CHARACTERIZATION OF ULTRASOUND CONTRAST AGENTS AS HYPERCEST AGENTS FOR MOLECULAR MRI

Christian T. McHugh

A dissertation submitted to the faculty of the University of North Carolina at Chapel Hill in partial fulfillment of the requirements for the degree of Doctor of Philosophy in the Department of Physics and Astronomy.

Chapel Hill
2022

Approved by:

Rosa T. Branca

Paul A. Dayton

Joaquin E. Drut

Yue Wu

Xiaopeng Zong

ABSTRACT

Christian T. McHugh: Characterization of Ultrasound Contrast Agents as
HyperCEST Agents for Molecular MRI
(Under the direction of Rosa T. Branca)

Molecular imaging is defined as an imaging technique capable of visualizing events that occur at the molecular level. For each imaging modality, there is a wide variety of molecular contrast agents that can be used for either therapeutic or diagnostic applications. Recently, there has been a push toward developing multipurpose theranostic contrast agents that are detectable across multiple imaging modalities. Gaseous microbubbles are an FDA-approved contrast agent that produce excellent ultrasound image contrast and have also been used for transport and delivery of drugs and gases. In this work, we explore if microbubbles can also be used as a contrast agent for magnetic resonance imaging.

In order to detect microbubbles using MRI at the clinical in-blood concentration used for contrast ultrasound studies, an alternative detection scheme known as hyperCEST must be used. Through simulations and *in vitro* experiments, microbubbles were characterized as efficient hyperCEST agents. We show that due to their high xenon loading capacity and favorable xenon exchange dynamics, microbubbles provided exceptional contrast and were detected at concentrations as low as 10s of fM, the lowest concentration for hyperCEST detection to date.

In preparation for *in vivo* translation, our lab optimized our hyperCEST imaging protocol by using cucurbit[6]uril. These results were the first demonstration of *in vivo* hyperCEST in mice. We show that in order to produce significant and reliable hyperCEST contrast, it is vital to establish a steady-state magnetization. These studies also revealed a spurious hyperCEST effect from direct saturation of the gas-phase signal in the lungs, a potential roadblock for *in vivo* translation of gas microbubbles as a hyperCEST agent.

Microbubbles are the precursor of liquid-core nanodroplets, and together, they act as a phase change contrast agents for ultrasound. In the liquid phase, perfluorocarbon nanodroplets have a ^{129}Xe resonance that is separated from the gas-phase, which may allow them to be distinguishable from the gas phase in the lung airspaces. We demonstrated that hyperCEST enables the detection of both liquid phase nanodroplets

and gas phase microbubbles, as well as their phase-conversion following exposure to US waves. This work establishes the feasibility of using nanodroplets as dual-phase dual modality contrast agent.

Despite the promising *in vitro* results, *in vivo* translation of these agents has proven to be challenging. Therefore future work should be focused on characterizing the hyperCEST properties of these agents in blood.

ACKNOWLEDGEMENTS

Moving to a new place as a young adult is tough. You don't have any money, you don't know where to buy a good milkshake, and finding friends takes a lot more effort than it did before. When I moved to North Carolina in the summer of 2017, those struggles were very real. For those first few weeks, it was easy to feel isolated in a new and unknown place. But when the Fall semester at UNC started and I began my journey through graduate school, I found myself surrounded by an extremely welcoming and supportive community. This community encouraged me when I felt like an imposter, empathized with me when the first-year workload was just too much, agreed with me when I would suggest ending the night at *Sup Dogs*, and inspired me to follow my passions. The work presented in this dissertation is a product of the relationships I made along the way; I could not have done it without them.

The world changed halfway through my third year, and everything went into lockdown; it was difficult not to feel isolated again. Sure, I found some comfort in revitalizing my *Pokémon* card collection, discovering *MetaZoo*, listening to *Pinegrove*, and playing countless hours of *Animal Crossing*. Even with the abundance of Zoom meetings, nothing compared up to the daily in-person interactions that I use to have with the people I cared about the most. It's strange that it took a full-fledged pandemic for me to really appreciated my fellow Tar Heels. I want to say thank you to everyone. Some of you may have already moved on to bigger and better things. Others, I may not have the chance to reconnect with before I myself move on. I hope each person gets the chance to read this to know that they are appreciated. You have made an impact on my life.

First and foremost, I want to recognize Tamara Branca, my advisor and mentor, for her guidance and support through these five years. Thank you for finding the perfect project for me. Your curiosity and motivation are qualities I aspire to have. You taught me how to think critically and solve problems quickly during an experiment - there is a live mouse in the scanner and we are constantly losing polarization, so every second counts! Most importantly, you taught me that anything can be fixed with a hot glue gun. Because of you, I am a better NMR scientist and experimentalist.

My experiments would not have been possible without the help of my labmates. Michele Kelley, thank you for sitting in a tiny room for hours to polarize the gas for my experiments. We have come a long way from those all-day experiments during our first summer in the group. Thank you, Nick Bryden, for also answering the call and occasionally being secluded in the polarizer room. More notably, you upgraded the ventilator - something that desperately needed some TLC. Sebastian Atalla, thank you for tolerating the lack of comments in my MATLAB code. I wish you the best of luck if you ever need to debug them in the future. Jack Garside, you stuck with me all through your four years of undergraduate research, three of them spent arguing with reviewers across four different journals to get a single paper published. I commend you on your perseverance. Thank you to the group's alumni, Michael Antonacci, Drew McCallister, Alex Burant, and Le Zhang for paving the way to where our group is today. I recently told someone that I could not have pictured myself in any other research group at UNC, and it is because of you all.

Many more people outside of our research group were pivotal in the success of my work. To each of my committee members: Paul Dayton, Joaquin Drut, Yue Wu, and Xiaopeng Zong, thank you for spending the time providing feedback on my thesis proposal and dissertation. Karl Koshlap, former manager of the UNC Eshelman School of Pharmacy NMR core facility, thank you for being available to troubleshoot my high-resolution NMR experiments. Jared Barkes, Jon Frank, and Hong Yuan of the BRIC Small Animal Imaging Facility were also invaluable when it came to prepping and scanning dozens of mice so that I didn't have to do it myself. Winnie Wang, thank you for being so flexible every time our experiments ran too long. I owe a lot to my bubble supplier, Phillip Durham. Thank you so much for making countless batches of microbubbles and nanodroplets. I never thought I would spend my PhD asking so many questions about bubbles, and you were always there to answer them.

During my time at UNC, I found the most joy in the classroom. I am so grateful that I had the opportunity to learn how to teach physics within a department that puts so much emphasis on developing research-based teaching methods. Duane Deardorff, Stefan Jeglinski, Alice Churukian, Jennifer Weinberg-Wolf, and Colin Wallace: thank you for mentoring me as I taught your courses and for trusting me to teach a course of my own. Because of you, I am a better physics educator. Shout out to my Learning Assistants: Nikos Dokmetzoglou, Samantha Pagan, Gaither Frye, Henry Nachman, and Cyrus Liu for helping me manage our classrooms. Most of all, thank you to all of the students I had the pleasure of having in my classes.

The camaraderie among the graduate students in the Department of Physics and Astronomy is a quality all graduate programs should strive to establish. I am indebted to my cohort. From our group trip to South Carolina to see the total solar eclipse to celebrating at the Qual party, I don't think I could have made it through the first year if it wasn't for the great people I was with along the ride. I look forward to seeing where you all end up. Thanks especially to Tim Osborne and Derrick Carr for being there through the good times and the bad.

I found a second home at the Newman Catholic Student Center Parish. I was welcomed with open arms by Kevin O'Reilly and Pamela Tremblay. Kevin, you brought worship music back into my life and I will always remember our Ignite trips. Pam, thank you for fostering a community for the graduate students and young adults in the parish. I will treasure the fun memories from First Friday Happy Hours, playing music for adoration, and the annual mixers at the start of each academic year.

Sarah, our story started at one of those mixers. Here we are now, just weeks away from our wedding. Throughout the years, we have been a team just trying to make it through grad school. It looks like we finally made it. I am so excited to marry you.

Finally, I would be nowhere without my family. Thank you for your constant love and support. After so many years, I'm happy to say that this is my last degree and I'm finished with school!

It will be difficult to move on from UNC. It has been an incredible five years. I am so thankful for every second of it. I couldn't have chosen a better place to spend my career as a graduate student.

#GDTBATH.

TABLE OF CONTENTS

LIST OF TABLES

LIST OF FIGURES

LIST OF ABBREVIATIONS

ADV	Acoustic Droplet Vaporization
BAT	Brown Adipose Tissue
BM	Bloch-McConnell
BOLD	Blood-Oxygen-Level Dependent
CB[6]	Cucurbit[6]uril
CEST	Chemical Exchange Saturation Transfer
COVID-19	Coronavirus Disease 2019
CryA	Cryptophane-A
CT	Computed Tomography
CW	Continuous Wave
DFB	Decafluorobutane
FDG	Fluorodeoxyglucose
FHC	Full HyperCEST
FID	Free Induction Decay
GLUT1	Glucose Transporter 1
HP	Hyperpolarized
HyperCEST	Chemical Exchange Saturation Transfer with Hyperpolarized ^{129}Xe
KO	Knock Out
MB	Microbubble
MRI	Magnetic Resonance Imaging
NMR	Nuclear Magnetic Resonance
NST	Non-Shivering Thermogenesis
PET	Positron Emission Tomography
PBS	Phosphate Buffered Saline
PFC	Perfluorocarbon
PFOB	Perfluorobutane
PPM	Parts Per Million
qHyperCEST	Quantitative hyperCEST

RBC	Red Blood Cell
RF	Radiofrequency
SAR	Specific Absorption Rate
SARS-CoV-2	Severe Acute Respiratory Syndrome Coronavirus 2
SEOP	Spin Exchange Optical Pumping
SPION	Superparamagnetic Iron Oxide Nanoparticles
SUV	Standardized Uptake Value
UCP1	Uncoupling Protein 1
US	Ultrasound
WT	Wild Type
XECT	Xenon Enhanced CT

CHAPTER 1: INTRODUCTION

In 1895, a physicist Wilhelm Röntgen was testing a cathode-ray tube when he noticed that a phosphorescent screen stored in the corner of his laboratory began to glow vividly in the darkened room. This new kind of radiation, initially deemed "X" radiation due to its unknown properties, intrigued Röntgen and he continued placing various objects in the beam's path to observe the transmission through solid materials. Among those objects was his wife's hand; when x-rays passed through her hand onto a photographic plate, the chilling image of her bones appeared along with the distinct outline of her ring (1; 2; 3; 4). This historical discovery was the first medical image, and Röntgen was awarded the very first Nobel Prize in Physics in 1901 (5).

News of this discovery went viral. Many scientists had access to cathode-ray tubes and could also produce x-rays (eventually named Röntgen rays (6), but the former name seemed to garner more public appeal) themselves. The general public was fascinated by x-rays (1), and many, including Thomas Edison, would partake in sideshows at amusement parks to casually get exposed to radiation and see the inner architecture of their bodies (4). Keep in mind that this was also during a time when people would willingly choose to imbue paint or cocktails with radium because of its attractive illuminating abilities. These patrons may have benefitted from the adage: *With great power comes great responsibility*.

That responsibility was taken up by another physicist, Marie Curie. Although Madame Curie is commonly known for her work with radioactivity, she made significant strides in making the medical use of x-rays widely available (4). Following Röntgen's discovery, physicians immediately adopted the technology to assist with diagnosis. Prior to 1895, surgeons would put patients through an extremely painful ordeal as they used tactile pressure to externally search for internal foreign bodies, only to cut blindly when extraction was necessary, occasionally missing their target. X-rays are particularly sensitive to metal objects such as bullets (6), and the use of imaging would provide efficient diagnosis and treatment of soldiers allowing for quicker full-recovery. At the time of World War I, Curie was astonished at the fact that imaging was not being utilized for this purpose. Instead, doctors on the battlefield regularly chose amputation as a quick solution, needlessly removing limbs when x-rays could have indicated a simple fracture. Curie

raised funds to properly equip the battlefields with mobile x-ray units. She educated the operators not only on how to collect an image, but also on the associated fundamental physics. At that time, physicists and physicians were separate professions. It was becoming more apparent that the two fields were necessarily intertwined, and these radiologists were at the cross-section. By the end of World War I, medical imaging was ubiquitous, and a surgeon would not choose to pick up a scalpel before viewing a diagnostic image.

Marie Curie was compelled to use her knowledge of science and technology in the service of humanity to improve quality of life. This type of motivation led to the growth of the subfield of Medical Physics. Medical Physics is a thriving interdisciplinary field where diagnostic and therapeutic strategies are constantly advancing. Imaging has diversified into a variety of modalities including computed tomography (CT), positron emission tomography (PET), magnetic resonance imaging (MRI), and ultrasound (US). Across these modalities, the topic of molecular imaging is an innovative concept where image contrast is produced by biochemical events at the molecular level. Each modality employs its own roster of exogenous contrast agents for molecular imaging, which will be described briefly in the following sections.

1.1 Computed Tomography

Planar x-ray imaging, as it was introduced by Röntgen, produced an image that was a result of x-rays passing through the entire object and collected on the other side. While this is not so much of a problem for imaging a human hand, an x-ray image of the abdominal region would not retain much anatomical information as the image would be formed from x-rays that were attenuated by many layers of multiple different tissues. Each organ would be superimposed on one another, resulting in a projection. In order to image thin, interior slices throughout the body, an imaging technique known as computed tomography (CT) was developed in 1970s. CT involves collecting a series of projections around the body and using a computational algorithm to reconstruct high-resolution slices (7). The 1979 Nobel Prize in Physiology of Medicine was awarded to physicist Allan Cormack and electrical engineer Godfrey Hounsfield for the development of CT (8).

The interaction of x-rays with tissue depends on the incident x-ray energy and the chemical composition of the tissue. At high energies, Compton scattering is more probable, and x-rays are deflected by the electrons in the outer shell of an atom in tissue. This ultimately results in poor image contrast. At lower energies, photoelectric interactions are more probable. The photoelectric effect is directly related to the

cube of the atomic number (Z) of the atom upon which the x-ray is incident. This is what gives rise to the stark contrast between tissue and bone; the oxygen (Z=8) present in water and tissue produces much less attenuation than calcium (Z=20) in bones (7). Based on this property, atoms with high atomic number can be introduced into the biological system to enhance contrast. These radiodense exogenous molecules are known as molecular contrast agents. By monitoring their biodistribution, specific physiological processes associated with the contrast agent can be imaged.

Xenon (Z=54) is a biocompatible and inert noble gas that has been used for a multitude of biomedical imaging applications, including providing xenon-enhanced image contrast for CT due to its high Z number (9; 10). Xenon is extremely lipophilic, and it was shown that xenon-enhanced CT (XECT) is particularly adept at identifying and quantifying brown adipose tissue (BAT) (10; 11). BAT is a fat tissue found in most mammals that helps regulate energy balance and core body temperature through a sympathetic process known as non-shivering thermogenesis (NST). Insufficient BAT activity could lead to an energy imbalance, resulting in metabolic diseases like obesity and diabetes. As such, BAT is a promising target for therapies and treatments for obesity (12). In order to evaluate the efficacy of these treatments, imaging modalities that are able to accurately identify and quantify BAT thermogenesis are essential (13; 14). Upon BAT stimulation with norepinephrine (15), blood flow increases to regions of BAT, transporting and depositing xenon into BAT depots. The dramatic increase in radiodensity in these regions demonstrated that XECT is specific and sensitive to BAT in both mice (10) (Figure 1.1) (11) and nonhuman primates (10) (NHP). In this study, NST activity was cross-validated using by means of another imaging modality, positron emission tomography.

1.2 Positron Emission Tomography

Positron emission tomography (PET) is a molecular imaging modality in the realm of nuclear medicine. In contrast to CT where radiation is directed towards the body, PET detects radiation as it leaves the body. This radiation is a product of a sequence of reactions initiated by the decay of radioactive contrast agents known as radiotracers. Radiotracers are typically an analog of biologically active molecule that contain a radioactive isotope. For example, fluorodeoxyglucose (FDG) is a glucose analog that carriers ^{18}F (13; 14; 16). ^{18}F undergoes radioactive β-decay, emitting a positron and a neutrino (7; 17). A positron is the antiparticle of an electron. When an electron and an anti-electron collide, they annihilate to produce

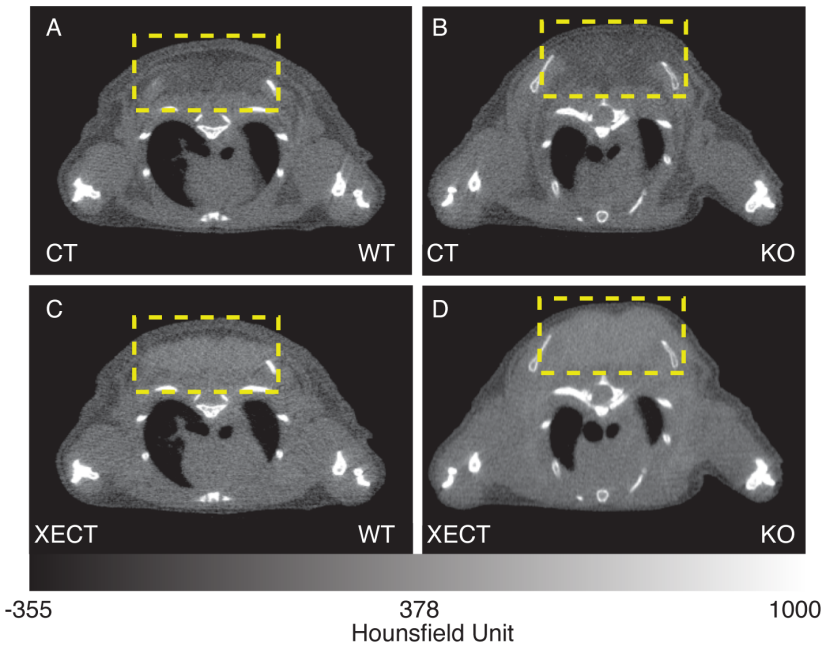

Figure 1.1: Selective radiodensity enhancement of BAT after NE stimulation of NST in a WT and in a KO mouse. Axial (a) CT and (b) XECT images of a WT mouse after NE injection. Axial (c) CT and (d) XECT images of a KO mouse after NE injection. In both WT and KO mice adrenergic stimulation of BAT resulted in a radiodensity enhancement of BAT of more than 200 HU (yellow dashed box).

two photons that move in precisely the opposite direction due to conservation of momentum. Upon detection of these photons, the origin of this annihilation event can be located by back-tracing their trajectories. A PET scanner is engineered to detect the emitted pair of photons using a complete ring of scintillating crystals that surround the patient, and the photons corresponding to a specific positron annihilation would be detected almost simultaneously on opposite sides of the ring.

As the radiotracers distribute throughout the body, they accumulate in regions based on their physiological purpose such as metabolic activity (18; 19). The molecular imaging capabilities of PET provide molecular-level information of biochemical processes before anatomical changes can be detected in alternative imaging methods. FDG PET, for example, is widely used in oncology to detect tumors, which general take up more glucose than healthy tissue (20). The amount of radiotracer that is taken up by a given tissue is quantified by the standardized uptake value (SUV), which is a measure used to threshold and validate diagnosis. PET and CT are regularly performed on a hybrid scanner in a single session, as CT provides anatomical context to SUV for more accurate diagnosis (21; 22).

Recently, FDG PET/CT imaging has been used to study infection diseases that produce inflammatory response, specifically COVID-19. In NHPs, FDG uptake served as a proxy for metabolic activity in the

lungs, which correlated to CT-identified structural abnormalities following exposure to SARS-CoV-2 (23). After the NHPs were exposed to SARS-CoV-2, FDG uptake increased as the disease progressed (24; 25; 26). Also, it was shown that vaccinated NHPs experiences less FDG uptake than nonvaccinated control NHPs (27). PET imaging remains at the forefront of clinical research.

FDG PET/CT has also been used to identify and quantify thermogenically active BAT in the interscapular fat depots of rodents (10; 28; 29; 30; 31) (Figure 1.2) (32) and humans (13; 14; 33), and to many, it is considered the gold standard. Several articles have extensively reported on the many limitations of FDG PET for the detection of BAT activity (13; 14), even suggesting that adrenergically induced glucose uptake in BAT is independent of BAT thermogenesis (31). These results seem to indicate that the high variability seen in human BAT glucose uptake (34; 35) may not be due to true differences in BAT thermogenesis (36), but to differences in insulin sensitivity and tissue blood flow (37).

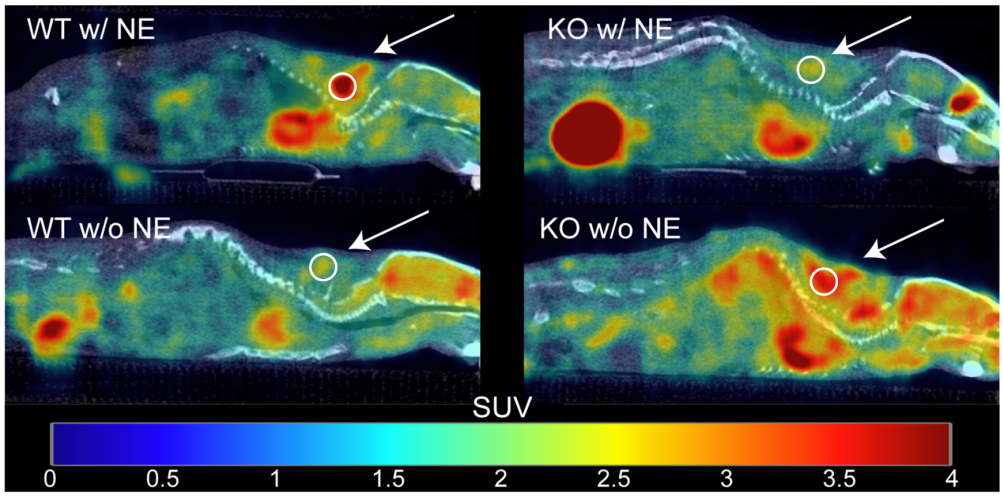

Figure 1.2: Example of fused FDG PET/CT images acquired from fasted male WT and KO mice with and without NE injection. Images are displayed on the same SUV scale on a sagittal view. Male mice were subject to scans with (top row) and without (bottom row) NE injection. The arrows indicate regions of interscapular BAT, and circles indicate the 5 mm2 ROI centered around the local maximum that was used to measure SUVpeak. While uptake increases after NE injection for the WT mouse (left column), uptake for the KO mouse (right column) seems suppressed upon NE injection.

Thermogenic activity in BAT is driven by the uncoupling protein 1 (UCP1), a protein that uncouples oxidative phosphorylation from adenosine triphosphate production in the mitochondria of brown adipocytes, resulting in increased heat production. It is widely accepted that BAT thermogenesis is contingent on the presence of functional UCP1 (38). Therefore, wild type (WT) and genetically modified knockout mice lacking UCP1 (KO) have been used to validate the use of FDG PET for the detection of

BAT thermogenic activity. However, the current literature is comprised of conflicting results. In a study of only male mice, adrenergic stimulation led to an increase of FDG uptake in BAT of WT mice and not in KO mice, suggesting that FDG uptake is indeed a good measure of UCP1-mediated thermogenesis (28). This finding was later supported by Jeanguillaume et al. who, this time, included both male and female mice. Unexpectedly, these authors observed FDG uptake in female KO mice, suggesting an effect due to sex (29). This discrepancy between male and female KO mice was corroborated by Hankir et al., who suggested that uptake is actually independent of the expression of UCP1 (30). Olsen et al. identified the UCP1-independent mTOR pathway was identified as an alternative cause for [^{18}F]FDG uptake upon BAT stimulation, but they did not observe the difference in uptake between male and female KO mice (31).

These conflicting reports demonstrate the controversy of relying on FDG uptake to indicate BAT thermogenesis. Incorrect identification could be caused by a variety of confounding variables including differences in animal handling techniques such as feeding status, type of anesthetic, type of BAT stimulation, and estrogen levels (32). It was also hypothesized that there is some UCP1-dependent mechanism that inhibits glucose uptake in absence of adrenergic stimulation, while facilitating glucose uptake upon stimulation. Glucose transport across cell membranes is facilitated by proteins such as glucose transporter 1 (GLUT1). Inokuma et al. (28) reported that GLUT1 mRNA levels were 1.4 times higher in KO mice when compared to WT mice. Therefore, even without stimulation, KO mice are expected to have higher [^{18}F]FDG uptake due to higher expression of GLUT1. The functional activity of GLUT1 is enhanced after NE injection, and this may be due to a conformational change in GLUT1 that increases its affinity for glucose (39). In the presence of UCP1, GLUT1 might behave like a NE-gated channel that either restricts glucose uptake at baseline, or enhances glucose uptake upon NE stimulation. Conversely, for KO mice that lack UCP1, such control on GLUT1 might have been lost, resulting in consistent changes and high variations in both baseline and stimulated conditions (32).

When a positron is emitted from the radioactive decay of the radiotracer, it may traverse up to 1 mm before pair-annihilation (7). This movement may affect the correspondence between the actual location of the radiotracer and the calculated location based on the detected photons. Positrons are charged particles, and therefore, they interact with magnetic fields. In 1991, physicist Raymond Raylman hypothesized in his PhD thesis that an external static magnetic field may assist with reducing the positron range and increase PET image resolution (40). This idea led to another dual-modal development in molecular imaging, this time combining PET with magnetic resonance imaging (35; 41).

1.3 Magnetic Resonance Imaging

Magnetic resonance imaging (MRI) is a medical imaging modality based on concepts in nuclear magnetic resonance (NMR). Although the acronym NMRI might be more accurate, the nuclear description is colloquially redacted due to its stigma. But in the case of NMR, nuclear only refers to the nucleus of an atom, as opposed to the radioactive processes associated with nuclear medicine. MRI is further separated from nuclear medicine due the fact that PET radiotracers produce high-energy, ionizing gamma radiation while MRI probes nuclear spins using non-ionizing radiofrequency (RF) pulses. With the help of magnetic fields, MRI is able to produce high-resolution images for molecular imaging (42; 43). The fundamental principles of NMR were first recognized by physicist Isidor Rabi, which earned him the 1944 Nobel Prize in Physics (44). As the field evolved, the development of MRI by physicists Peter Mansfield and Paul Lauterberg garnered yet another Nobel Prize in 2003, this time in the category of Physiology or Medicine (45).

MRI detects the precession of spin-1/2 nuclei such as ^{1}H, ^{13}C, ^{19}F, and ^{129}Xe. Due to the fact that lipophilic ^{129}Xe is magnetically visible, hyperpolarized (HP) ^{129}Xe MRI has also been used as a means to detect BAT (11; 46; 47). Upon adrenergic stimulation of NST, HP ^{129}Xe is shuttled to regions of BAT, and contrast was easily detected in not only lean mice, but also obese mice (Figure 1.3) (46). This puts HP ^{129}Xe MRI at an advantage because BAT detection using the alternative imaging modalities has been difficult for obese subjects, the population that would benefit the most from BAT imaging.

The purpose of NST is to maintain core body temperature by producing heat. As such, detection of NST has also been done by measuring temperature with infrared thermography or direct probing with thermocouples. The former, while noninvasive, lacks the specificity to BAT as it relies on the conduction of heat to the superficial surface of the skin. The latter is invasive, and it is particularly sensitive to probe positioning (11; 32). Certain NMR resonances, like the water ^{1}H resonance for example, are temperature dependent and can provide information on absolute temperature. Recently, it was also shown that the resonance frequency of xenon dissolved in lipids has a strong temperature dependence, much stronger than that of water (-0.2ppm/°C versus -0.01ppm/°C) (48; 49). This has been demonstrated *in vivo* in mice, isolating changes in temperature directly to NMR signal emanating from BAT (11; 46). Interestingly, with ^{129}Xe MR thermometry, UCP1-KO mice exhibited a thermogenic response (11), casting more doubt on the contingency of UCP1 on NST (30; 31; 32).

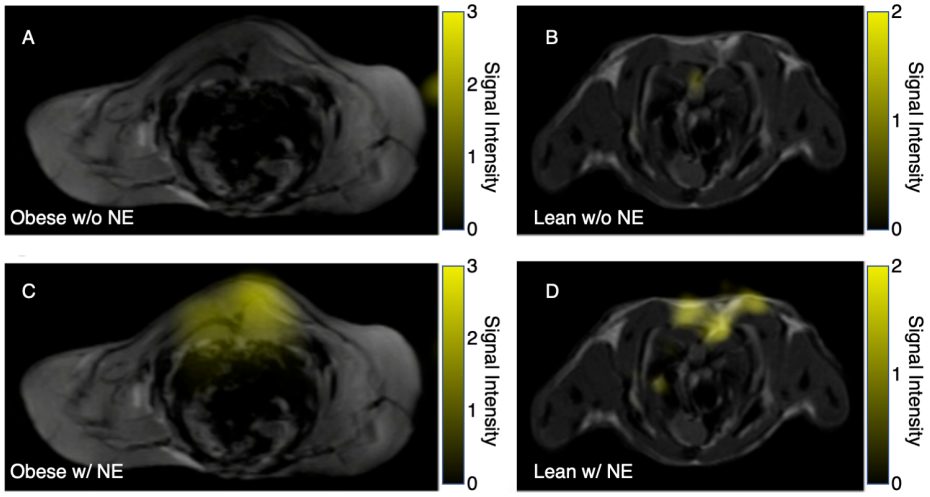

Figure 1.3: HP ^{129}Xe maps of interscapular BAT in lean and obese mice. HP dissolved-phase ^{129}Xe images are displayed as a false color overlay on the corresponding 1-mm-thick axial proton reference image at baseline (A and B) and during adrenergic stimulation of NST. Significant signal enhancement is observed in both obese (left) and lean (right) mice in regions of interscapular BAT.

MR image contrast can be generated by clever RF pulse sequence design that takes advantage of the relaxation properties of nuclear spins within various compartments. This is why MRI excels at soft tissue anatomical imaging (50). Local, microscopic magnetic field gradients can easily alter the image contrast. A functional MRI technique known as blood-oxygen-level dependent (BOLD) imaging is commonly used to image blood flow in the brain, as it leverages the local change in magnetic susceptibility that arises from the local increase in blood volume and oxygenation (51; 52; 53). Hemoglobin is responsible for carrying oxygen throughout the body, and depending on whether a hemoglobin molecule is oxygenated or deoxygenated, its magnetism is diamagnetic or paramagnetic, respectively. The presence of paramagnetic molecules in blood can increase its paramagnetism with respect to tissue and lead to local susceptibility gradients. As a result, the microscopic spin population dephases, and signal in that region is lost in T_2-weighted images. BOLD has been used to detect BAT in mice (54). BOLD is an example of molecular imaging with an endogenous contrast agent, hemoglobin.

A similar effect can be achieved with exogenous MR contrast agents such as superparamagnetic iron oxide nanoparticles (SPION) (55). SPIONs are widely considered to be biocompatible and are used in multiple biomedical applications (56), but there is growing concerns about their toxicity. (57; 58). One application is the internal transportation and targeted delivery of payloads guided by external magnetic fields (59). These payloads may contain gases or therapeutic drugs and can be encapsulated by a molecular

carrier known as a microbubble (MB) (60). By embedding MB with SPION, they were able to be directly detected with MRI (61). In order to release the payload, ultrasound (US) waves can be used to interact with, detect, or collapse MB due to their echogenic properties.

1.4 Ultrasound

Ultrasound (US) is a medical imaging modality that does not rely on electromagnetic waves, but rather acoustic waves oscillating at frequencies between 1 and 10 MHz. These mechanical waves are transmitted into the body via a transducer. As the waves propagate, they are scattered to varying degrees based on the surface they encounter. Some waves are backscattered directly along the original transmission path, and the transducer receives the signal and extracts depth and anatomical information based on time delay and intensity, respectively (7). The intensity is a function of the acoustic impedance of the media; the larger the impedance mismatch between interfaces, the greater the sensitivity to imaging different physiological compartments. The impedance mismatch between blood and tissue is relatively small, so it is difficult to resolve vasculature from other physiological tissues without the assistance of a molecular US contrast agent (62).

Microbubbles (MB) are gas-filled microspheres that serve as a contrast agent for clinical US imaging (63; 64; 65; 66). MB consist of a heavy-gas core surrounded by a lipid shell. They are extremely echogenic and provide enhanced US image contrast due to the large impedance mismatch with respect to blood or tissue (62). The compressible nature of a MB allows it to oscillate in an acoustic field, producing a nonlinear response to further enhance their signal to better image vascular networks (67; 68) (Figure 1.4).

MB have also been used as a vehicle of gas delivery for therapeutic applications. With US, MB can be guided and ruptured on command to deliver their contents to targeted sites. For example, delivery of oxygen can reverse tumor hypoxia to better facilitate diagnosis and treatment (60; 69). MB loaded with nitric oxide improved stem cell based therapies for angiogenesis in myocardial infarct areas (60; 70). Thermally polarized xenon also has therapeutic potential where targeted delivery could assist with neuroprotection against stroke by inhibiting the receptor pathway associated with neuronal death (60; 71). Similarly, HP ^{129}Xe MRI could benefit greatly from targeted delivery to regions of BAT as MR signal is directly propor-

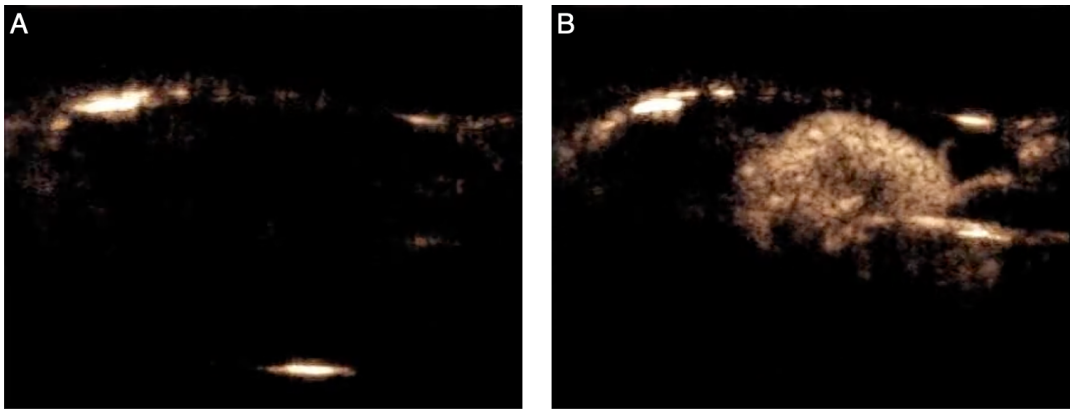

Figure 1.4: Microbubble enhanced ultrasound imaging. Sagittal ultrasound images of a rat are displayed before (A) and after (B) MB perfusion. Initially, there is essentially zero contrast visible. With the addition of MB, the vasculature of the kidney becomes very clearly defined.

tional to spin density. With this in mind, MB show potential to be used not only to enhance the contrast in US images but also in MR images

1.5 Overview of Contents

In the world of molecular imaging, contrast agents are used for therapeutic or diagnostic applications. Recently, there has been a push toward developing the field of theranostics where singular molecular compounds can serve both therapeutic and diagnostic purposes and are detectable across multiple imaging modalities (69; 72; 73). In the previous section, the benefits of multimodal imaging were made apparent; CT gave anatomical context to PET and PET gave functional context to MRI. The focus of this thesis revolves around the union of MRI and US by developing MR techniques to detect established US contrast agents.

In Chapter 2, the fundamental physics of NMR are presented. Chapter 3 builds upon this theory by introducing the mechanism of chemical exchange saturation transfer with hyperpolarized ^{129}Xe, or hyperCEST. This technique allows the indirect detection of MB at extremely low concentrations, and in Chapter 4, MB are characterized for their efficacy as hyperCEST contrast agents. *In vivo* hyperCEST imaging is the topic of Chapter 5, where experimental considerations are optimized for the well-establisted hyperCEST agent cucurbit[6]uril. Chapter 6 presents the dual-phase capabilities of MB, as nanodroplets, the condensed form of MB, also facilitate hyperCEST but at a different functional frequency. Finally, this the-

sis concludes with preliminary data for in vivo hyperCEST detection of US contrast agents and discusses its complications and goals for future work.

The family tree of medical imaging was planted by Röntgen – its roots in physics and its branches in the health sciences. Medical physics has been recognized by the scientific community with multiple Nobel Prizes and by the clinical community with the widespread clinical use of imaging in hospitals around the world. This thesis hopes to continue the lineage of physics in medicine by introducing a dual-modal, dual-phase contrast agent for molecular MR/US imaging.

CHAPTER 2: CONCEPTS IN NUCLEAR MAGNETIC RESONANCE

2.1 Nuclear Magnetic Resonance Physics

The early twentieth century saw a dramatic shift in the paradigm of physics. The classical theories of Isaac Newton and James Clerk Maxwell eventually became insufficient for explaining experimental results, and a new quantum theory was born. This revolution was spearheaded by notable greats such as Paul Dirac, Albert Einstein, Werner Heisenberg, and Erwin Schrödinger who would meet regularly with their contemporaries at the famous Solvay Conferences to discuss the recent advances in physics and chemistry (74). In 1927, the fifth Conference focused on electrons and photons (75), but two significant contributors to the field were not in attendance.

At the time, George Uhlenbeck and Samuel Goudsmit were graduate students at Leiden University under the supervision of Paul Ehrenfest. Together, Uhlenbeck and Goudsmit studied atomic spectra. Uhlenbeck was more grounded in analytical theory, juxtaposed to Goudsmit, who would approach science by making intuitive guesses and presenting ideas that seemed to stumble upon the truth (76). In fact, Goudsmit believed that luck plays a significant, and often uncredited, role in the advancement of physics (77).

After Wolfgang Pauli introduced his exclusion principle in 1925, which included a new, fourth quantum number (78), Goudsmit tested his luck and employed this new half-integer quantum number while deciphering the anomalous Zeeman effect. The Zeeman effect is the splitting of spectral lines in the presence of an external magnetic field. For some atoms, an anomaly occurs, and the observed splitting does not match classical theory. When Goudsmit made his guess, "like magic," the theory fit precisely (76; 77). Goudsmit informed Uhlenbeck of this result, and Uhlenbeck realized its implications. Electrons must possess a fourth degree of freedom to correspond to this fourth quantum number. The charge must spin and generate its own magnetism. This made Uhlenbeck skeptical.

The findings were written up with Uhlenbeck as the first author, seeming to fully support the bold claims of Goudsmit, and the note was submitted for publication (79). Ehrenfest contacted Hendrik Lorentz

for his opinion on the spinning of electrons. Lorentz determined that this idea was inconsistent with an electron spinning in the literal sense, requiring rotation faster than the speed of light in order for the charge to produce the expected magnetic effect. Uhlenbeck's fears were met, and he pleaded with Ehrenfest to not submit the article. Alas, the article was already sent off to review. Ehrenfest attempted to comfort his graduate student by pointing out that Uhlenbeck had no reputation and, therefore, nothing to lose.

To this day, the conceptualization of spin remains obscure and unclear. Nonetheless, just as it was observed by Uhlenbeck and Goudsmit, its reality becomes apparent in experimental data. The spin of a particle is its source of intrinsic magnetism and, as a result, particles with non-zero spin interact with magnetic fields dynamically. In this chapter, I discuss how spins interact with external magnetic fields and present the mathematical derivations for spin dynamics. The controlled manipulation and measurement of an ensemble of spins is the goal of nuclear magnetic resonance (NMR) spectroscopy. NMR is a multifaceted tool that was the focus of Nobel Prizes awarded in physics (44; 80), chemistry (81; 82), and medicine (45), establishing its utility for interdisciplinary research. From defining molecular structure to imaging cancerous tumors, NMR brings spin to life.

2.2 Fundamental Interaction of Spin with a Magnetic Field

Intrinsic spin can be represented by a quantum mechanical operator $\hat{S}$. It is a form of angular momentum whose components follow the fundamental commutation relation:

$$\left[\widehat{S}_i, \widehat{S}_j\right] = i\hbar\epsilon_{ijk}\widehat{S}_k \tag{2.1}$$

where i is the imaginary unit, $\hbar$ is Planck's constant (1.05457 x 10^{-34} J s), and ϵ_{ijk} is the antisymmetric Levi-Civita tensor used according to the Einstein summation convention with indices i, j, k representing orthogonal axes x, y, z, respectively. Due to the fact that the components of $\hat{S}$ do not commute, the Uncertainty Principle places a limit on the precision of measuring individual components simultaneously. A particle's spin determines its magnetic behavior, and its magnetic moment $\hat{\mu}$ is defined as:

$$\hat{\mu} = \gamma\hat{S} \tag{2.2}$$

The gyromagnetic ratio γ is the proportionality factor relating $\hat{\mu}$ and $\hat{S}$, and Table 2.1 lists γ for a variety of spin-1/2 nuclei. The sign for γ may be positive or negative, corresponding to whether the magnetic moment aligns parallel or antiparallel to the spin angular momentum (Figure 2.1). When a magnetic moment is placed within an external magnetic field $\vec{B}_0$, it precesses around $\vec{B}_0$ at the Larmor frequency ω_0, which is also proportional to the gyromagnetic ratio.

$$\vec{\omega}_0 = -\gamma \vec{B}_0 \tag{2.3}$$

Here, the sign of γ determines the direction of precession when using a right-handed coordinate system as viewed looking down on the plane transverse to $\vec{B}_0$; a positive or negative Larmor frequency corresponds to a counterclockwise or clockwise rotation, respectively (Figure 2.1). The quantum and classical derivation of single-spin precession will be presented in the following sections.

Isotope	Gyromagnetic Ratio (γ) [10^6 rad s^{-1} T^{-1}]	Larmor Frequency (ω_0) [MHz]
^{1}H	267.522	400.228
^{2}H	41.066	61.473
^{13}C	67.283	100.659
^{15}N	-27.126	-40.582
^{19}F	251.815	376.729
^{31}P	108.394	162.164
^{129}Xe	-74.521	-111.488

Table 2.1: Gyromagnetic ratios (83) and Larmor frequencies for various isotopes at B_0 = 9.4 T.

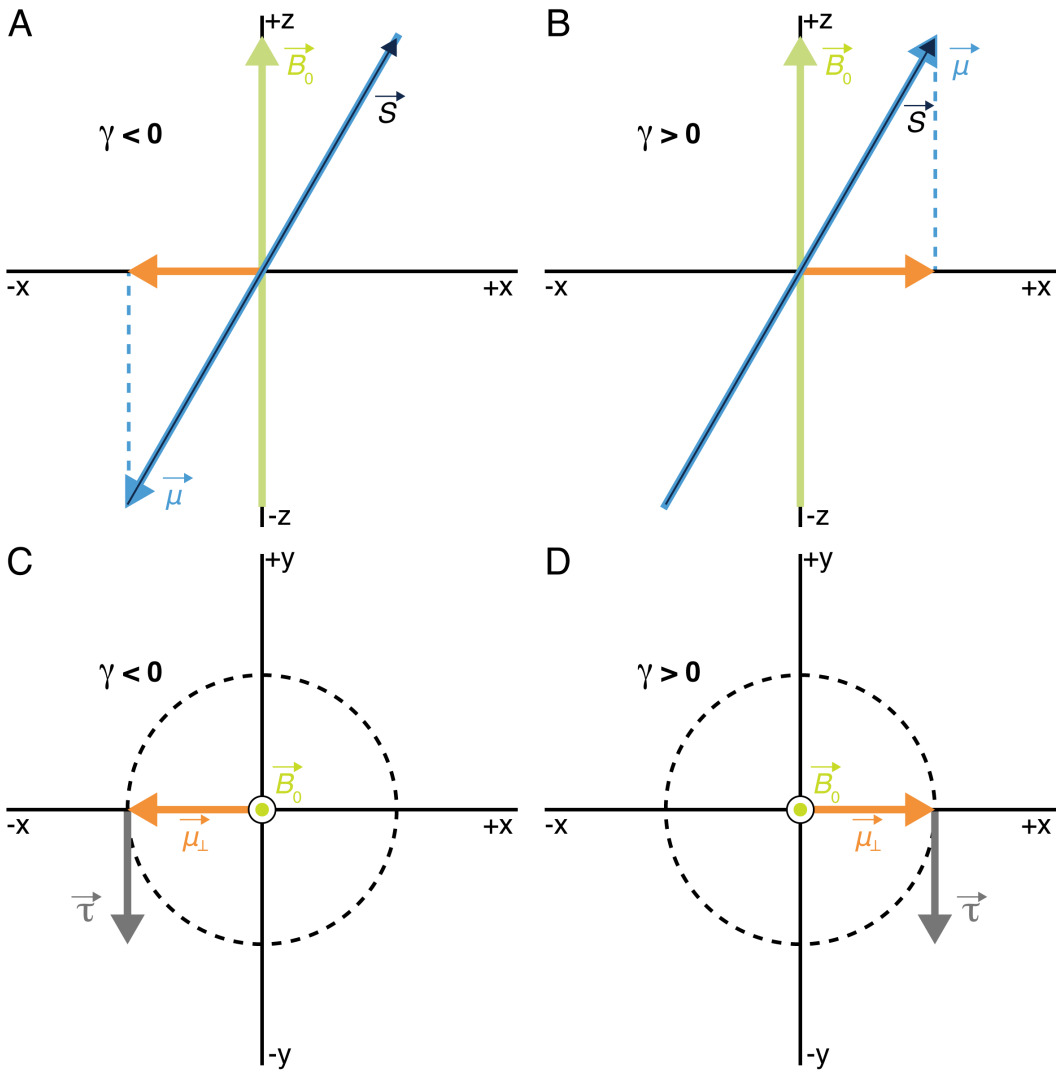

Figure 2.1: Gyromagnetic ratio and spin precession. The gyromagnetic ratio γ relates a nucleus's spin $\vec{S}$ to its magnetic moment $\vec{\mu}$. When γ is negative (A), $\vec{\mu}$ is aligned anti-parallel to $\vec{S}$. When γ is positive (B), $\vec{\mu}$ is aligned parallel to $\vec{S}$. When the nucleus is placed in an external magnetic field $\vec{B}_0$ in the +z direction, a torque is applied according to Eq. (2.15). When γ is negative (C), the projection of $\vec{\mu}$ onto the transverse plane ($\vec{\mu}_\perp$) rotates with a positive Larmor frequency in the counterclockwise direction. When γ is positive (D), $\vec{\mu}_\perp$ rotates with a negative Larmor frequency in the clockwise direction.

2.3 Quantum Derivation of Single-Spin Precession

Quantum mechanics takes place in Hilbert space, a linear vector space where physical observables are represented by Hermitian matrix operators and physical states are represented by vector wavefunctions. The time-evolution of a quantum system can be determined by taking either of two perspectives: the Schrödinger picture and the Heisenberg picture.

In the Schrödinger picture, the state $|\psi\rangle$ evolves in time according to the Schrödinger equation:

$$i\hbar\frac{\partial}{\partial t}\left|\psi\left(t\right)\right\rangle = \hat{H}\left|\psi\left(t\right)\right\rangle \tag{2.4}$$

where $\hat{H}$ is the Hamiltonian of the system. The Hamiltonian is the time-evolution operator and, in most cases, is simply defined as the sum of the potential energy ($\hat{U}$) and kinetic energy ($\hat{T}$) of the system.

$$\hat{H} = \hat{U} + \hat{T} \tag{2.5}$$

In the Heisenberg picture, the dynamics of the system is determined by the time-evolution of the operators before they act on a static state. The Heisenberg equation of motion for an operator $\hat{A}$ is:

$$\frac{d\hat{A}\left(t\right)}{dt} = \frac{1}{i\hbar}\left[\hat{A}\left(t\right), \hat{H}\right] \tag{2.6}$$

This is analogous to the Poisson bracket formalism in classical Hamiltonian dynamics. While either perspective accurately models the behavior of the quantum system, the Heisenberg picture is used here for simplicity to derive the precession of a single spin within an external magnetic field.

For a nuclear magnetic moment $\hat{\mu}$ within a static external magnetic field $\vec{B}_0$, the Hamiltonian is time-independent and can be expressed as:

$$\hat{H} = -\hat{\mu}\cdot\vec{B}_0 \tag{2.7}$$

By convention, the z-axis is aligned with $\vec{B}_0$, and using equations (2.2) and (2.3), the Hamiltonian can be written in terms of the corresponding parallel-component of the spin $\hat{S}$ and Larmor frequency ω_0:

$$\hat{H} = -\hat{\mu}\cdot\vec{B}_0 = -\gamma\hat{S}\cdot\vec{B}_0 = \left(-\gamma B_0\right)\hat{S}_z = \omega_0\hat{S}_z \tag{2.8}$$

The Heisenberg equation of motion is then written as:

$$\frac{d\hat{S}_i\left(t\right)}{dt} = \frac{1}{i\hbar}\left[\hat{S}_i\left(t\right), \omega_0\hat{S}_z\right] \tag{2.9}$$

where i = x, y, z for each component of the intrinsic spin. Using the spin angular momentum commutator relation (Eq. 2.1), the Heisenberg equation of motion produces a simple system of coupled differential equations.

$$\frac{d\hat{S}_x(t)}{dt} = -\omega_0 \hat{S}_y(t)$$
$$\frac{d\hat{S}_y(t)}{dt} = \omega_0 \hat{S}_x(t) \tag{2.10}$$
$$\frac{d\hat{S}_z(t)}{dt} = 0$$

The transverse components of the spin, $\hat{S}_x$ and $\hat{S}_y$, are analogous to a 2-dimensional harmonic oscillator that oscillates around the transverse plane. The z-component of the spin, $\hat{S}_z$, is parallel to the external magnetic field, and its dynamic solution to constant in time.

$$\hat{S}_x(t) = \hat{S}_{x,0}\cos\omega_0 t - \hat{S}_{y,0}\sin\omega_0 t$$
$$\hat{S}_y(t) = \hat{S}_{y,0}\cos\omega_0 t + \hat{S}_{x,0}\sin\omega_0 t \tag{2.11}$$
$$\hat{S}_z(t) = \hat{S}_{z,0}$$

These time-dependent spin operators are proportional to the corresponding components of the magnetic moment operator (Eq. 2.2). For an arbitrary state $|\psi\rangle$, the expectation values for the measurement of each component of the magnetic moment are also time-dependent.

$$\begin{aligned}\langle\hat{\mu}_x\rangle(t) &= \langle\psi|\hat{\mu}_{x,0}\cos\omega_0 t - \hat{\mu}_{y,0}\sin\omega_0 t|\psi\rangle \\ &= \langle\psi|\hat{\mu}_{x,0}|\psi\rangle\cos\omega_0 t - \langle\psi|\hat{\mu}_{y,0}|\psi\rangle\sin\omega_0 t \\ &= \langle\hat{\mu}_x\rangle_0\cos\omega_0 t - \langle\hat{\mu}_y\rangle_0\sin\omega_0 t\end{aligned} \tag{2.12}$$

$\langle\hat{\mu}_i\rangle_0$ are the expectation values of the initial projections of $\hat{\mu}$ onto each coordinate axis. Similarly,

$$\langle\hat{\mu}_y\rangle(t) = \langle\hat{\mu}_y\rangle_0\cos\omega_0 t + \langle\hat{\mu}_x\rangle_0\sin\omega_0 t$$
$$\langle\hat{\mu}_z\rangle(t) = \langle\hat{\mu}_z\rangle_0$$

Thus, the Heisenberg equation of motion for a single nuclear magnetic moment within a static external magnetic field indicates that $\hat{\mu}$ precesses around $\vec{B}_0$, and the transverse components oscillate in magnitude at the Larmor frequency.

2.4 Classical Derivation of Single-Spin Precession

For spin-1/2 nuclei, the spin dynamics can be accurately represented by a semi-classical toy model analogous to gyroscopic precession. When the angular momentum ($\vec{L}$) of spinning top is off-axis from the gravitational field, it precesses due to the torque ($\vec{\tau}$) provided by the gravitational force at its center of mass. Torque causes a change in angular momentum.

$$\frac{d\vec{L}\,(t)}{dt} = \vec{\tau}\,(t) \tag{2.13}$$

This idea can also be applied to spin angular momentum $\vec{S}$.

$$\frac{d\vec{S}\,(t)}{dt} = \vec{\tau}\,(t) \tag{2.14}$$

The torque experienced by a magnetic moment $\vec{\mu}$ within an external magnetic field $\vec{B}_0$ is defined as:

$$\vec{\tau}\,(t) = \vec{\mu}\,(t) \times \vec{B}_0 \tag{2.15}$$

The magnetic moment is proportional to $\vec{S}$ (Eq. 2.2), and the law of conservation of angular momentum can be expressed as:

$$\frac{d\vec{\mu}\,(t)}{dt} = \gamma \frac{d\vec{S}\,(t)}{dt} = \gamma\vec{\mu}\,(t) \times \vec{B}_0 \tag{2.16}$$

After aligning $\vec{B}_0$ with the z-axis, equations (2.3) and (2.16) yield a familiar set of first-order coupled differential equations.

$$\begin{aligned} \frac{d\mu_x\,(t)}{dt} &= -\omega_0\mu_y\,(t) \\ \frac{d\mu_y\,(t)}{dt} &= \omega_0\mu_x\,(t) \end{aligned} \tag{2.17}$$

$$\frac{d\mu_z(t)}{dt} = 0$$

Similar to the quantum mechanical analysis, the transverse components behave like a 2-dimensional harmonic oscillator, and the z-component remains constant in time.

$$\begin{aligned}
\mu_x(t) &= \mu_{x,0}\cos\omega_0 t - \mu_{y,0}\sin\omega_0 t \\
\mu_y(t) &= \mu_{y,0}\cos\omega_0 t + \mu_{x,0}\sin\omega_0 t \\
\mu_z(t) &= \mu_{z,0}
\end{aligned} \tag{2.18}$$

2.5 Radio-Frequency Pulse and the Rotating Reference Frame

While a magnetic moment is precessing about $\vec{B}_0$, an additional field $\vec{B}_1$ can be applied to further manipulate its direction and tip it away from the z-axis. In order for $\vec{B}_1$ to efficiently interact with a precessing $\vec{\mu}$, $\vec{B}_1$ must have transverse components that oscillate, here with a frequency ω.

$$\vec{B}_1(\omega, t) = B_1(\hat{x}\cos\omega t + \hat{y}\sin\omega t) \tag{2.19}$$

$\vec{B}_1$ is presented as right-circularly polarized, rotating in the counter-clockwise direction about the transverse plane. In order to simplify the analysis, let us move into the rotating reference frame for which $\vec{B}_1$ can be seen as static. This involves the coordinate transformations

$$\begin{aligned}
\hat{x}' &= \hat{x}\cos\omega t + \hat{y}\sin\omega t \\
\hat{y}' &= -\hat{x}\sin\omega t + \hat{y}\cos\omega t \\
\hat{z}' &= \hat{z}
\end{aligned} \tag{2.20}$$

These transformations allow $\vec{B}_1$ to be described as a static field in the $\hat{x}'$ direction, $\vec{B}_1'(\omega, t) = B_1\hat{x}'$.

In the rotating reference frame, the perceived precession frequency (Ω_0) about $\hat{z}'$ due to $\vec{B}_0$ is the difference between ω_0 and ω. Thus, $\vec{B}_0'$ can be written as

$$\vec{B}_0'(\omega,t) = \frac{1}{\gamma}\Omega_0\hat{z}' = \frac{\omega_0-\omega}{\gamma}\hat{z}' \tag{2.21}$$

The effective magnetic field in the rotating frame is the vector sum of $\vec{B}_0'$ and $\vec{B}_1'$

$$\vec{B}_{eff}(\omega,t) = \vec{B}_0'(\omega,t) + \vec{B}_1(\omega,t)' = \frac{\omega_0-\omega}{\gamma}\hat{z}' + B_1\hat{x}' \tag{2.22}$$

From Eq. (2.16), the time-evolution of $\vec{\mu}$ in the rotating reference frame is

$$\begin{aligned}\left(\frac{d\vec{\mu}(t)}{dt}\right)' &= \gamma\vec{\mu}(t)\times\vec{B}_{eff} \\ &= \vec{\mu}(t)\times\left((\omega_0-\omega)\hat{z}' + \omega_1\hat{x}'\right)\end{aligned} \tag{2.23}$$

When $\omega_0 = \omega$, the on-resonance condition is satisfied by $\vec{B}_1$, and $\vec{\mu}$ will rotate about $\hat{x}'$. If ω is different than ω_0, then $\vec{B}_1$ is off-resonance with $\vec{\mu}$; the $\hat{z}'$ component of $\vec{B}_{eff}$ will dominate, and $\vec{\mu}$ will continue to precess about $\hat{z}$ unperturbed.

This resonance condition was the motivation for the title of nuclear magnetic resonance. It was first demonstrated by Rabi in 1938 (84), and he was later awarded the Nobel Prize in Physics for exploiting this resonant behavior to determine the magnetic moments of a variety of nuclei. By tuning $\vec{B}_1$ to specific frequencies, different nuclei will respond based on their unique gyromagnetic ratio. As shown in Table 2.1, common nuclei used for NMR precess at frequencies on the order of MHz, requiring $\vec{B}_1$ to be in the radio-frequency (RF) regime of the electromagnetic spectrum.

2.6 Spin Ensembles, Magnetization, and Hyperpolarization

A typical NMR sample can contain an ensemble of spin-1/2 nuclei on the order of Avogadro's number. Each individual spin's magnetic moment contributes to the macroscopic magnetization $\vec{M}$ (in units of magnetic moment per unit volume). In thermal equilibrium, spins are oriented randomly and they produce a total vector-sum that is essentially zero. As shown in the previous sections, when an external magnetic field is turned on, the spins begin to precess around the z-axis. The oscillating transverse components of the magnetic moments time-average to zero. The z-components, on the other hand, do not necessarily

vanish. The magnitude of $\vec{M}$ is governed by statistical mechanics, and the dynamics of $\vec{M}$ is governed by the density matrix formalism (83; 85).

The density matrix ($\hat{\rho}$) defines the quantum state of the entire ensemble without reference to individual spin states. The operator $\hat{\rho}$ for a spin-1/2 system is defined as

$$\hat{\rho} = \begin{pmatrix} \rho_{\uparrow\uparrow} & \rho_{\uparrow\downarrow} \\ \rho_{\downarrow\uparrow} & \rho_{\downarrow\downarrow} \end{pmatrix} \tag{2.24}$$

Spins can align either parallel ($\uparrow$) or anti-parallel ($\downarrow$) to $\vec{B}_0$, and the probabilities of being in either spin state are represented by $\rho_{\uparrow\uparrow}$ and $\rho_{\downarrow\downarrow}$, respectively. The off-diagonal elements are known as the coherences between the states and may indicate the presence of transverse spin magnetization. The time-evolution of the density matrix is governed by the Hamiltonian of the system.

$$\frac{d\hat{\rho}}{dt} = \frac{-1}{i\hbar}\left[\hat{\rho}, \hat{H}\right] \tag{2.25}$$

This is very similar to the Heisenberg equation of motion (Eq. 2.6) with the exception of the minus sign. This is due to the fact that $\hat{\rho}$ itself is not a time-dependent observable in the Heisenberg picture, but rather a construct of Schrodinger-picture states (86). Nonetheless, the result is a similar oscillatory behavior as previously derived for a single-spin.

The populations of the spin states, $\rho_{\uparrow\uparrow}$ and $\rho_{\downarrow\downarrow}$, can be determined with statistical mechanics. As $\vec{\mu}_z$ can align either parallel ($\uparrow$) or anti-parallel ($\downarrow$) to $\vec{B}_0$, these states correspond to different energy levels as defined by Eq. (2.7).

$$\begin{aligned} E_\uparrow &= -\frac{1}{2}\hbar\gamma B_0 \\ E_\downarrow &= +\frac{1}{2}\hbar\gamma B_0 \end{aligned} \tag{2.26}$$

This splitting of energy levels in the presence of an external magnetic field is known as Zeeman splitting. The energy difference between these two levels ($\Delta E = E_\uparrow - E_\downarrow$) is $-\hbar\gamma B_0$. Using Eq. (2.3), ΔE can be expressed in terms of the Larmor frequency $\Delta E = \hbar\omega_0$, demonstrating that a photon must be oscillating at the Larmor frequency to induce a transition between energy levels.

According to the Boltzmann distribution, the ratio between the number of magnetic moments aligned parallel ($N_\uparrow$) or anti-parallel ($N_\downarrow$) can be expressed in terms of Boltzmann's constant k_B (1.380649 x 10-23 J K^{-1}) and temperature T:

$$\frac{N_\uparrow}{N_\downarrow} = \exp(\frac{-\Delta E}{k_B T}) \tag{2.27}$$

indicating a slight population preference for the low-energy state. The population difference for a sample of N total spins is represented by the polarization P, and it can be determined with Boltzmann statistics.

$$P = \frac{N_\uparrow - N_\downarrow}{N} = \tanh\left(\frac{\hbar\gamma B_0}{2k_B T}\right) \tag{2.28}$$

For practical applications, $\hbar\gamma B_0$ is four orders of magnitude less than $k_B T$, and the polarization can be approximated by

$$P \approx \frac{\hbar\gamma B_0}{2k_B T} \tag{2.29}$$

After determining the disparity in energy-state populations, the magnitude of the bulk magnetization M_{th} is simply the product of the spin density ρ_0, μ_z, and P.

$$M_{th} = \rho_0 \frac{(\hbar\gamma)^2 B_0}{4k_B T} \tag{2.30}$$

At thermal equilibrium for clinical conditions, the disparity in spin-state populations is on the order of 100 ppm (87). As shown in Eq. (2.28), the polarization can increase with the use of large B_0 or low T, but at the expense of biomedical practicality. Instead, polarization can be artificially and substantially increased (by 4-5 orders of magnitude) beyond thermal equilibrium into a hyperpolarized (HP) state using methods such as dissolution dynamic nuclear polarization (88), parahydrogen induced polarization (89), and spin-exchange optical pumping (SEOP) (90).

SEOP excels at hyperpolarizing large amounts of noble gases, approaching unity polarization for ^{129}Xe (91; 92). SEOP is a two-stage process including the optical pumping of an alkali metal followed by spin-exchange via collisions between the alkali metal and the noble gas, creating a HP noble gas. First, left-handed circularly polarized laser light is targeted at an optical cell containing the noble gas of interest, a vaporized alkali metal, and a buffer gas. Rubidium (Rb) is commonly chosen as the alkali metal because

it has a D_1 transition at 794.7 nm for which high-powered light sources are readily available (90). When the laser light is tuned to this wavelength, a D_1 transition occurs according to the quantum mechanical selection rule $\Delta l = \pm 1$, resulting in a transition from the state ${}_2S_{-1/2} \rightarrow {}_2P_{+1/2}$. Collisions with the buffer gas, typically N_2, quenches the excited state of Rb and induces relaxation to the ground state without emission of photon, avoiding the effects of radiation trapping (93). As Rb relaxes, it populates $m_s = \pm\frac{1}{2}$ with equal probability. Since the circularly polarized laser is continuously depopulating ${}_2S_{-1/2}$, the population eventually becomes polarized to the ${}_2S_{+1/2}$ state.

The polarization of the optically-pumped alkali metal atoms is then transferred to the noble gas atoms through spin-exchange processes. The transfer of angular momentum occurs either through van der Waals interactions or binary collisions. The former involves the interactions within a short-lived cluster made by the alkali metal vapor, noble gas, and buffer gas (90). The latter, binary collisions between the alkali metal electron spins and the noble gas nuclear spins, is the dominant mechanism for transferring angular momentum via Fermi-contact hyperfine interactions (87).

The two main setups used to create HP ^{129}Xe gas are stopped-flow and continuous-flow. Stopped-flow production is a batch method that hyperpolarizes a single volume of ^{129}Xe gas at a time. Even though stop-flow production is capable of near-unity polarization (92), clinical applications using HP ^{129}Xe gas utilize the continuous-flow method, which is capable of producing much larger volumes of HP ^{129}Xe gas in a shorter amount of time compared to the batch method (94). Continuous-flow production has achieved polarization as high as 84% (95; 96), although typical polarizations achieved in our lab range between 10% – 20%, sufficient for *in vivo* usage (11; 46; 97). There is a significant discrepancy between the continuous-flow polarization achieved in practice and the theoretical value, and work is also being done to reconcile the difference (98; 99).

In contrast to hyperpolarization, the opposite scenario in which the populations of $N_\uparrow$ and $N_\downarrow$ are equalized, effectively destroying the bulk magnetization, is known as saturation. The process of saturation and its role in the chemical exchange saturation transfer MR experiments will be discussed extensively in Chapter 3.

2.7 Relaxation

Hyperpolarization establishes a non-stable bulk magnetization, and over time, the excess magnetization will decay back to its thermal equilibrium state. This process is known as relaxation; following a perturbation, the longitudinal and transverse components of the bulk magnetization reestablish a steady state. Revisiting Eq. (2.16) and summing over μ_i to represent the total magnetization $\vec{M}$, the set of differential equations can be separated into longitudinal and transverse components.

$$\begin{aligned} \frac{dM_{\parallel}(t)}{dt} &= 0 \\ \frac{dM_{\perp}(t)}{dt} &= \gamma M_{\perp}(t) \times \vec{B}_0 \end{aligned} \tag{2.31}$$

As they are written here, this set of differential equations represents the dynamics associated with non-interacting nuclei. This does not accurately represent an ensemble of spins, which are essentially tiny magnets in thermal motion, exchanging energy and influencing the local magnetic field (83).

Longitudinal relaxation is also known as spin-lattice relaxation, harkening back to the early days of NMR that focused on its application on solids and the exchange of energy between nuclear spins within a crystal lattice (42). Many applications of NMR today deal with liquids and gases, and reference to a lattice is usually dropped in favor of simply acknowledging build-up of longitudinal magnetization parallel to $\vec{B}_0$. The rate of change of M_z is proportional to the difference $M_z(t) - M_{th}$ (100).

$$\frac{dM_z(t)}{dt} = -\frac{1}{T_1}\left(M_z(t) - M_{th}\right) \tag{2.32}$$

When $M_z = M_{th}$, a stationary solution is satisfied. Figure 2.2 shows the growth and decay as a result of turning $\vec{B}_0$ on and off. The proportionality constant T_1 is the characteristic timescale for the longitudinal magnetization recovery, and it is determined empirically based on the spin environment for various nuclei.

Suppose an RF-pulse rotates the bulk magnetization into the transverse plane. Each individual spin in the ensemble experiences the same flip angle and will continue to precess around $\vec{B}_0$ at its Larmor frequency. The synchronization of precession is dependent on the uniformity of the external magnetic field throughout the sample. When dealing with interacting nuclei, each individual spin perturbs its local field, leading to slight changes in precession frequency and disrupting synchrony. Eventually, the transverse components of the individual spins will be randomly oriented, and the bulk magnetization will vanish.

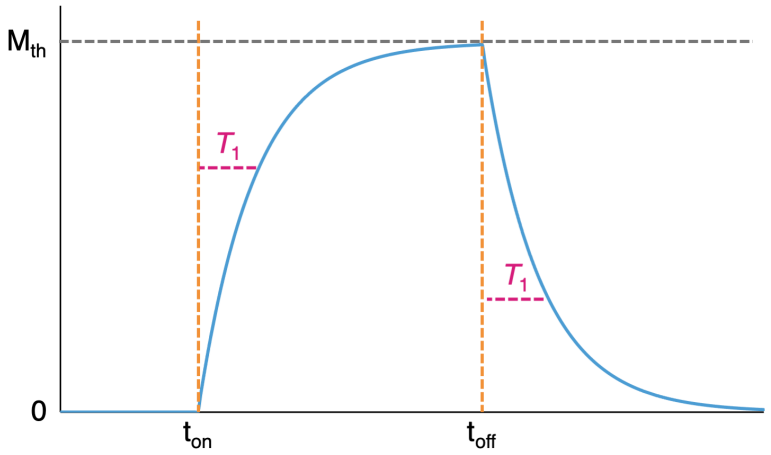

Figure 2.2: T_1 relaxation. In thermal equilibrium, spins are randomly oriented and the net magnetization is 0. When an external magnetic field $B_0\hat{z}$ is turned on at t_{on}, the spins longitudinally orient themselves according to Boltzmann statistics. This growth rate increases exponentially with the time constant of T_1. After a sufficiently long time, the magnetization reaches thermal equilibrium (M_{th}). When the perturbing external field is turned off at t_{off}, the spin ensemble decays away from M_{th} according to T_1.

This transverse relaxation is also known as spin-spin relaxation. Transverse relaxation manifests in the dynamical equations as a decay rate term.

$$\frac{dM_{\perp}(t)}{dt} = \gamma M_{\perp}(t) \times \vec{B}_0 - \frac{1}{T_2} M_{\perp}(t) \tag{2.33}$$

T_2 is the characteristic timescale for phase decoherence. Field inhomogeneity is present in most practical samples due to differences in magnetic susceptibilities between compartments, and it is characterized by T_2'. The effects of microscopic and macroscopic field inhomogeneities can be compounded into an apparent transverse relaxation time T_2^*.

$$\frac{1}{T_2^*} = \frac{1}{T_2} + \frac{1}{T_2'} \tag{2.34}$$

While T_2 may be more intrinsic to the molecular makeup of the sample, T_2^* is what is observed in experiment. In general, T_2^* is always less than T_2, causing a faster decay in magnetization.

Eqs. (2.30) and (2.31) can be combined to form the Bloch equation.

$$\frac{d\vec{M}(t)}{dt} = \gamma \vec{M}(t) \times \vec{B}_0 - \hat{R}\left(\vec{M}(t) - \vec{M}_{th}\right) \tag{2.35}$$

where $\hat{R}$ is the relaxation rate matrix defined as:

$$\hat{R} = \begin{pmatrix} \frac{1}{T_2} & 0 & 0 \\ 0 & \frac{1}{T_2} & 0 \\ 0 & 0 & \frac{1}{T_1} \end{pmatrix} \tag{2.36}$$

Felix Bloch first published this famous nuclear spin dynamics equation in 1946, and initially referred to the phenomenon as nuclear induction (100). In 1958, Harden McConnell modified the Bloch equation to include chemical exchange between magnetically distinct environments (101), which will be discussed thoroughly in Chapter 3.

2.8 The NMR Experiment

As the net magnetic moment of a sample precesses, its associated magnetic field also oscillates. Due to Faraday's Law of Induction, the changing magnetic field can be probed with a coil. Suppose spins precess about $B_0\hat{z}$. After applying an RF-pulse perpendicular to $\hat{z}$, the spins are tipped into the transverse (xy) plane. A coil within a circuit is strategically positioned on a plane perpendicular to the transverse plane (yz, for example). As the net magnetic moment continues to precess around $\hat{z}$, the flux of the transverse components through the coil's surface is continually changing. The fluctuating magnetic field produces an electromotive force, and current begins to oscillate within the circuit. Through Ohm's law, the oscillating current is related to an oscillating voltage, which is easily detectable. As the magnetization of the spin ensemble begins to relax, the amplitude of the voltage decays due to T_2 relaxation. The resulting signal is known as the free-induction decay (FID) (Figure 2.3).

The FID is a time-domain signal and can be made up of many different frequencies compiled together. The various frequency components can be extracted and easily visualized after Fourier transformation. The Fourier transformation allows oscillating signals to be represented as a linear combination of complex exponentials, and each constituent frequency appears as a peak in the frequency-domain. The collection of peaks in the frequency-domain is the NMR spectrum. Ideally, these peaks have a Lorentzian lineshape, following the mathematical form:

$$S(\omega) \;\; M_0 \frac{\lambda}{\lambda^2 + (\omega - \omega_0)^2} \tag{2.37}$$

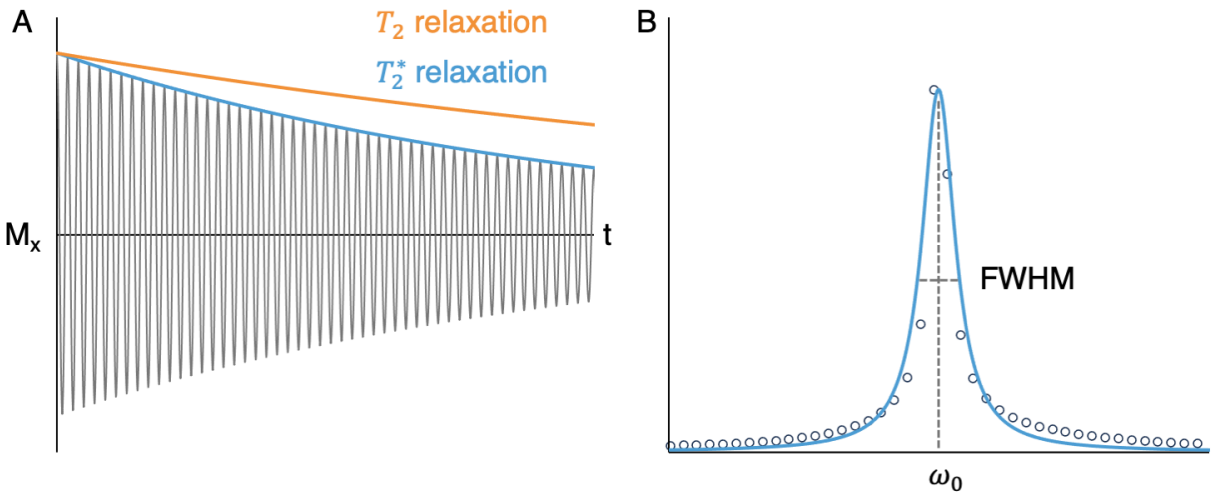

Figure 2.3: Fourier transforming the FID produces the NMR spectrum. (A) The time-domain signal of the transverse magnetization is the FID. This signal decays over time according to T_2^*, a result of field inhomogeneities produced in the laboratory. These experimental inhomogeneities induce a faster decay than the intrinsic T_2 relaxation. (B) The Fourier transform of the FID produces the NMR spectrum in the frequency domain. Lorentzian peaks appear centered at component frequencies, producing characteristic spectral signatures. T_2^* manifests itself in the peak in the form of the FWHM.

Each of these parameters corresponds to specific characteristics of a spin-compartment. The Larmor frequency ω_0 represents the center of the Lorentzian peak along the ω-domain. Thus, the location of a peak in the spectrum can identify the presence of a molecule due to its intrinsic resonance frequency. The decoherence decay rate constant (λ) is inversely proportional to T_2^*, $\lambda = 1/T_2^*$, and makes itself apparent in the broadness of the peak as the full-width at half-max ($FWHM = 2/T_2^*$, in units of rad/s). M_0 corresponds to the peak intensity. For samples presenting multiple peaks, provided the species have relatively similar T_2 values, the comparison between peak intensities can provide insight on relative concentrations. For example, if a peak is twice the height of another peak, then the concentration of the former is roughly double that of the latter given that M_0 of either species is directly related to the spin density (Eq. 2.30).

Spin-compartments are often identified by comparing the relative frequency difference when compared to a reference peak or frequency (ω_{ref}). Since the precession frequency is directly proportional to the external magnetic field (Eq. 2.3), the frequency shift between spin-species is also field-dependent. In order to communicate a meaningful frequency difference across NMR spectrometers of varying field strengths, a ratio is used to eliminate field-dependence.

$$\delta = \frac{\omega_0 - \omega_{ref}}{\omega_{ref}} \tag{2.38}$$

This is known as the chemical shift (δ). Larmor frequencies are often on the order of MHz (Table 2.1), and the difference $\omega_0 - \omega_{ref}$ is often on the order of Hz. As such, it is convenient to refer to chemical shifts in units of parts per million (ppm). If the chemical shift is negative, then $\omega_{ref} > \omega_0$ and ω_0 is considered to be shifted upfield from ω_{ref}. Conversely, if the chemical shift is positive, ω_0 is considered to be shifted downfield from ω_{ref}.

A chemical shift is caused by the electron cloud surrounding a nucleus. The electron cloud surrounding a nucleus is able to react to an applied magnetic field and provide shielding by creating an opposing field according to Lenz's law. This decreases the local magnetic field, and, consequently, its shifts precession frequency upfield. When the nucleus is in the presence neighboring groups that are particularly electronegative, the electron cloud can be skewed and the electron-density decreases. This results in deshielding of the nucleus, and δ will shift downfield. ^{129}Xe is a particularly sensitive nucleus and can be detected over a range that spans more than 200 ppm, (20-fold greater than ^{1}H (102; 103)) due to its large electron cloud. Typical ^{129}Xe chemical shifts for various molecules and tissues are listed in Table 2.2, referenced to signal corresponding to ^{129}Xe dissolved in water. ^{129}Xe is an ideal NMR probe because it is versatile and sensitive to many unique biological compartments. The apparent chemical shift can also be influenced by magnetic susceptibility and compartmental geometry that perturb the local field, and this behavior will be discussed in depth in Chapter 4.

Environment	Chemical Shift [ppm]
Phosphate Buffered Saline	0
Cucurbit[6]uril (CB[6])	-71.8
Perfluorooctyl Bromide (PFOB)	-90
Decafluorobutane (DFB)	-138
Gas (cylindrical PEEK tubing)	-192
Gas (microbubble, MB)	-194.6

Table 2.2: Typical chemical shifts of ^{129}Xe referenced to xenon dissolved in phosphate buffered saline.

In 1966, Richard Ernst first demonstrated Fourier transform NMR spectroscopy (104), which was initially met with pushback on publication and manufacturing (105). Eventually, commercial Fourier transform spectrometers were adopted by companies like Bruker and Varian, and Richard Ernst was awarded the Nobel Prize in Chemistry in 1991 for his contributions to the field. Since then, NMR spectroscopy has become a standard for identifying chemical composition. Modern high-field NMR spectrometers are

extremely sensitive to small chemical shifts and produce high-resolution spectral signatures, and individual spin-species can be directly observed. Although, this depends on each molecule being present at concentrations that are detectable above the noise level. For example, mM concentrations of HP ^{129}Xe are easily detected (106) and sensitivity to chemical shifts can provide accurate thermometry measurements (11; 48). As molecular concentrations decrease, it becomes more difficult to distinguish NMR signals from the background noise. In the following chapter, I will introduction an indirect detection scheme where dilute molecules imprint their presence onto a large, detectable signal by transferring their magnetization through chemical exchange.

CHAPTER 3: CHEMICAL EXCHANGE SATURATION TRANSFER WITH HP ^{129}XE

3.1 Chemical Exchange NMR

The acquisition of an NMR spectrum provides a magnetic snapshot of the sample within an acquisition time on the order of ms. Outside of the context of dynamic studies, one would hope that a spectrum of a stable solution would record a stationary state, and all of the atoms would have settled into their compartments producing very sharp and distinctive peaks. Imagine a large family getting together for a group photo at their family reunion. Everyone takes their spot and the photographer's countdown begins. The flash goes off, and of course, someone is blinking, someone is not looking at the camera, and a pair of cousins are switching spots. All of this commotion is caught in the image, making certain family members blurry or out of focus. While the macroscopic family was positioned for the photo, the microscopic motion was imprinted onto the image. Similarly, for NMR spectroscopy, even when a sample is in macroscopic equilibrium, the atoms are in thermal motion and may move between magnetically distinct environments, and peaks broaden and shift. This process is known as chemical exchange, and it is a common artifact in NMR spectra.

As shown in Chapter 2, the compartment in which a nucleus resides affects its precession frequency and its relaxation properties. Thus, the interchange between magnetically distinct environments can have a substantial effect on its spin dynamics. Changes in molecular stereochemistry can alter chemical shifts and produce conformational chemical exchange (107). Another mechanism, and the scope of this thesis, involves the atom, thus the nuclear spin, passing between physical boundaries (108). Typically, this involves exchange between a large solvent pool (Pool A) and molecular carriers (43; 109; 110; 111) (Pools B, C, etc. as needed (112)).

The exchange between pools can be modeled on a spin-by-spin basis using Monte Carlo methods (113). The transition probability per unit time is equal to the exchange rate k. The probabilistic nature of these transitions results in chaotic trajectories for each individual spin. The accumulation of precession phase is dependent on the amount of time each spin spends in a pool rotating at a specific frequency.

Thus, over time, a higher number of transitions will decrease the coherence of an ensemble of spins. As k increases, the peaks in the ensemble's NMR spectrum would consequently broaden due to the wide distribution of frequencies. This is particularly detrimental to spectral resolution where high k may cause nearby peaks to coalesce. Coalescence between neighboring peaks (separated by δ) occurs when k is on the order of the NMR timescale (83; 107; 114).

$$k_{coalescene} = \frac{\delta}{\sqrt{2}} \tag{3.1}$$

In order for peaks to be uniquely resolved, the ideal exchange rate is $k << \delta$. Factors such as temperature (107) and diffusivity (115; 116; 110; 111) are directly related to k, and they can be manipulated to help resolve the effects of chemical exchange.

It is important to highlight the difference between chemical exchange and chemical reaction. While both processes are microscopically dynamic, on a macroscopic scale, chemical exchange appears to be a process that characterizes the dynamic equilibrium of the spin system. In order words, every time a spin leaves one pool, another spin comes and takes its place. This switching of occupants does not alter the chemical construction of the sample, and it is not detected on a macroscopic scale outside of the NMR spectrum. This balance requires that the individual population proportions are invariant over time (107; 113). Let f_i represent the fraction of the total number of spins that reside in Pool i. For a 2-pool system of equal populations, $f_A = f_B = 0.5$, and it will remain that way for all time. In order to maintain this equilibrium, the respective exchange rates must be related by the same proportion (107; 112).

$$\frac{k_{AB}}{k_{BA}} = \frac{f_B}{f_A} \tag{3.2}$$

k_{AB} is the exchange rate from Pool A to Pool B, and k_{BA} is the exchange rate from Pool B to Pool A. This ratio can also be extracted from the relative peak intensities of the pools.

3.2 Chemical Exchange Saturation Transfer

As nuclei exchange between magnetically different environments, their precession frequency changes. Thus, according to Eq. 2.23, an individual spin will respond to different RF-pulse frequencies depending on the compartment in which it resides when B_1 is applied. For example, if a spin is in Pool A precessing

at a frequency ω_A, it will be affected by B_1 only if B_1 is also oscillating near ω_A. Spins in Pool B precessing at ω_B are blind to this B_1, and they are unaffected by this RF-pulse provided that ω_A and ω_B are sufficiently separated comparted to the bandwidth of B_1. When δ is large or k is below the coalescence threshold (Eq. 3.1), selectively manipulating a spin is relatively straightforward. In a standard NMR experiment, a large and unwanted signal can be selectively destroyed with B_1 on-resonance with that pool, attenuating its magnetization before signal acquisition. This is a process known as presaturation where the on-resonance B_1 induces transitions between energy levels and gradually decreases the polarization (Eq. 2.28). Once the populations of $N_\uparrow$ and $N_\downarrow$ are equal, the polarization and magnetization are 0, and the spin pool is saturated.

Chemical exchange is an ongoing process, and spins that may have been selectively saturated in one pool may exchange into the other (Figure 3.1). As a result, selective presaturation may result in mutual signal attenuation between pools in chemical exchange. Pool A may be the target of the RF-pulse, but those depolarized spins exchange into Pool B. The efflux from Pool A is countered with influx from Pool B, and the replenished spins are, in turn, saturated as well. This means that, even though Pool B was not the target, this transfer of magnetization leaves an imprint on its signal. This effect is a hallmark of chemical exchange between pools.

This magnetization transfer mechanism is particularly useful for solutions in which $f_A >> f_B$, which is usually the case for extremely dilute molecules (Pool B) that exchange protons with the 110 M water molecules of the solvent (Pool A) (112; 117; 118). In these instances, a direct NMR spectrum would show a large peak from Pool A, but show little to no trace of Pool B due to its low spin density. The clever combination of presaturation and chemical exchange can reveal the hidden pool through the indirect detection scheme known as chemical exchange saturation transfer (CEST) (43; 117; 119).

CEST is an NMR technique that can increase detection sensitivity by several orders of magnitude. It relies on on-resonance saturation of the dilute spin pool and then monitoring its effect on the solvent pool. When compared to an off-resonance spectrum, the on-resonance spectrum will show a decrease in the solvent signal. This loss in signal is indicative of the presence of the dilute pool, and the B_1 frequency that produces the CEST effect is precisely the precession frequency of Pool B. Determining ω_B, the resonance frequency of Pool B, is as informative as a directly observing a sharp peak on an NMR spectrum.

The resonance frequency of Pool B may not be known *a priori*. In this case, sequential experiments are done,whereby a series of NMR spectra are acquired at variable B_1 frequencies ω. The intensity of the

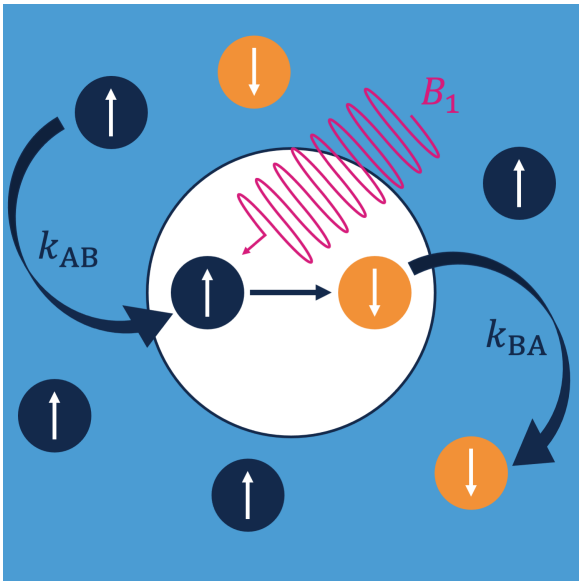

Figure 3.1: CEST mechanism. Spins can undergo chemical exchange between a solvent pool (Pool A, blue) and a dilute molecular carrier (Pool B, white). Pool A and Pool B are magnetically different environments, and an RF-pulse (B_1) can be tuned to only affect the spins in Pool B. B_1 saturates the spins while in Pool B. The depolarized spins then exchange into the solvent at an exchange rate of k_{BA}. At the same time, spins from Pool A exchange into Pool B at an exchange rate of k_{AB}, which in turn get depolarized. When B_1 is tuned to ω_B, this process results in a decrease in the magnetization of the large solvent pool.

peak corresponding to Pool A, normalized to its intensity without any presaturation, is plotted as a function of ω. This plot is known as the Z-spectrum (Figure 3.2). As opposed to the NMR spectrum containing peaks, the Z-spectrum has valleys. The primary valley at 0 ppm is usually referenced as ω_A, and should have complete signal loss due to the direct on-resonance saturation of Pool A. Any valleys away from 0 ppm correspond to the frequencies of pools that are in chemical exchange with Pool A. Figure 3.2 shows a simulated Z-spectrum with the following parameters (120): B_0 =11.7 T, continuous wave (cw) B_1 =5 μT, t_{sat} =2 s, δ_A =0ppm, δ_B =-150 ppm, f_A =1, f_B =0.01, k_{BA} =2000 Hz, $T_1^A = T_1^B$ =40 s, $T_2^A = T_2^B$ =1/20 s. These parameters will also be used for all of the simulated Z-spectra in this Chapter, unless stated otherwise. Simulations were generated using the Bloch-McConnell solution discussed in Section 3.5.

The chemical exchange dynamics affect a Z-spectrum in ways that are very similar to how they affect an NMR spectrum. The exchange rate between Pool B and Pool A (k_{BA}) is crucial for the efficient transfer of magnetization, needed to produce substantial signal reduction. First, k_{BA} should be slow on the NMR timescale in order to ensure exchange between magnetically distinct environments and allow for selective saturation (121). The smaller the chemical shift (δ_B), the more difficult it is to differentiate between val-

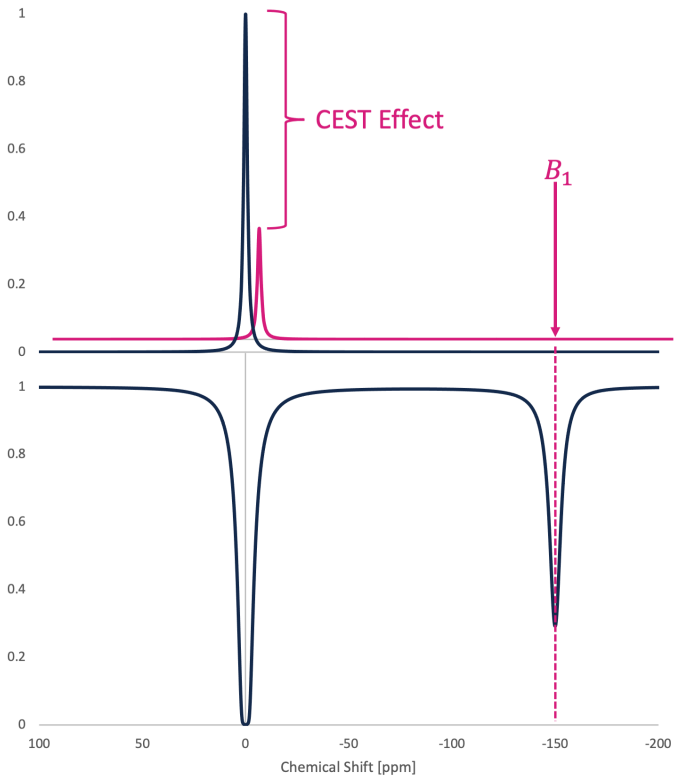

Figure 3.2: The CEST effect on and NMR spectrum and the Z-spectrum. (Top) The NMR spectrum shows a single, large peak at 0 ppm. When B_1 is applied at -150 ppm, the large peak becomes attenuated due to the CEST effect facilitated by a dilute pool that resonates at -150 ppm with respect to the large, detection pool. (Bottom) If ω_B is not known *a priori*, then it can be identified with a Z-spectrum. The frequency of B_1 is varied across the spectral width, and the intensity of the detection peak is monitored. The valley in the Z-spectrum at -150 ppm corresponds to the hidden signal in the NMR spectrum. Thus, CEST allows for the indirect detection of dilute molecules.

leys in the Z-spectrum (Figure 3.3). For ^{1}H CEST experiments, it is common for δ_B to only be a few ppm. Even with a small chemical shift, it is not a lost cause. In order to extract the CEST effect, a magnetization transfer ratio asymmetry analysis can be used (117). The valleys should be Lorentzian in shape, and asymmetry is due to the coalesce of valleys and the CEST effect. At the same time, CEST is in constant competition with relaxation, and k_{BA} must be fast compared to the longitudinal relaxation rates of Pool A and Pool B ($R_1^{A,B}$). This ensures that the effects of saturation on the spins can have an appreciable effect on the bulk magnetization before thermal equilibrium is reinstated (43; 114). k_{BA} should be considered as a Goldilocks parameter since it must not be too slow nor too fast in order to facilitate efficient CEST contrast (Figure 3.4).

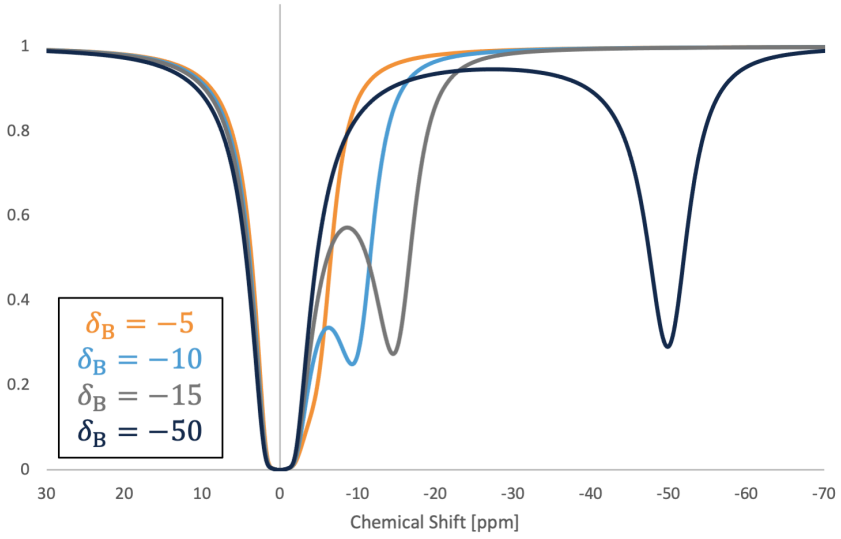

Figure 3.3: δ_B dependence. Chemical exchange may cause Z-spectrum valleys to coalesce, and larger chemical shifts can alleviate this effect. If the exchange rate is slow on the NMR timescale, separate valleys are easily resolved, and pools can be selectively saturated. For ^{1}H CEST, chemical shifts are only a few ppm, similar to δ_B=-5 ppm. It is difficult to directly resolve the valleys, but a magnetization transfer ratio asymmetry analysis can extract the CEST effect from the asymmetry in the Lorentzian shape.

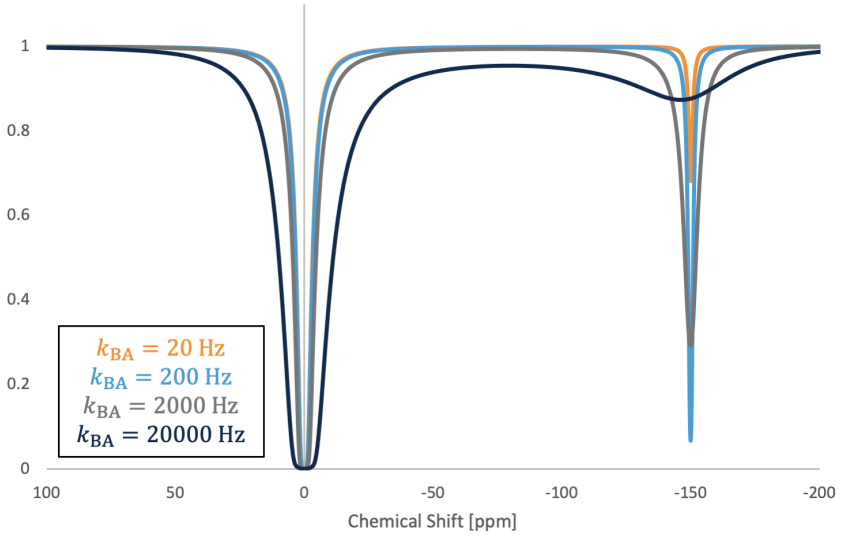

Figure 3.4: Exchange rate dependence. The exchange rate is a Goldilocks parameter. Here, as k_{BA} increases, contrast at -150 ppm increases to an inflection point and then decreases. If k_{BA} is too fast, then even if the valleys are sufficiently separated to avoid coalescence, the spins do not spend enough time in Pool B to be significantly affect by B_1. On the other hand, if k_{BA} is too slow, then not enough depolarized spins will exchange into Pool A to saturate the spin population disparity.

Since the flip angle is directly related to B_1 (Figure 3.5) and the saturation time t_{sat} (Figure 3.6), those parameters also influence the degree of saturation and the amount of CEST contrast that is produced. While increasing both of these parameters will ensure significant CEST contrast, the act of doing so yields diminishing returns. B_1 is usually on the order of μT, and as it is increased, Figure 3.5 shows the broadening of the valleys, and spectral sensitivity decreases, which is especially detrimental for small δ_B. Increasing t_{sat} would also increase contrast, but prolonging exposure to B_1 can have negative effects on biological systems. This is relevant for clinical MRI scanners that place limits on the specific absorption rate (SAR) to avoid excessive tissue heating from RF-irradiation. It is not necessary to use B_1 and t_{sat} excessively. It has been shown that the optimal cw B_1 is related to the exchange rate, $B_1 = 5k_{BA}/\gamma$. This RF strength can still achieve 96% contrast while maintaining spectral sensitivity (122). Figure 3.6 shows that further increasing t_{sat} loses its effect, and even doubling t_{sat} from 5 s to 10 s produces very little increase in contrast. A rule of thumb is $t_{sat} < T_1^A$ (122).

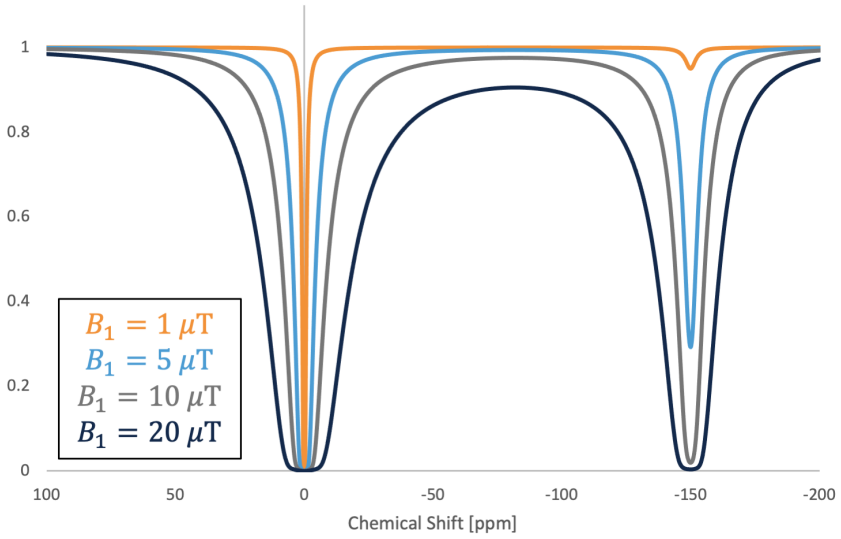

Figure 3.5: RF-pulse strength dependence. Increasing B_1 will saturate the spins in Pool B more rapidly. But this comes at the cost of spectral sensitivity. As shown here, as B_1 increases, the valleys broaden. For small chemical shifts, excessively increasing B_1 is detrimental. The optimal B_1 is $5k_{BA}/\gamma$.

Even with these power limitation in mind, clinical scanners still enforce strict limits on cw RF-pulses. Instead, B_1 can be transmitted as a train of short, shaped pulses (97; 122; 123). This helps to ameliorate the risk of RF heating. The successful translation to clinical imaging has allowed ^{1}H CEST contrast to image endogenous metabolites that can provide functional information in brain (124; 125; 126; 127), breast

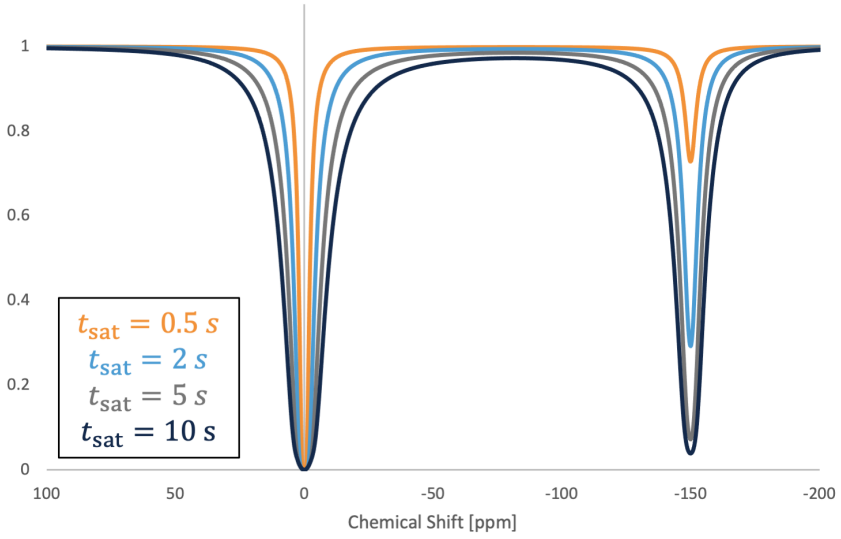

Figure 3.6: t_{sat} dependence. Increasing t_{sat} loses its efficacy at a certain point as shown here, where doubling t_{sat} from 5 s to 10 s shows very little difference in contrast. t_{sat} should be kept to a minimum in order to avoid excessive exposure to RF irradiation.

(128; 129), and prostate (130; 131) tumors. Once ω_B of the contrast agent is determined with spectroscopy, imaging only requires on- and off-resonance images, where the off-resonance frequency is chosen to be $-\omega_B$ in order to minimize symmetric effects of the saturation profile. Images are masked by an intensity threshold to minimize the contribution of noise (132), and contrast maps are generated by pixel-by-pixel subtraction.

3.3 HyperCEST

Another requirement is that a large fraction of the total spins must participate in the exchange process. In a typical ^{1}H CEST experiment, the ^{1}H solvent concentration is on the order of 100 M. This requires at least mM concentrations of the solute in order for a significant portion of the total spin population to undergo chemical exchange (110; 117). This is reflected in the parameter f_B, and in general, increasing f_B increases the contrast achieved by on-resonance saturation of Pool B (Figure 3.7). As f_B approaches f_A, the Z-spectrum shows no preference between spin pools, and irradiation of either pool produces equal signal loss in the other. Although, at that point, it is most likely the case that both peak appear in an NMR spectrum at equal intensities, and CEST is no longer necessary.

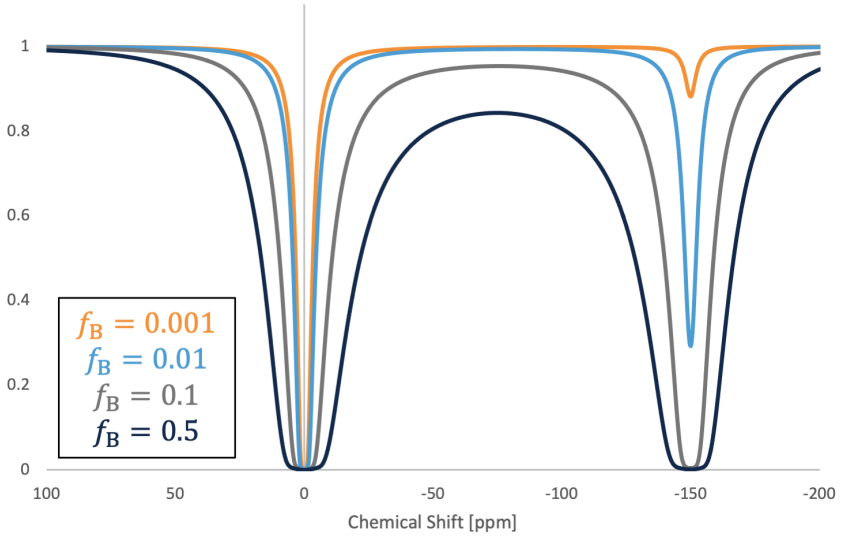

Figure 3.7: f_B dependence. CEST contrast depends on the proportion of total spins that participate in chemical exchange. In order for a significant number of spins to be depolarized, the fraction of the total spins in Pool B (f_B) must be sufficient. There are multiple methods to increasing f_B: increase the concentration of the molecular carrier in solution, increase the carrying capacity per carrier, or decrease the concentration of the detection nucleus on the solvent pool. By using hyperCEST with large carriers capable of enclosing millions of ^{129}Xe atoms, f_B increases even at low carrier concentrations due to the low concentration of HP ^{129}Xe in the solvent.

To increase f_B, CEST can be combined with HP ^{129}Xe. ^{129}Xe is a nontoxic and inert gas with a large electron cloud, which makes it extremely sensitive to its chemical environment. It has a large chemical shift range (>200 ppm), providing leeway for k_{BA} to be slow on the NMR timescale. Its relatively high solubility in tissues makes ^{129}Xe an ideal biological probe (103). ^{129}Xe has no background signal in natural samples and must be introduced exogenously through bubbling, injection, or inhalation. Upon inhalation, it accumulates in tissues at hundreds of μM to mM concentrations (116). At these very low concentrations, its detection requires nuclear spin hyperpolarization, generally achieved via SEOP. SEOP leads to a more than 10^4-fold increase in nuclear spin polarization, amplifying the signal of ^{129}Xe spins present at mM concentrations to levels comparable to that of water ^{1}H in tissues (110; 118). At mM concentrations of ^{129}Xe in the detectable Pool A, CEST can tolerate much lower carrier concentrations for Pool B than ^{1}H CEST, maintaining a comparable if not larger f_B.

This technique, coined hyperCEST, was first demonstrated in 2006 (43). Since then, synthetic ^{129}Xe-binding cages like cryptophanes (CryA, 6Å diameter) (133), pillar[5]arenes (P5A, 6Å diameter) (134), and cucurbit[6]uril (CB[6], 4Å diameter) (135) have been studied as hyperCEST agents because they

rapidly and reversibly bind single ^{129}Xe atoms (4Å diameter) (135). CryA has shown the hyperCEST effect at 1 nM concentrations (136), and hundreds of fM when combined with a bacteriophage scaffold (137). While CryA are quite difficult to synthesize (138), the biocompatible (139; 140; 141; 142) and commercially available CB[6] has shown hyperCEST sensitivity down to pM concentrations (135) and has been determined to be kinetically superior to CryA as a hyperCEST agent (143). HyperCEST with CB[6] was first demonstrated in vitro with whole blood (144), and recently, also *in vivo*, but at a relatively high concentration of 10 mM (123). While Hane et al. reported no toxic effects 30 minutes post-injection at this dosage, it should be noted that CB[6] is prone to bind a wide variety of analytes (145), so its high required dose is a reflection of its inefficiency *in vivo*.

These previous studies have highlighted the importance of developing more efficient hyperCEST agents – larger hosts that encapsulate and influence multiple ^{129}Xe atoms at a time to optimize exchange dynamics and saturation. Specifically, by breaking the 1:1 stoichiometry, the number of ^{129}Xe atoms subjected to depolarization is expected to increase while keeping the carrier concentration to a minimum. Indeed, some hyperCEST agents such as naturally occurring gas vesicles (GV) produced by aquatic microbes (110; 118; 146) and liquid-core perfluorocarbon (PFC) nanoemulsions (116; 109) accommodate thousands of ^{129}Xe atoms per host, and have exhibited an hyperCEST effect at pM concentrations.

It is clear that there is a wide variety of molecular agents that facilitate hyperCEST. In order to evaluate their efficacy, their kinetic parameters can be extracted from Z-spectra. In the following sections, the dynamical equations of spins in chemical exchange are presented along with methods to produce both numerical and analytical solutions. With these solutions in-hand, an analysis known as quantitative hyperCEST (112) (qHyperCEST) can be used to fit Z-spectra to extract relevant exchange parameters and to simulate experimental parameters to determine optimal experimental protocol (122; 147).

3.4 The Bloch-McConnell Equations

In Chapter 2, the Bloch equation (Eq. 2.35) was introduced as a set of ordinary differential equations used to model the magnetization dynamics including longitudinal and transverse relaxation for a single spin pool. Here, it is presented in its general form with the inclusion of a time-dependent presaturation RF-pulse $\vec{B}_1\,(t)$.

$$\frac{d\vec{M}(t)}{dt} = \gamma\vec{M}(t) \times \left(\vec{B}_0 + \vec{B}_1(t)\right) - \hat{R}\left(\vec{M}(t) - \vec{M}_{th}\right) \tag{3.3}$$

In the case of hyperCEST, spins exchange between magnetically different pools and magnetization is transferred. As a result, the Bloch equations must be modified to describe the magnetization of multiple pools by including exchange rate terms.

In 1957, Harden McConnell first introduced these modifications for a 2-pool system (101).

$$\frac{d\vec{M}^A(t)}{dt} = \gamma\vec{M}^A(t) \times \left(\vec{B}_0 + \vec{B}_1(t)\right) - \hat{R}^A\left(\vec{M}^A(t) - \vec{M}^A_{th}\right) - k_{AB}\vec{M}^A(t) + k_{BA}\vec{M}^B(t)$$

$$\frac{d\vec{M}^B(t)}{dt} = \gamma\vec{M}^B(t) \times \left(\vec{B}_0 + \vec{B}_1(t)\right) - \hat{R}^B\left(\vec{M}^B(t) - \vec{M}^B_{th}\right) - k_{BA}\vec{M}^B(t) + k_{AB}\vec{M}^A(t) \tag{3.4}$$

These are known as the Bloch-McConnell (BM) equations. It is assumed that the magnetizations of Pool A ($\vec{M}^A$) and Pool B ($\vec{M}^B$) are coupled only in the sense of magnetization transfer via chemical exchange, and the effect of relaxation is confined to each specific pool. For example, as spins leave Pool A, they carry their magnetization with them, and $\vec{M}^A$ decreases at a rate of $k_{AB}\vec{M}^A$. Similarly, as spins enter Pool A from Pool B, $\vec{M}^A$ increases at a rate of $k_{BA}\vec{M}^B$. While spins remain in Pool A, they relax according to the Bloch equation governed only by T_1^A and T_2^A.

The initial magnetizations M_0^A and M_0^B are proportional to their spin-densities similar to Eq.3.2.

$$\frac{M_0^B}{M_0^A} = \frac{f_B}{f_A} \tag{3.5}$$

When $f_B << f_A = 1$, Eqs. 3.2 and 3.5 simplify to $k_{AB} = f_B k_{BA}$ and $M_0^B = f_B M_0^A$, respectively.

It is very straight forward to apply these modifications to more complex systems of 3 or more pools. For each additional pool, the rate of change of $\vec{M}^i$ will essentially be identical to Eq. 3.4, adjusting for its own exchange rates into and out of Pool A as well as the scaling according to f_i for Eqs. 3.2 and 3.5. It is assumed that each additional pool is present at a low concentration and exchanges directly only with the solvent pool (147; 148; 149). As a result, Eq. 3.4 will be adjusted by including influx and efflux terms for each additional pool. This approach will be discussed in more detail in Chapter 6.

For a 2-pool system, the vector components of the coupled differential equations will be written out here in their entirety.

$$\frac{dM_x^A(t)}{dt} = -\omega_A M_y^A(t) - R_2^A M_x^A(t) - k_{AB} M_x^A(t) + k_{BA} M_x^B(t)$$

$$\frac{dM_y^A(t)}{dt} = \omega_A M_x^A(t) + \omega_1 M_z^A(t) - R_2^A M_y^A(t) - k_{AB} M_y^A(t) + k_{BA} M_y^B(t)$$

$$\frac{dM_z^A(t)}{dt} = -\omega_1 M_y^A(t) - R_1^A\left(M_z^A(t) - M_{th}^A\right) - k_{AB} M_z^A(t) + k_{BA} M_z^B(t) \tag{3.6}$$

$$\frac{dM_x^B(t)}{dt} = -\omega_B M_y^B(t) - R_2^B M_x^B(t) + k_{AB} M_x^A(t) - k_{BA} M_x^B(t)$$

$$\frac{dM_y^B(t)}{dt} = \omega_B M_x^B(t) + \omega_1 M_z^B(t) - R_2^B M_y^B(t) + k_{AB} M_y^A(t) - k_{BA} M_y^B(t)$$

$$\frac{dM_z^B(t)}{dt} = -\omega_1 M_y^B(t) - R_1^B\left(M_z^B(t) - M_{th}^B\right) + k_{AB} M_z^A(t) - k_{BA} M_z^B(t)$$

3.5 Solutions to the Bloch-McConnell Equations

The Bloch-McConnell (BM) equations have been solved numerically multiple ways (150; 151; 152; 153), but a simple and fast method involves a single exponential matrix evaluation (154) of the form:

$$\frac{d\mathbf{M}}{dt} = \mathbf{A} \cdot \mathbf{M} \tag{3.7}$$

Define matrices $\mathbf{M}$ and $\mathbf{A}$ as:

$$\mathbf{M} = \begin{bmatrix} M_x^A(t) & M_x^B(t) & M_y^A(t) & M_y^B(t) & M_z^A(t) & M_z^B(t) & 1 \end{bmatrix}^T \tag{3.8}$$

$$\mathbf{A} = \begin{bmatrix} -R_2^A - k_{AB} & k_{BA} & -\omega_A & 0 & 0 & 0 & 0 \\ k_{AB} & -R_2^B - k_{BA} & 0 & -\omega_B & 0 & 0 & 0 \\ \omega_A & 0 & -R_2^A - k_{AB} & k_{BA} & \omega_1 & 0 & 0 \\ 0 & \omega_B & k_{AB} & -R_2^B - k_{BA} & 0 & \omega_1 & 0 \\ 0 & 0 & -\omega_1 & 0 & -R_1^A - k_{AB} & k_{BA} & R_1^A M_{th}^A \\ 0 & 0 & 0 & -\omega_1 & k_{AB} & -R_1^B - k_{BA} & R_1^B M_{th}^B \\ 0 & 0 & 0 & 0 & 0 & 0 & 0 \end{bmatrix} \tag{3.9}$$

The solution of Eq. 3.7 is simply:

$$\mathbf{M}(t) = e^{\mathbf{A}t}\mathbf{M}(0) \tag{3.10}$$

This operation is easily evaluated in MATLAB. By normalizing by $\mathbf{M}(0)$, Eq. 3.10 can be rewritten as a function of the B_1 frequency, ω_1. The resulting expression (Eq. 3.11) is the mathematical representation of a Z-spectrum as it models the Z-component (subscript) of the magnetization of Pool A (superscript).

$$Z(t_{sat},\ \omega_1) = \left[\frac{\mathbf{M}(t_{sat},\ \omega_1)}{\mathbf{M}(0)}\right]_z^A = \left[e^{\mathbf{A}(\omega_1)t}\right]_z^A \tag{3.11}$$

This solution will be known as the BM solution. Its computational processing speed is several orders of magnitude faster than alternative numerical methods such as the Runge-Kutta-Fehlberg algorithm while producing comparable results (154). It is also easily adapted to accommodate systems exceed two spin pools and is the chosen method for the contents of Chapter 6.

The BM solution is a numerical solution suitable for both ^{1}H CEST and hyperCEST. In the case of hyperCEST, where the initial magnetization is much larger than the stationary state, the Bloch-McConnell equations can be approximated to yield the Full HyperCEST (FHC) solution (120).

$$Z(t_{sat},\ \omega_1) = e^{-\lambda_{depol}(\omega_1)t_{sat}} \tag{3.12}$$

Where $\lambda_{depol}(\omega_1)$ represents the depolarization rate:

$$\lambda_{depol}(\omega_1) = -\lambda_{direct}(\omega_1) - \lambda_{CEST}^{AB}(\omega_1) \tag{3.13}$$

which results from spin relaxation ($\lambda_{direct}(\omega_1)$) and chemical exchange ($\lambda_{CEST}^{AB}(\omega_1)$), defined as:

$$\begin{aligned} -\lambda_{direct}(\omega_1) &= R_1^A cos^2\theta + R_2^A sin^2\theta \\ -\lambda_{CEST}^{AB}(\omega_1) &= \frac{S_1 + S_2}{S_3 + S_4 + S_5 + S_6 + S_7 + S_8} \end{aligned} \tag{3.14}$$

In the above expression, the S functions are defined as:

$$S_1 = \omega_1^2 \frac{k_{AB} \cdot k_{BA}}{k_{AB} + k_{BA}} \cdot (\delta\omega_B - \delta\omega_A)^2$$

$$S_2 = \frac{R_2^B}{k_{AB}+k_{BA}} \cdot \omega_1^2 k_{AB} \left(\omega_A^2 + (k_{AB}+k_{BA})^2 + k_{AB}R_2^B + \omega_1^2\right)$$

$$S_3 = \left(\omega_A \left(k_{BA} + R_2^B\right) + \omega_B k_{AB}\right)^2$$

$$S_4 = \left(k_{AB} + k_{BA} + R_2^B\right)^2 \omega_1^2 \tag{3.15}$$

$$S_5 = \left(\omega_A\omega_B - k_{AB}R_2^B\right)^2$$

$$S_6 = \omega_B^2\omega_1^2$$

$$S_7 = k_{AB}R_2^B\omega_1^2$$

$$S_8 = \frac{k_{AB}+k_{BA}+R_2^B}{k_{AB}+k_{BA}} \left(\omega_A^2\omega_1^2 + \omega_1^4\right)$$

The FHC solution is limited to a 2-pool system and assumes that the longitudinal relaxation of both Pool A and Pool B are similar such that $T_1^A = T_1^B = T_1$. However, this is not always the case because T_1 for ^{129}Xe in water is on the order of 100 s, and molecular cages span a range of T_1 values such as 4 s for CryA (112) or several hundreds of seconds for gas-phase microbubbles (111). In these cases, an effective longitudinal relaxation rate $R_{1,eff}$ can be used in Eq. 3.14 that takes into account the weighted contributions of each pool.

$$R_{1,eff} = f_A R_1^A + f_B R_1^B \tag{3.16}$$

The FHC solution is a good approximation that can accurately simulate a Z-spectrum for hyperCEST experiments. It has been verified to be in agreement with numerical methods, and further reduces the computational time below that of the BM solution by 2 orders of magnitude (112; 120).

3.6 Quantitative HyperCEST

The BM solution and the FHC solution have utility for simulating Z-spectra and designing optimal experimental parameters for cw hyperCEST experiments (122; 147). They can also be used for analytical purposes by fitting experimental Z-spectra and extracting magnetic and kinetic parameters corresponding to each spin pool. This is the analysis known as quantitative hyperCEST, or qHyperCEST (112). qHyper-

CEST is a robust fitting method that can accurately quantify parameters such as δ_A, δ_B, k_{BA}, f_B, T_1^A, and T_2^A from simulated data (tolerating 10% noise) as well as experimental data (112).

The FHC solution also gives insight on the limitation of qHyperCEST. When $k_{BA} >> R_2^B$, which is the case for realistic hyperCEST agents like CryA, the depolarization rate (Eq. 3.13) simplifies to:

$$\lambda_{depol}\left(B_1,\ \omega_1\right) = f_B k_{BA} \frac{\left(\gamma B_1\right)^2}{\left(\gamma B_1\right)^2 + k_{BA}^2 + \left(\omega_1 - \omega_B\right)^2} \tag{3.17}$$

For on-resonance saturation of Pool B ($\omega_1 = \omega_B$), Eq. 3.17further simplifies to:

$$\lambda_{depol}\left(B_1\right) = f_B k_{BA} \frac{\left(\gamma B_1\right)^2}{\left(\gamma B_1\right)^2 + k_{BA}^2} \tag{3.18}$$

From here, two regimes can be defined. If $\gamma B_1 >> k_{BA}$, this can be considered as strong saturation, and $\lambda_{depol,max} = f_B k_{BA}$. Conversely, if $\gamma B_1 << k_{BA}$, this is the weak saturation regime, and $\lambda_{depol,max} = f_B \cdot \left(\gamma B_1\right)^2 / k_{BA}$. In the strong saturation regime, qHyperCEST was not able to separate f_B from k_{BA} because their product determined $\lambda_{depol,max}$. This may be an issue for presaturation field strengths that exceed 20 μT. In the weak saturation regime, qHyperCEST is a dependable fitting routine. Both the BM solution and the FHC solution are usable functional forms; the former can handle systems of multiple pools, while the latter cuts down on computational time (112).

Armed with the theoretical construct of hyperCEST, potential carrier molecules can be evaluated on their ability to provide efficient contrast at low concentrations. In the following Chapters, I will discuss my work to determine if US contrast agents are good hyperCEST agents and if hyperCEST enables their detection at clinically relevant US concentrations.

CHAPTER 4: CHARACTERIZATION OF GAS MICROBUBBLES AS HYPERCEST AGENT FOR DUAL MODALITY MR/US IMAGING

This section presents results that have been previously published in the journal *ChemPhysChem*[1].

4.1 Introduction

Gaseous microbubbles (MB) consist of a heavy-gas core surrounded by a lipid shell. They are extremely echogenic and provide enhanced US image contrast in clinical applications (63; 64; 65; 66). MB can also be functionalized to enhance their molecular specificity (155; 156), and can be guided or locally ruptured on command by US waves to deliver a payload of drugs (157; 158; 159; 160; 161) or gases, such as oxygen (60; 69; 162; 163).

MB have also been proposed as a contrast agent for MRI (61; 164). However, the susceptibility difference at the gas-liquid interface does not provide significant spin dephasing when compared to other MRI relaxation agents. In order to produce appreciable MRI contrast with raw MB, doses in excess of what is typically used for US are required (164). Alternatively, in order to enhance relaxivity, MB can be combined with iron oxides (61). This, however, is in contention with the growing concern over the toxicity of exogenous paramagnetic nanoparticles (57; 58; 165). While MB show great potential to be a dual modality contrast agent for US and MRI, progress must be made to improve MRI sensitivity to raw MB at concentrations comparable to those used for clinical US imaging (10 μL/kg at a concentration of 10^{10} MB/mL), which corresponds to an in-blood MB concentration on the order of 10s of fM.

Here, we assess whether lipid-shelled perfluorocarbon (PFC) MB at the clinically relevant blood concentration used for US studies (10s of fM), can produce an observable hyperCEST effect. This is accomplished by a theoretical and an experimental characterization of the exchange dynamics of samples with varying MB size distributions and concentrations using qHyperCEST (112; 120).

[1]C. T. McHugh, P. G. Durham, M. Kelley, P. A. Dayton, R. T. Branca. Magnetic Resonance Detection of Gas Microbubbles via HyperCEST: A Path Toward Dual Modality Contrast Agent. ChemPhysChem 2021, 22, 1219. https://doi.org/10.1002/cphc.202100183

4.2 Quantitative HyperCEST Simulations

Figure 4.1 shows the expected signal loss due to the hyperCEST effect at various B_1 strengths, using simulations based on the FHC Solution (112; 120). Monodisperse MB samples are defined by their average diameter and concentration (in terms of count or gas-volume per unit of solvent volume). The expected k_{BA} was estimated from the diffusion coefficient of ^{129}Xe between the two compartments (D = 19.5e-10 m^2 s^{-1}) (166), assuming a negligible contribution from diffusion through the monolayer lipid shell, whose thickness is on the order of nm.

$$k_{BA} = \frac{D}{4\pi r^2} \tag{4.1}$$

The expected f_B was estimated by using the Ideal Gas Law and Henry's Law (K_H = 4400e-8 mol m^{-3} Pa^{-1}) (167) at a given gas-volume concentration G in units of liters of gas per liter solution.

$$f_B = \frac{G}{RTK_H} \tag{4.2}$$

These simulations show that the signal reduction increases with B_1 as well as with gas-volume concentration, as expected. The simulations also show that MB size must be optimized to maximize signal reduction. If the MB are too small, k_{BA} is too fast for the spins to be appreciably saturated by B_1. On the other hand, large MB with slow k_{BA} are not ideal either since depolarized spins still must be exchanged into Pool A at experimental timescales. Further, the expected k_{BA} for ^{129}Xe with micron-sized MB is ideal for competing with relaxation ($k_{BA} >> 1/T_1^{A,B}$), where T_1^A in phosphate buffer saline (PBS) is 160 s and T_1^B is on the order of an hour (168).

4.3 Materials and Methods

MB preparation

PFC MB were prepared in-house as described previously (169). Briefly, 1,2-distearoyl-sn-glycero-3-phosphocholine (DSPC) and 1,2-distearoyl-sn-glycero-3- phosphoethanolamine-N-methoxy (polyethylene-glycol)-2000 (DSPE-PEG2000) (Avanti Polar Lipids, Alabaster, AL, USA) were dissolved in 5% glycerol, 15% propylene glycol (both from Fisher Chemical, Waltham, MA, USA) in PBS (v/v) at a 1:9 ratio, to

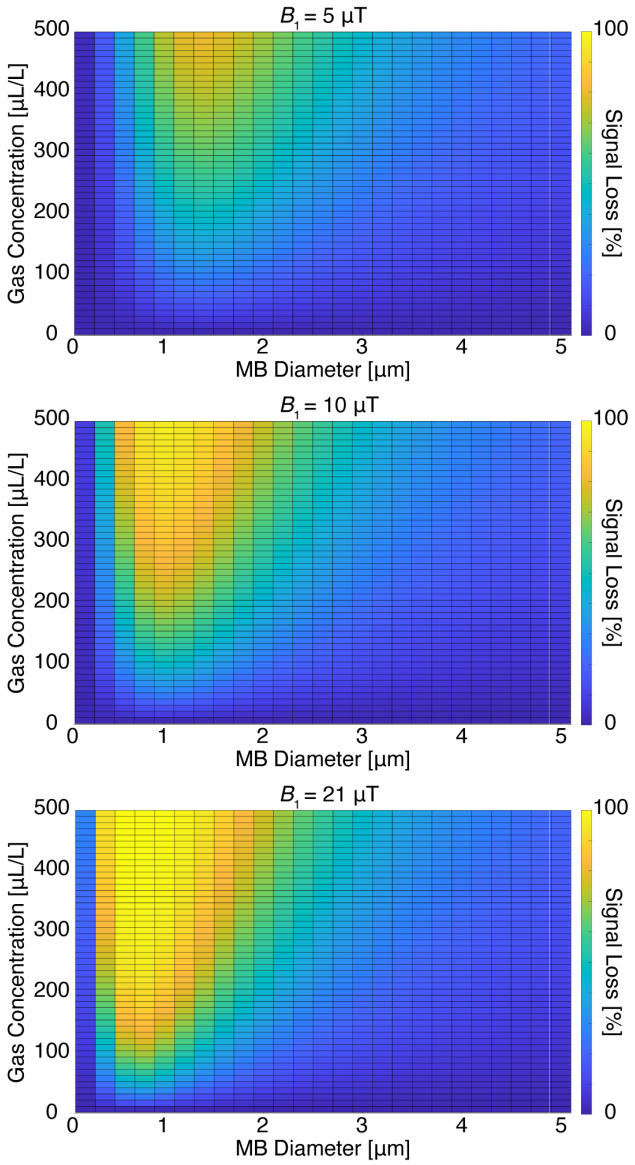

Figure 4.1: Simulated solvent signal loss for different MB diameters and saturation field strengths. MB samples are defined by the gas-volume concentration (μL/L) and average diameter (μm), which determine f_B , k_{BA}, and the size of signal loss. Signal loss generally increases with B_1 and gas-volume concentration, while is maximized for MB with a diameter between 1-2 μm. For context, theoretical exchange rates for 1, 2, and 3 μm MB are 600 Hz, 160 Hz, and 70 Hz, respectively.

a total lipid concentration of 1 mg/mL. Dissolved gas was removed from the prepared solution under vacuum. Vials were then backfilled with decafluorobutane (Fluoro Med, Round Rock, TX, USA). MB were generated via mechanical agitation (VialMix, Bristol-Myers- Squibb, New York, NY, USA). MB size and concentration were determined via single particle optical sizing (Accusizer 780AD, Particle Sizing Systems, Port Richey, FL, USA). In addition, commercially available MB were purchased from Advanced

Microbubbles Inc (Newark, CA, USA). MB used in these experiments are comparable to already FDA approved contrast agents (170) that would need no modification to be evaluated in humans.

Samples were prepared with three MB size distributions: small (0.9 ± 0.4 μm), medium (2 ± 1 μm), and large (3.2 ± 0.7 μm) diameters (Figure 4.2). The standard MB dose for humans is 10 μL/kg at 10^{10} MB per mL, and can be 10x greater for rodents, depending on the application (170). This results in an *in vivo* human and rodent blood-concentrations of approximately 10 and 100 fM, respectively. In order to reflect these conditions, each sample was diluted to 10s-100s fM. MB distribution plots are provided in Figure 4.2.

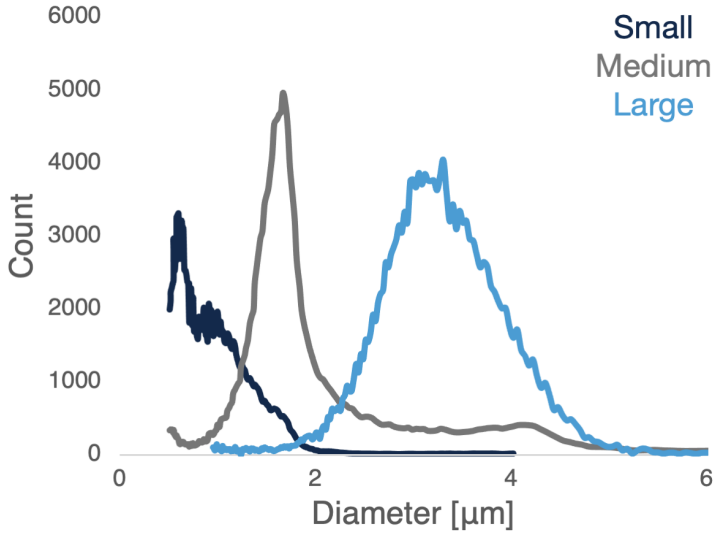

Figure 4.2: MB size distributions. Size distributions for small, medium, and large MB are shown. MB samples were prepared in-house for small (0.9 ± 0.4 μm) and medium (2 ± 1 μm) MB. MB size and concentration were determined via single particle optical sizing (Accusizer 780AD, Particle Sizing Systems, Port Richey, FL, USA). Large (3.2 ± 0.7 μm) MB were purchased from Advanced Microbubbles Inc (Newark, CA, USA).

Production and delivery of HP ^{129}Xe

Xe gas (26.4% ^{129}Xe) was polarized to approximately 20% by using a Polarean 9800 Xe polarizer (Polarean, Durham, North Carolina, USA). Absolute ^{129}Xe polarization values were measured by using the Polarean 2881 polarization measurement station. For the experiments, HP ^{129}Xe gas along with N_2 buffer gas was dispensed into a 275 mL Tedlar bag (Jensen Inert Products, Coral Springs, Florida, USA) in a 75/25 Xe/N_2 volume ratio. The gas was delivered by using a HP gas compatible ventilator (171) (built

in-house) controlled via LabVIEW (National Instruments, Austin, Texas, USA), which allowed for precise control of gas volume and timing used for the HP ^{129}Xe bubbling.

NMR Spectroscopy Experiments

All spectroscopic studies were performed on a Varian Inova 500 MHz high resolution NMR spectrometer (Varian NMR Systems, Palo Alto, California, USA) using a ^{1}H-^{19}F/^{15}N-^{31}P PFG switchable broadband probe. In order to replicate *in vivo* conditions, all NMR experiments were performed at a temperature of 37 °C, pre-calibrated using the chemical shift separation between methyl and hydroxyl protons in a 100% methanol sample. Optimal shimming conditions were found by manual shimming of the ^{1}H spectrum of a pure sample of PBS as the inclusion of microbubbles in the sample induced magnetic field inhomogeneities that hindered optimal shimming (172).

Each MB sample was placed in a 5 mm (outer diameter) NMR tube and equilibrated to the set temperature before the beginning of each experiment. The HP-compatible ventilator bubbled HP ^{129}Xe through PEEK tubing (0.5 mm inner diameter) for 2 s directly into the sample. The length of the bubbling cycle was found to be sufficient for providing a reproducible starting magnetization. After HP ^{129}Xe bubbling, a 1 s delay was used before the application of a continuous-wave presaturation pulse (B_1) applied for a saturation time (t_{sat}) of 2 s. A ^{129}Xe spectrum was then acquired using a center frequency of 138.27 MHz (on-resonance with the dissolved-phase ^{129}Xe frequency, here labeled as 0 ppm), a spectral width of 60015 Hz, 8192 data points, 2 averages, and a pre-calibrated flip angle of 90°. Such large excitation spectral width enabled us to use the same spectra used for the acquisition of Z-spectra, for T_1 correction of the HP gas magnetization, and for the detection of possible bubbles trapped in the sensitive region of the coil. The cycle of delivery of fresh HP ^{129}Xe followed by presaturation and signal acquisition was repeated as the frequency offset of the saturation pulse B_1 was varied across the spectral width. Care was taken to increase the density of measurements around offset frequencies corresponding to dissolved-phase ^{129}Xe signal and the gas-phase ^{129}Xe signal. Initial points upfield from -300 ppm were removed from the analysis due to variable magnetization at the start of each experiment to allow the sample to approach a steady state in dissolved ^{129}Xe concentration and for ^{129}Xe to establish itself in the core of the MB. Also, spectra that showed a distinct peak at -194.6 ppm were also removed from the analysis (Figure 4.3). These spectra reflected the presence of a large gas bubble trapped in the sensitive region of the spectrometer during signal acquisition, inducing large B_0 inhomogeneities.

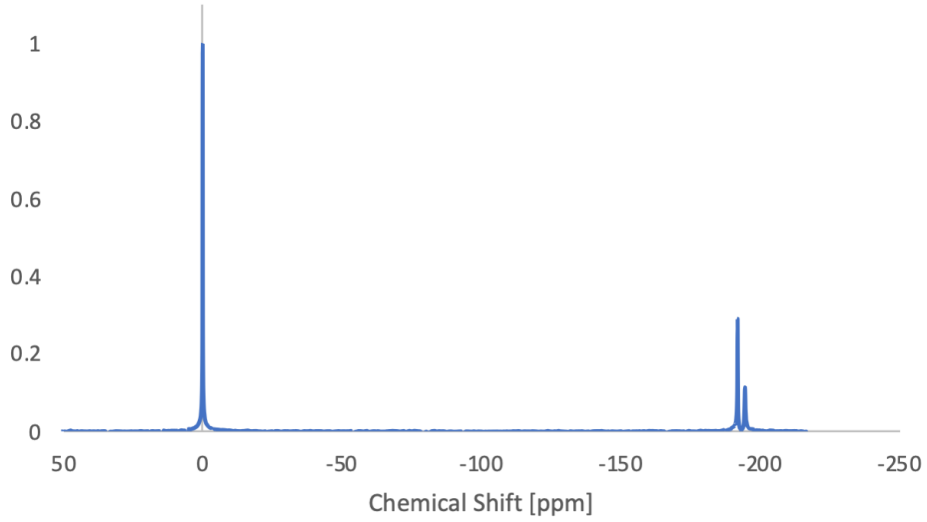

Figure 4.3: Spectrum of a MB suspension with a large gas bubble trapped in the sensitive region. After the bubbling procedure, a distinct gas-phase ^{129}Xe peak at -194.6 ppm was observed whenever a mm-sized bubble was stuck in the sensitive region of the spectrometer. It is important to note that, even if this signal comes from a much large spherical enclosure, according to magnetostatics, the susceptibility-induced frequency shift felt by the spins in the large bubbles should be the same as the one felt inside the much smaller MB.

Analysis

All data processing and fitting were done by using MATLAB R2019b (The Mathworks, Inc., Natick, Massachusetts, US). The signal intensity of the dissolved-phase ^{129}Xe peak (placed at 0 ppm) was recorded for each B_1 offset frequency. A T_1-correction was applied to these values due to the loss of polarization of the HP ^{129}Xe gas as it sat in the fringe field of the spectrometer. The Z-spectrum was formed by plotting the normalized T_1-corrected solvent ^{129}Xe signal intensity as a function of the B_1 offset frequency.

The Z-spectra were fit according to the FHC solution, as previously published (110; 112; 120). Using the built-in MATLAB function MultiStart (50 iterations) in conjunction with lsqcurvefit, the following kinetic parameters were determined: f_B and k_{BA}. Initial values and upper and lower bounds were required as inputs. To minimize the chance of ending up in a local minimum, a common issue with multiparametric fitting procedures, T_1^A was measured separately.

4.4 Results

The predicted hyperCEST effect for gas MB was verified experimentally *in vitro*. Samples of DSPC:DSPE-PEG2000 coated MB, filled with decafluorobutane (DFB) at varying MB sizes were diluted to *in vivo* concentrations used for pre-clinical and clinical US studies. They were then placed in a high-resolution NMR spectrometer equipped with a single axis gradient, and equilibrated to a set temperature of 37 °C. Fresh HP ^{129}Xe was bubbled directly into the sample at 1 psig (Figure 4.4A). The bubbling duration was set to 2 s, which allowed for an adequate amount of ^{129}Xe to dissolve into solution, while rationing a single batch of polarized gas to across the acquisition of an entire Z-spectrum. After the bubbling procedure, a continuous-wave presaturation pulse was applied for 2 s, and the resulting ^{129}Xe signal was acquired. The experiment was repeated as the frequency of B_1 was varied across a range of more than 250 ppm. The normalized dissolved-phase signal (referenced to be 0 ppm) was then plotted as function of the B_1 frequency to construct a Z-spectrum.

It is of note that, in order for ^{129}Xe to become fully incorporated into solution as well as into the gas core of MB (173; 174; 175), ^{129}Xe was bubbled into the solution before the beginning of the NMR experiment. This resulted in a surplus of the dissolved-phase magnetization. Once the NMR acquisition started, a steady state magnetization was reached after the acquisition of the first 3 data points, which were consistently excluded from the analysis during the post processing procedure (Figure 4.5). The steady state magnetization reached after the acquisition of the first 3 data points reflected the amount of HP ^{129}Xe gas that was continuously replenished by the 2 s bubbling procedure. A 2-second bubbling duration was chosen to enable the acquisition of an entire z-spectrum using a single batch of HP ^{129}Xe gas, and because of the limited lifetime of MB under bubbling conditions.

Figure 4.4 shows ^{129}Xe spectra acquired on a sample with and without an on-resonance (-194.6 ppm with respect to the dissolved-phase signal) RF saturation pulse of 5 μT. First, it is interesting to note the lack of a gas-phase peak at -194.6 ppm in the MB spectrum acquired with off-resonance saturation. Even at the highest MB concentrations used in this study (just 380 fM), the ^{129}Xe signal originating from the gas-phase core of MB cannot be observed directly. Yet, as shown in Figure 4.4B, significant dissolved-phase signal loss is observed in the MB sample when an RF saturation is applied at -194.6 ppm. Also, no dissolved-phase signal loss is observed for a saturation frequency of -192 ppm, which corresponds to residual gas-phase ^{129}Xe inside of the PEEK tube immersed in the sample. On the other end, no signal

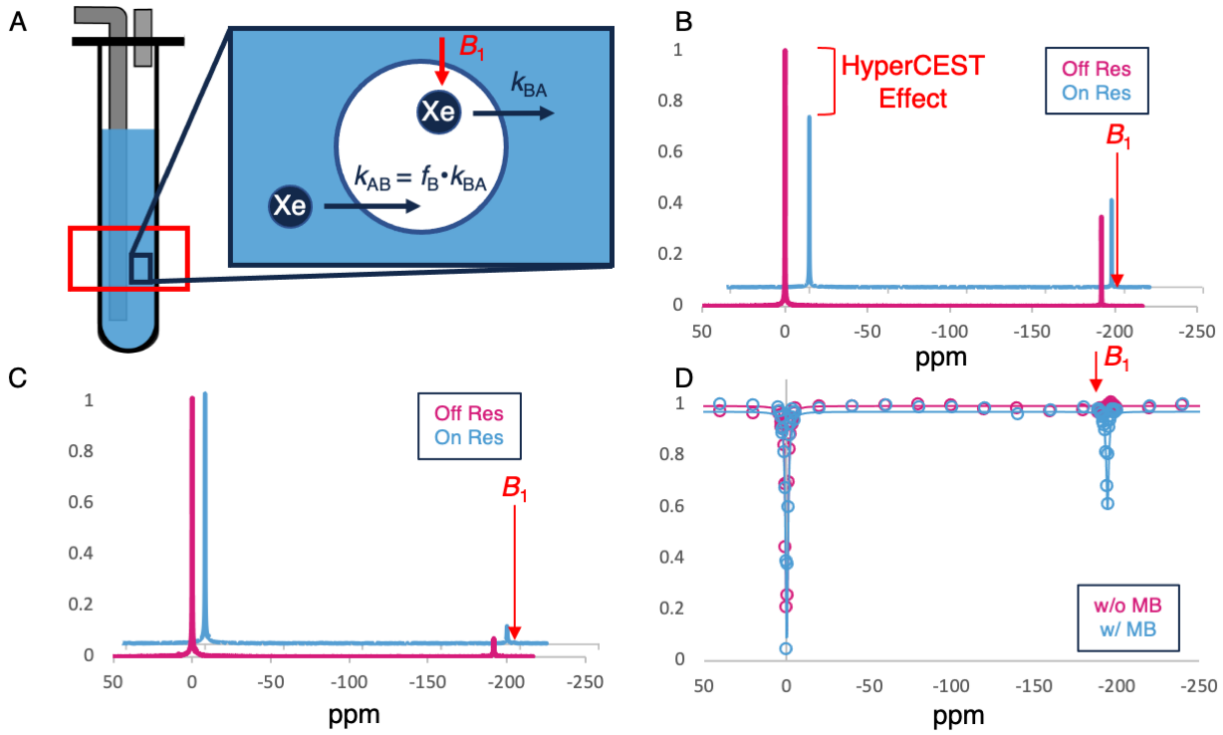

Figure 4.4: Effect of on-resonance saturation on ^{129}Xe NMR spectrum. (A) Sketch of the experimental NMR setup (not on scale). A suspension of MB was placed in an NMR tube. Fresh HP ^{129}Xe gas was bubbled directly into the suspension through a long narrow PEEK tube, connected to an HP-compatible ventilator on one end, and immersed in the NMR tube on the other end. ^{129}Xe exchanges into and out of the MB according to k_{AB} and k_{BA}, respectively. (B) ^{129}Xe NMR spectra from a suspension of MB, with on-resonance (-194.6 ppm) and off-resonance RF saturation. Peaks at 0 ppm and -192 ppm correspond to ^{129}Xe dissolved in the solvent, and residual ^{129}Xe gas inside of the PEEK tubing, respectively. At the low MB concentrations used here, the gas-phase signal originating from ^{129}Xe inside of the MB core, and located 2.6 ppm upfield from the gas-phase peak inside of the PEEK tubing, cannot be observed directly. But, when B_1 is on-resonance the MB, a significant attenuation of the dissolved-phase signal is observed. (C) NMR ^{129}Xe spectra of a solvent sample without MB, acquired with on- and off-resonance RF saturation. Peaks at 0 ppm and -192 ppm are still visible. However, no solvent signal reduction is observed after RF saturation at -194.6 ppm. (D) Z-spectrum showing a 40% signal loss for a saturation frequency of -194.6 ppm is observed only in presence of MB.

reduction is seen for the same saturation frequency in absence of MB (Figure 4.4C and 4.4D), confirming that the hyperCEST effect seen in the sample with MB is indeed due to saturation of gas-phase spins inside the MB core.

The 2.6 ppm frequency shift observed between the residual ^{129}Xe gas in the PEEK tube (observed directly at -192 ppm from the dissolved-phase signal) and the ^{129}Xe gas in the MB core (observed only indirectly in the z-spectrum at -194.6 ppm), is consistent with the susceptibility-induced frequency shift expected between gas enclosed into a sphere and a long vertical cylinder (Figure 4.6). In order to confirm

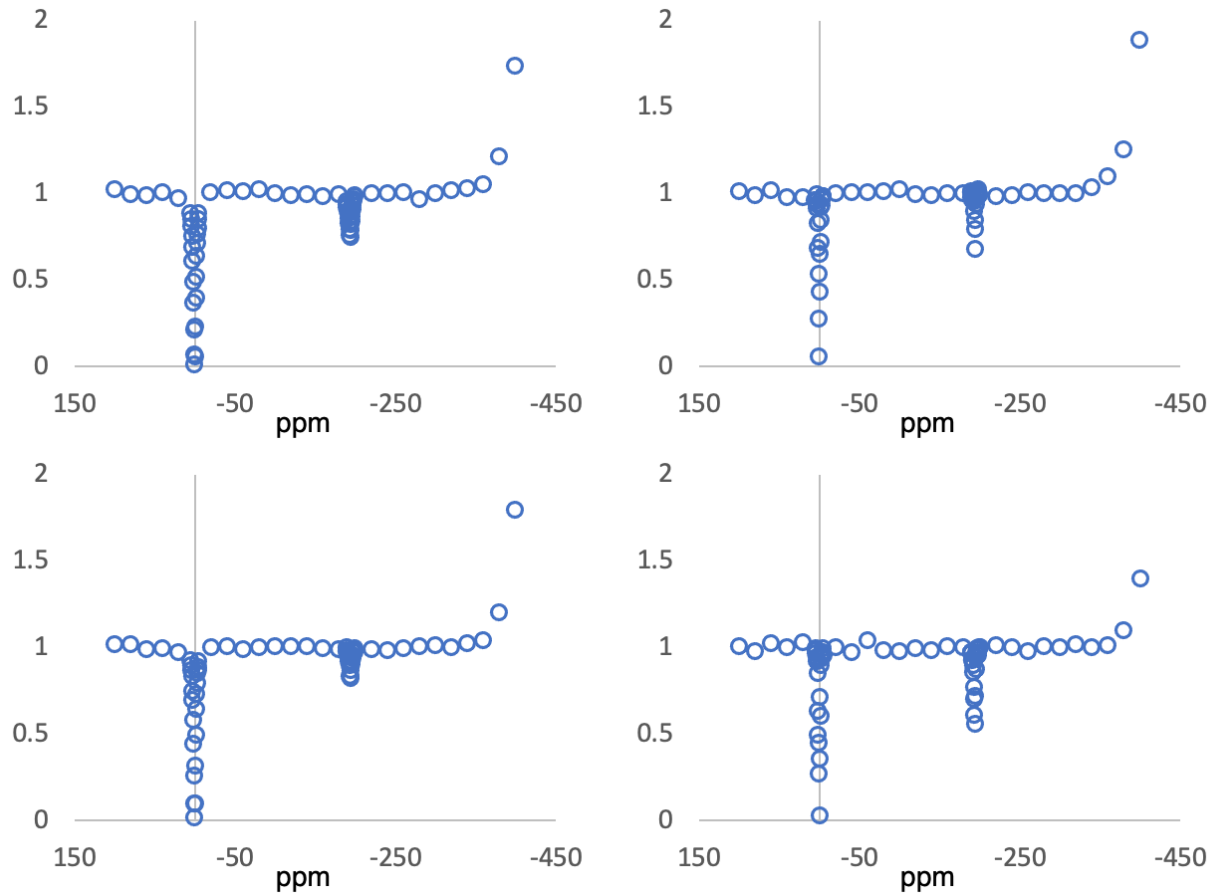

Figure 4.5: Examples of full Z-spectra including initial points. Data points for each Z-spectrum were collected sequentially from right to left as shown in these examples. A steady state magnetization was soon reached after the acquisition of the first three data points of each Z-spectrum, which were subsequently discarded from the analysis.

that the observed shift was purely due to a susceptibility-induced frequency shift, magnetic field maps were simulated using finite element analysis computations (COMSOL Multiphysics, Stockholm, Sweden). Maxwell's equations were solved for a gas-filled vertical cylinder (Figure 4.6A) and sphere (Figure 4.6B) submerged in water. The respective susceptibilities of the compartments were considered, and the sphere of Lorentz correction was applied to calculate the local magnetic flux density and the corresponding susceptibility-induced frequency shift (176). These simulations confirmed a +2.8 ppm susceptibility induced frequency shift for the gas inside the vertical cylinder compared to that in the sphere. Because these field perturbations are independent of the compartment size, the same susceptibility induced frequency shift is expected for small and large MB, including the mm-sized bubbles trapped in the sensitive region of the spectrometer.

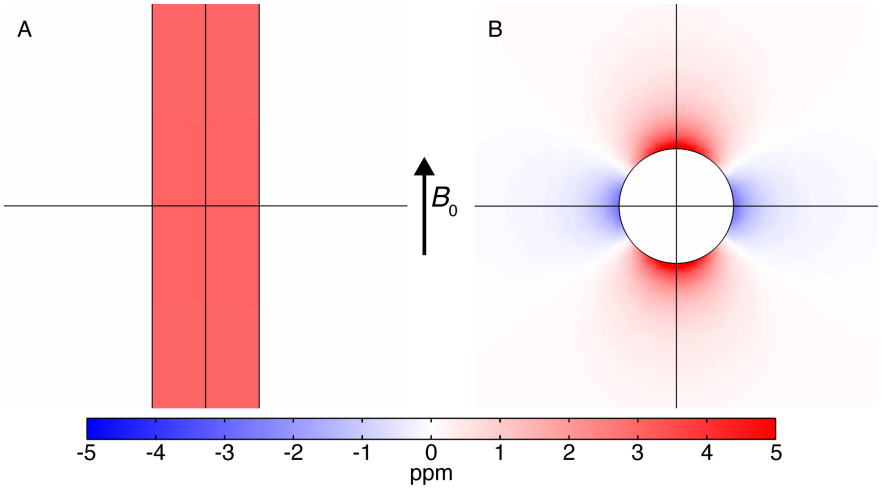

Figure 4.6: Expected susceptibility-induced frequency shift for a long vertical cylinder and for a sphere placed in a magnetic field. Simulations of the frequency shift expected for an infinite vertical cylinder (A) and a sphere (B) immersed in a more diamagnetic medium. In these simulations, the interior of each geometry is assumed to contain a 75/25 Xe/N_2 mixture (χ=-1.904e-8), while the exterior is assumed to contain water (χ=-9.035e-6). According to magnetostatic, the local magnetic flux density felt inside the long cylinder should be about 2.8 ppm greater than the one felt inside the spherical enclosure, regardless of their dimensions. As a result, two separate gas-phase peaks should be expected in the ^{129}Xe spectrum: one downfield corresponding to ^{129}Xe inside the long cylindrical PEEK tube, and one upfield corresponding to ^{129}Xe inside the spherical MB.

Incidentally, a large distinct peak, also located at -194.6 ppm, was observed whenever a large ^{129}Xe bubble was trapped in the sensitive region of the coil (Figure 4.3). As such, all spectra that showed an additional peak upfield from the gas phase peak were removed from the analysis.

Figure 4.7 shows three separate and consecutive Z-spectra zoomed near the gas-phase frequency. A strong hyperCEST effect is shown during the acquisition of the first Z-spectrum. However, for the following two Z-spectra acquisitions, the hyperCEST effect was significantly diminished. Similar behavior was observed for other samples. Such behavior is consistent with the expected decrease in MB concentration during the bubbling process. MB lifetime in solutions strongly depends on the type and concentration of dissolved gases as well as the presence of shear forces (173; 174; 175). Shear forces produced during the bubbling procedure could contribute to decrease MB lifetime. While the decrease in MB concentration after each Z-spectrum acquisition was easily observed as a reduction of the hyperCEST effect at the -194.6 ppm saturation frequency, this reduction could not be quantified using the single particle optical sizing because of the very low MB concentrations used in these NMR experiments. To compensate for any variability in MB concentration, new suspensions were prepared immediately before each experiment.

Nonetheless, since the amount of signal loss decreases with MB dissolution, this data demonstrates that the hyperCEST effect we observe is indeed contingent on the presence of MB.

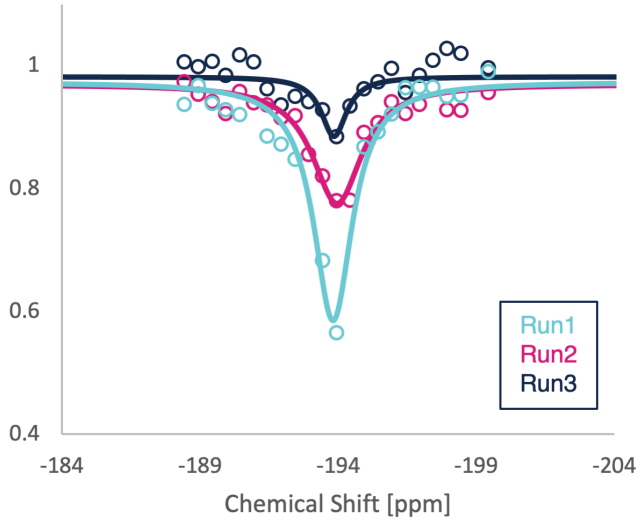

Figure 4.7: Loss of hyperCEST effect from MB over time due to the slow destruction of gas MB. MB Z-spectra shown near the gas phase frequency at -194 ppm from the solvent frequency. Initially, medium-sized MB show a strong hyperCEST effect (Run 1) which diminished with time during the acquisition of consecutive Z-spectra (Run 2 and Run 3). Each Z-spectrum was acquired in 13.5 min. This clearly demonstrates that MB produce hyperCEST contrast, and as MB concentration diminishes, so does the induced hyperCEST effect.

Figure 4.8 shows the various Z-spectra acquired from all samples near the gas-phase frequency. The average chemical shift of ^{129}Xe in MB was determined to be -194.2 ± 0.4 ppm from the dissolved-phase frequency. Figures 4.8A and 4.8B show the effect of B_1 on signal reduction for small and medium MB samples at constant concentration (340 fM for small MB, and 40 fM for medium MB). The trend confirms the theoretically predicted behavior shown in Figure 4.1: as B_1 increases, more signal is depleted from Pool A.

Next, small, medium, and large MB were tested at varying molarity to demonstrate the effect of increasing gas-volume concentration (directly related to f_B). Figures 4.8C, 4.8D, and 4.8E verify that increasing f_B improves hyperCEST efficiency by inducing more signal reduction. Finally, Figure 4.8F shows the effect of varying MB size at constant molarity. At a given molarity, the increase in MB size is expected to lead to an increase in the number of spins that participates in the exchange process. But, Figure 4.8F shows that overcompensating with MB size may have diminishing returns. This should not come

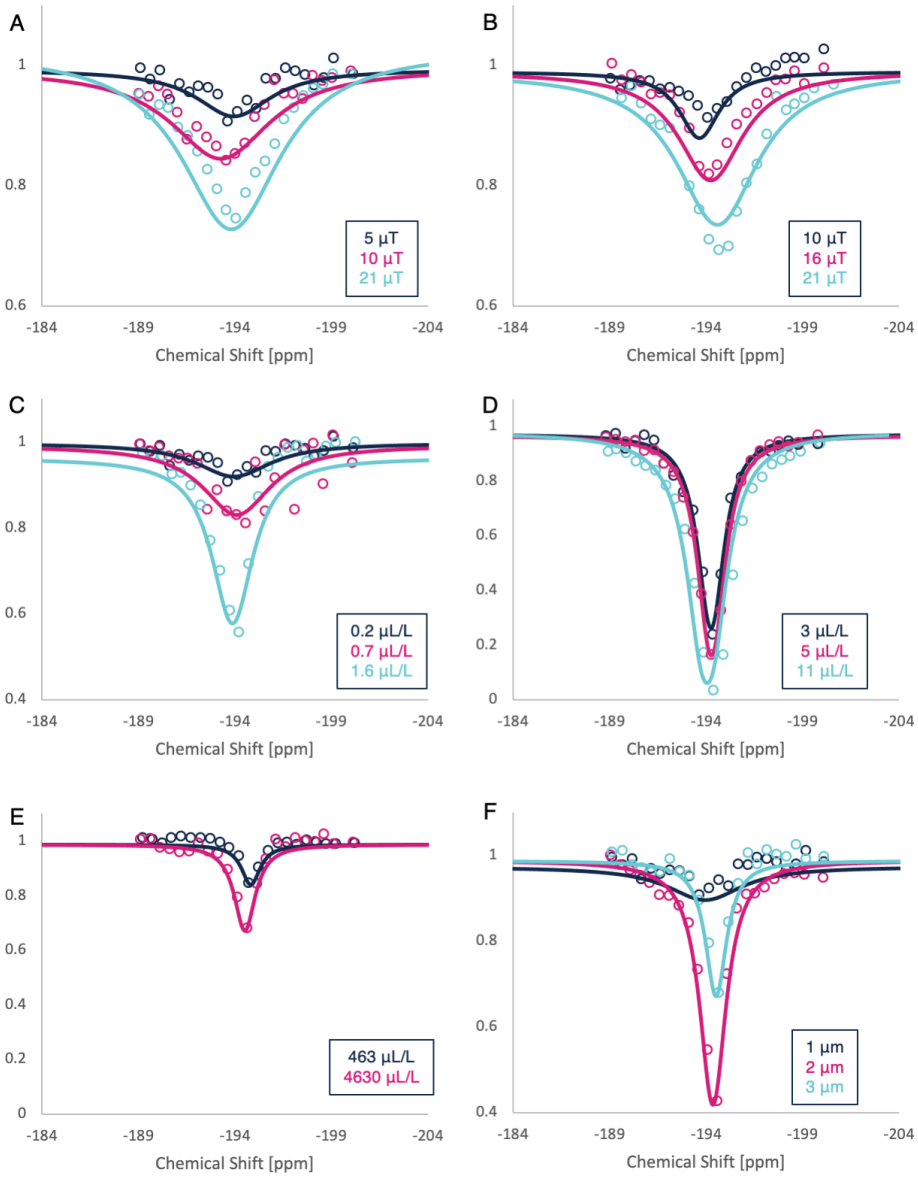

Figure 4.8: Experimental Z-spectra obtained from different MB samples. MB Z-spectra shown near the gas phase frequency. A narrow valley, characteristic of slow k_{BA} and narrow gas phase frequency distribution inside the MB, can be observed at around -194 ppm from the dissolved-phase ^{129}Xe signal. For these experiments, B_1 was varied while maintaining a constant number concentration for small (A, 340 fM) and medium (B, 40 fM) MB. Gas-volume concentration was varied at constant B1 (5 μT) for small (C), medium (D), and large (E) MB. MB diameter was varied at constant number concentration (F, 400 fM). The trends shown all follow theoretical predictions. Signal loss increases with B_1 as well as gas-volume concentration. HyperCEST efficiency increases until the diameter exceeds 2 μm, for which k_{BA} is then too slow to transfer a significant number of saturated spins to Pool A.

as a surprise because larger MB are expected to have a decreased gas turnover rate, as predicted by the theoretical model.

qHyperCEST was used to fit the Z-spectra and extract the dynamic parameters k_{BA} and f_B for ^{129}Xe in chemical exchange with MB. Table 4.1 reports the different MB concentrations and sizes used in this study, the corresponding hyperCEST effect, as well as the range of k_{BA} and f_B values obtained from the Z-spectra fitting procedure. Overall, k_{BA} was slow on the NMR timescale decreasing further as MB diameter increased. For small and medium MB samples, the f_B determined from the Z-spectra using qHyperCEST was greater than what was expected, but not for large MB. The discrepancy between the expected f_B value and the experimentally obtained f_B value is likely the result of an increase in MB diameter caused by the exposure of MB to the new gas environment. The MB were initially filled with DFB and were kept in vials in equilibrium with a headspace that was also filled with DFB. When put in the NMR tube, the samples were exposed to the Xe/N_2 gas mixture that was bubbled into the solution. As previously discussed, gas exchange and MB dissolution occur when MB are transferred between environments with different gas compositions (173; 174; 175; 177). Specifically, simulations based on *in vivo* gas partial pressures for rats showed an increase in MB diameter by a factor of 3, mostly due to the rapid inflow of N_2 to replace the original contents of the MB. Xe and N_2 both have very similar diffusion coefficients (166), and this type of gas turnover may explain the volumetric increase proportional to the measured increase in f_B from the ideal case. MB dissolution is driven by surface tension and dissolved-gas concentration. Differences in surface tension may explain why small and medium MB expanded while large MB shrunk. Additionally, MB growth could be similar to the ripening observed from nanoemulsions (116). This could be an alternative explanation for the decrease in hyperCEST contrast after repeated measurements shown in Figure 4.7. The medium-sized MB may have expanded, resulting in inefficient kinetics. Because MB have a size distribution, their expansion or contraction during the bubbling procedure would be difficult to simulate.

4.5 Discussion

HyperCEST is a very powerful NMR technique that can be used to indirectly detect dilute ^{129}Xe hosts that actively exchange ^{129}Xe gas with the solvent. Compared to ^{1}H CEST, hyperCEST presents an increase in solute sensitivity by orders of magnitude due to the smaller solvent HP ^{129}Xe detection pool

MB Sample	Mean Diameter [μm]	Concentration [fM]	Gas Volume Concentration [μL/L]	Expected f_B [10^{-6}]	B_1 [μT]	Fit f_B [10^{-6}]	Fit k_{BA} [s^{-1}]	Gas Turnover Rate per Host [10^6 s^{-1}]	Signal loss [%]
Small	0.9 ± 0.4	336	0.2	2	5	470	1560	7271	10.5
					10	320	1946	6201	17.5
					21	240	1267	3048	26.1
		738	0.67	6	5	930	1383	5809	19.4
		2240	1.6	14	5	1800	676	1818	45.2
Medium	2 ± 1	37.5	1.7	15	10	200	361	6442	9.3
					16	200	583	11081	19.1
					21	290	600	15319	26.5
		85	3	24	5	3500	340	46800	73.8
		170	5	48	5	4900	300	28200	83.9
		340	11	96	5	7400	420	30200	93.9
Large	3.2 ± 0.7	39	460	4080	5	2000	41	7028	16.1
		390	4630	40800	5	1400	163	1956	32.9

Table 4.1: Characteristics of MB samples used for the experiments and FHC fit results for the MB samples. Small, medium, and large MB samples were made with distributions centered around 0.9, 2, and 3.2 μm diameters, respectively. The samples were diluted to concentrations comparable to the *in vivo* blood concentration of MB used in rodents (100 fM) and humans (10 fM) in clinical US studies. All Z-spectra were collected using a 2 s saturation pulse at the listed B_1. qHyperCEST using the FHC solution were used to determine k_{BA} and f_B, which were used to calculate the gas turnover rate per host, defined as the product of k_{BA} and the number of ^{129}Xe atoms per host as determined by f_B. The expected f_B was calculated by using the ideal gas law and Henry's law. The difference between the expected f_B and f_B determined by qHyperCEST is indicative of a change in MB size.

(Pool A), which is capable of displaying sufficient magnetization for signal detection, and efficient f_B for CEST contrast generation. After its first *in vitro* demonstration in 2006, the first *in vivo* hyperCEST demonstration in rats came more than 10 years later, using CB[6] at a relatively high concentration of 10 mM (123). For human translation, larger hyperCEST agents that are capable of containing and interacting with thousands of ^{129}Xe atoms at once are needed because their working concentrations can be decreased to levels that are much lower than the ^{129}Xe carriers that maintain a 1:1 stoichiometry.

Here, we demonstrated that gas MB produce a substantial hyperCEST effect at concentrations as low as 10s of fM, surpassing the current limit for NMR/MRI contrast agent detection. This concentration corresponds to the FDA approved MB dose used for contrast US studies, also on the order of 10s of fM.

The large hyperCEST effect observed in this study is similar to the one previously observed with liquid-core PFC nanoemulsions at fM concentrations (116). In fact, these earlier studies shed light on the importance of exchange kinetics for optimizing the hyperCEST effect. Specifically, chemical exchange can

cause broadening of peaks in NMR spectra (115; 107). Similarly, the valleys in a Z-spectrum can broaden when exchange rates increase. This may cause the valleys to coalesce, masking the effect of selectively saturating Pool B by the direct saturation of Pool A. As shown by Stevens et al., by increasing the size of the nanoemulsions (and consequently decreasing the carrier concentration to maintain a constant Pool B volume), k_{BA} is decreased and the valley corresponding to Pool B was then resolved. But, k_{BA} remained relatively fast, and still encouraged the use of high saturation powers. Further increasing carrier size may be beneficial for the liquid-core PFC nanoemulsions, but it eventually would yield diminishing returns. The same behavior is expected for gas MB. However, because of the much higher diffusion rate of ^{129}Xe in the gas phase, larger size MB can still be more efficient compared to nanosized emulsions, in which gas diffusivity is significantly reduced. Similar to nanoemulsions, the simulations in Figure 4.1 show that there is an optimal size for MB. While k_{BA} must be slow enough to allow time for the spins of Pool B to be significantly depolarized, substantial exchange still must occur to transfer observable signal loss to Pool A. The experimental data shown in Figure 4.8F corroborate the theory and clearly show a better efficiency of medium and small size MB, compared to largest one.

In order to alleviate any concern of coalescing valleys while allowing for slow to intermediate k_{BA}, the chemical shift between Pool A and Pool B should be large. Another advantage of MB, when compared to nanoemulsions and other hyperCEST agents, is the much larger chemical shift difference between the solvent and the gas-phase peak inside the MB core, -194.2 ppm, which places MB as hyperCEST agents in the much favorable slow exchange regime.

It is also important to point out that in addition to their size, the shell chemistry and gas composition of gas MB represent additional degrees of freedom for optimization of hyperCEST efficiency. The shell of MB can be made out of lipids, lipopolymers, proteins, or polymers, all of which have different ^{129}Xe solubilities, while their core can contain different gases or gas mixtures, that can lead to a change in the resonance frequency and diffusion coefficient, all of which are expected to change ^{129}Xe exchange rate in and out of the MB.

Nanoscale GV also enclose ^{129}Xe in the gas phase, and they have shown hyperCEST at pM concentrations (110). Farhadi et al. also aimed to develop a dual US/MRI contrast agent, but with GV (146). While GV can contain thousands of gaseous ^{129}Xe atoms, a 2 μm MB can host millions. The larger volume of MB and the resulting lower k_{BA} lead to better gas turnover and a detection sensitivity down to fM concentrations (Table 4.1). In addition, while GVs are usually found in oblong, almost cylindrical shapes, whose

random orientation with respect to B_0 leads to a broad frequency distribution of the ^{129}Xe gas frequency enclosed in its core, MB have spherical shapes, which inherently leads to a very narrow frequency distribution of its gas core. The much narrower frequency distribution of the MB gas core leads to much narrower valleys than those observed by either Kunth et al. or Farhadi et al. for GVs, and to a more efficient saturation (110; 146). A similar hyperCEST effect was indeed observed not just at smaller molar concentrations than those reported for GV, but also for weaker (5 μT compared to 15 μT) and shorter (2 s compared of 10 s) RF saturation pulses. This results in an almost two orders of magnitude reduction in SAR, when compared to similar hyperCEST agents. Although Figures 4.8A and 4.8B suggest increasing B_1 to maximize signal reduction, 20% signal reduction is sufficient for imaging studies137, and is easily surpassed at 5 μT for medium-sized MB. This is especially relevant for *in vivo* translation of any hyperCEST agent, where the need of long saturation pulses may be prohibitive due to SAR limitations.

The lowest molar concentration used in this study was 37.5 fM. At this concentration a 9.3% signal loss was achieved. When dealing with larger hyperCEST agents that accommodate many ^{129}Xe atoms at a time, it is more appropriate to compare hyperCEST efficiency of different carriers while normalizing for the partial volume of the sample occupied by each carrier. For this reason, here we present MB concentrations in terms of μL of carrier volume per L of solution. The nanoemulsions used by Stevens et al. had droplet volume concentrations of approximately 230 μL/L. With a B_1 of 21 μT and a t_{sat} of 2 s, 26 pM of 310 nm nanoemulsions provided 80% signal loss (116). Figure 4.8D shows medium MB produced >80% signal loss at the much smaller partial volume of 5 μL/L and with only a 5 μT presaturation pulse with a duration of 2 s. Previous GV data could not be directly compared in the same manner because of the use of multiple different combinations of B_1 and t_{sat} (110). In this case, the gas turnover rate per host (Table 4.1) may be used to characterize carrier efficiency as it directly quantifies the number of ^{129}Xe atoms a carrier interacts with per second. Compared to GV, MB have higher gas turnover rates per host by up to 2 orders of magnitude.

The overarching goal of hyperCEST is molecular imaging, requiring functionalization of the cage molecule in order to target different disease sites. MB have been functionalized with binding ligands to increase their targeting specificity and they have been used for *in vivo* diagnostics and targeted delivery of therapeutic payloads, such as gases (60; 69; 162; 163) or drugs (157; 158; 159; 160; 161). Next steps should focus on MB functionalization through molecular targeting (155; 156; 178) for hyperCEST imaging, similar to how GV were previously used to image breast cancer cells *in vitro* (118). Because the spec-

trometer used in the current study was not equipped with imaging gradients, we could not perform *in vitro* imaging hyperCEST experiments. The hyperCEST effect seen in the Z-spectra should easily translate to image contrast, as previously demonstrated for all other hyperCEST agents (43; 144; 109; 118; 123; 146).

4.6 Conclusions

In this chapter, MB were characterized as possible hyperCEST agents. We demonstrated the ability of hyperCEST to detect MB at the dose typically used for clinical US imaging, a dose at which MB cannot be directly detected by current MR techniques. Since MB are able to interact with 10s of billions of ^{129}Xe atoms per second they can efficiently provide substantial hyperCEST contrast at clinically relevant concentrations. The wider chemical shift difference between dissolved-phase and gas-phase signal, along with the much narrower frequency distribution of ^{129}Xe inside the MB core leads to more efficient spin saturation, and to a reduction in SAR exposure for clinical translation. Their biocompatibility, higher detection sensitivity, and more efficient saturation are pivotal to future human translation of hyperCEST techniques and to the use of MB as a true dual modality contrast agent.

CHAPTER 5: *IN VIVO* HYPERCEST IMAGING

This section presents results that have been previously published in the journal Magnetic Resonance in Medicine[1].

5.1 Introduction

CEST has been used to detect endogenous metabolites that can provide functional information in brain (124; 125; 126; 127), breast (128; 129), and prostate (130; 131) tumors. In the previous two chapters we have shown that the size of the CEST contrast is determined by the ratio between the exchangeable protons and the bulk water protons present in the tissue of interest. If HP nuclei are used for detection (hyperCEST), the detectable concentration of the HP solvent spins can decrease along with the needed concentration of the solute spins, thus enhancing MR detection sensitivity (116).

While the first *in vitro* hyperCEST demonstration dates back to 2006 (43), *in vivo* translation has lagged far behind, with a single *in vivo* demonstration in rats reported in 2017 using CB[6] (123), a biocompatible (139; 140; 141; 142) and commercially available synthetic molecular cage (4Å diameter (135)) capable of hosting a single Xe atom that is in rapid chemical exchange with the solvent. The lag between *in vitro* and *in vivo* translation can be attributed not only to the well-known difficulties associated with imaging the dissolved-phase xenon signal in small animals, but also to the difficulty of reaching the steady-state dissolved-phase ^{129}Xe magnetization needed to obtain a reliable hyperCEST contrast. Unlike the concentration of water protons in tissues, the concentration of HP ^{129}Xe spins in tissues increases with time during continuous xenon inhalation. Eventually, it is maximized after a time that is tissue-specific and that depends on tissue blood flow and the specific xenon solubility and T_1 in the tissue of interest.

Here, while reporting on the first *in vivo* demonstration of hyperCEST contrast in mice at high field using CB[6], we detail the experimental protocol needed to achieve a steady-state dissolved-phase xenon magnetization and a reliable hyperCEST contrast *in vivo*.

[1]McHugh, CT, Kelley, M, Bryden, NJ, Branca, RT. In vivo hyperCEST imaging: Experimental considerations for a reliable contrast. Magn Reson Med. 2021; 00: 1– 10. https://doi.org/10.1002/mrm.29032

5.2 Materials and Methods

Animal Preparation

A total of n = 7 balb/c female mice, 2–3 months old, used for these studies. All animal experiments were performed according to the ethical guidelines for animal experiments as described in the Public Health Service Policy on Humane Care and Use of Laboratory Animals (179), the Animal Welfare Act and Animal Welfare Regulations (180), and the Guide for the Care and Use of Laboratory Animals (181) under an animal protocol approved by the Institutional Animal Care and Use Committee of the University of North Carolina at Chapel Hill.

Mice were anesthetized with an intraperitoneal injection of 70 mg/kg of pentobarbital, perorally intubated, and mechanically ventilated by using a homemade, HP-compatible ventilator similar to the one described in Nouls et al. (171) The ventilator delivered a tidal volume of 0.15 mL of a gas mixture of either O_2/N_2 or O_2/HP-Xe in a 1:3 gas-volume ratio, at a rate of 80 breaths/min, with a 150 ms inhalation duration, a 200 ms breath-hold, and a 350 ms exhalation duration (Figure 5.1).

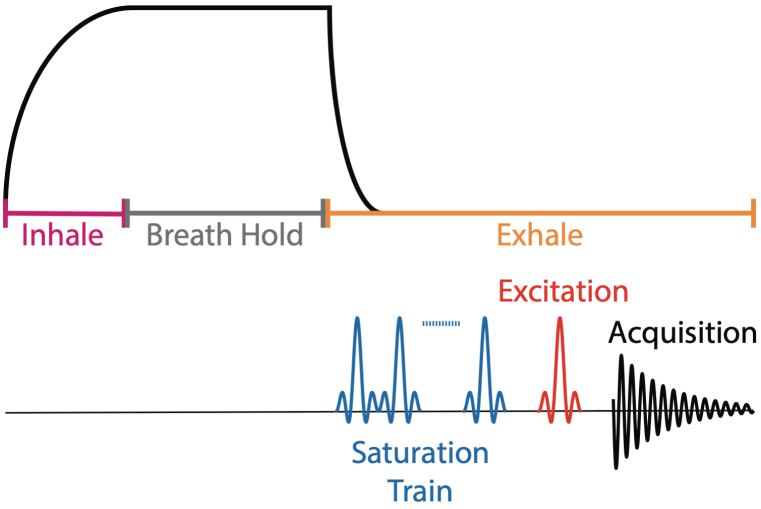

Figure 5.1: Ventilator trigger and pulse sequence timing. Mice were ventilated by using a homemade HP-compatible ventilator that was controlled by LabVIEW to allow for precise control of tidal volume and timing. The breathing rate was 80 breaths/min with an inhalation duration of 150 ms, a breath-hold of 200 ms, and an exhale phase of 350 ms. RF saturation followed by RF excitation and acquisition was triggered by the ventilator during the exhale phase, either every breath, or every second, third or fourth breath.

Xenon gas was polarized to approximately 15% as described previously. A single bag of HP gas was produced every 20-30 minutes and enabled the acquisition of 4-6 Z-spectra, or 4-5 MR images. For all

MR experiments, saturation, excitation, and signal acquisition were directly triggered by the ventilator during the exhalation phase of the breath cycle), either after every breath-hold or after every second, third or fourth breath-hold of HP ^{129}Xe gas. (Figure 5.1).

In Vivo NMR Spectroscopy and Imaging

All spectroscopic and imaging experiments were performed using a 9.4 T small animal MR scanner (BioSpec 94/30, Bruker Biospin, USA), using a 35 mm dual-tuned ^{1}H/^{129}Xe volume coil (m2m Imaging Corp.) Mice were positioned inside the coil with the heart located at the center of the coil and in the magnet's isocenter. Serial Z-spectra and images were acquired before and after the injection of a 0.1 mL PBS suspension of CB[6] (Sigma-Aldrich, St. Louis, USA), at either a 10 mM or 20 mM CB[6] concentration, which resulted in an in-blood CB[6] concentration of approximately 1 mM or less.

HP ^{129}Xe spectra and images were acquired with a standard FLASH pulse sequence right after applying a presaturation pulse train made of sixteen 3-lobe sinc pulses, each with a 20 ms duration, a bandwidth of 310.5 Hz, and a nominal flip angle of 400°. The center frequency of the RF train was varied from -700 ppm to 200 ppm, with denser spectral acquisition near the frequency of ^{129}Xe in CB[6], centered at -71.8 ppm (135) from the dissolved-phase ^{129}Xe frequency, placed at 0 ppm. A 2 ms 3-lobe sinc pulse, with a 90° nominal flip angle, on-resonance with the dissolved-phase xenon spins (110.75 MHz), was used to excite the spins. ^{129}Xe spectra were acquired using a spectral width of 55556 Hz, 7776 data points, and 2 averages. The initial spectra, acquired with a saturation frequency from -700 ppm to -400 ppm from the dissolved-phase ^{129}Xe frequency, displayed a non-constant intensity of the dissolved-phase ^{129}Xe signal and were removed from the analysis.

For each mouse, multiple Z-spectra were collected using the same bag of HP ^{129}Xe. For each set, the synchronization between the breathing pattern and the MR acquisition (i.e. with saturation/acquisition performed after every breath-hold or after every second, third or fourth breath-hold) was chosen in a random order to offset any possible effects from CB[6] clearance during the acquisition of the entire set of Z-spectra.

Sets of hyperCEST images were acquired after applying the RF pulse saturation train described above, either with an on-resonance (-71.8 ppm) or an off-resonance (+71.8 ppm) saturation frequency. To offset any possible effect from the depolarizing gas and to minimize any spurious signal fluctuation, with every

fresh bag of HP ^{129}Xe gas, after the acquisition of a full Z-spectrum, four sequential images were acquired (alternating between on- and off-resonance saturation).

Anatomical ^{1}H images were acquired by using a Fast Low Angle Shot (FLASH) pulse sequence with a field of view of 60 mm x 30 mm, a matrix size of 64 x 32, an echo time of 3.6 ms, a spectral bandwith of 50000 Hz, and a flip angle of 20°.

Post processing was done in MATLAB R2019b (The Mathworks, Inc., Natick, Massachusetts, US). Z-spectra were formed by plotting the normalized, T_1-corrected, solvent ^{129}Xe signal integral as a function of the B_1 offset frequency, as previously done (111). To generate hyperCEST contrast maps, the same intensity threshold was applied to off-resonance and on-resonance images as done previously (132), in order to limit the contribution of noise to the hyperCEST contrast calculation. HyperCEST contrast maps were then generated pixel-by-pixel by subtracting the on-resonance image from the subsequent off-resonance image, before renormalization by the off-resonance pixel value.

5.3 Results

In Vivo NMR Spectroscopy and Z-spectra

Figure 5.2 shows an example of the non-localized dissolved-phase signal acquired on one of the mice, as well as the change in signal intensity obtained at the beginning of each acquisition before a steady-state magnetization was established. The same signal behavior was observed in all our experiments, both before and after CB[6] injection, prompting us to acquire a series of off-resonance saturation dummy scans before the acquisition of every Z-spectrum and image.

The observed dissolved-phase signal behavior can be easily explained. Immediately after the beginning of HP ^{129}Xe gas inhalation, the dissolved-phase ^{129}Xe magnetization slowly starts to grow as more HP ^{129}Xe accumulates into tissue despite continuous RF excitation with a nominal 90° pulse that had been previously calibrated using a sample containing ^{129}Xe in oil at high pressure. This transient increase is followed by a steady decrease produced by the repeated RF excitations, until a steady-state condition is reached. On the other hand, in spectra acquired after several minutes of HP ^{129}Xe inhalation, the dissolved-phase magnetization has already reached its maximum value in tissue, and only a consistent decrease of the tissue-dissolved-phase magnetization is observed due to the continuous RF excitation until a steady-

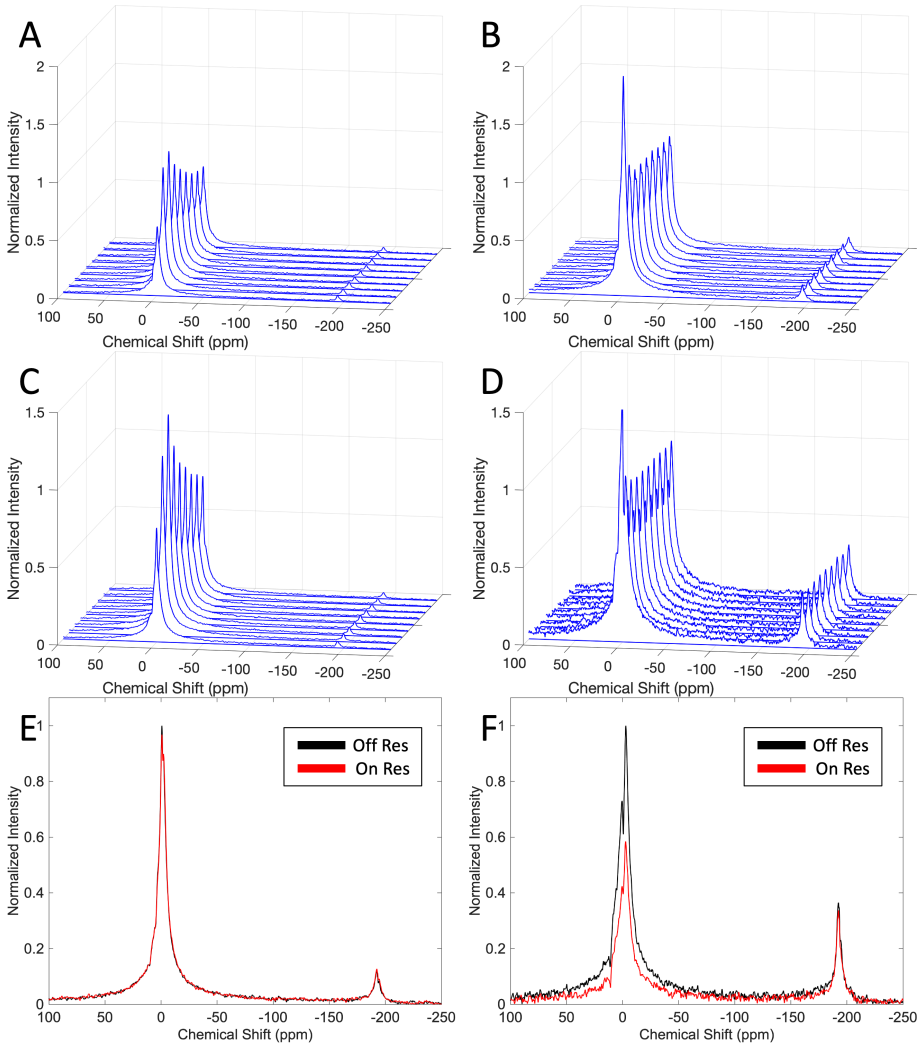

Figure 5.2: Dissolved-phase signal variation observed at the beginning of a Z-spectrum acquisition. In order to indirectly detect the dilute CB[6] signal, consecutive ^{129}Xe spectra were acquired after a train of saturation pulses with an offset frequency that varied from -700 ppm to +200 ppm. The intensity of the dissolved phase in the first off-resonance spectra varied in a consistent manner across all mice. All spectra shown here were normalized to the dissolved-phase signal intensity of the off-resonance signal corresponding to a presaturation frequency of +200 ppm. (A) and (B) show an example of the first 9 spectra obtained from a mouse before CB[6] injection, and (C) and (D) show corresponding spectra after CB[6] injection (0.1 mL volume with a 10 mM CB[6] concentration). (A) and (C) were collected 10s after the inhaled gas was switched from the O_2/N_2 mixture to the O_2/Xe mixture. The intensity of the dissolved phase was observed to increase and then decrease before reaching a constant value. (B) and (D) were collected three-minutes after the inhaled gas was switched from the O_2/N_2 mixture to the O_2/Xe mixture. In this case the intensity of the dissolved phase peak was observed to steadily decrease over time before reaching a constant value. (E) Off-resonance and on-resonance (-71.8 ppm) spectra collected before (E) and after (F) CB[6] injection after allowing the dissolved phase magnetization to stabilize. After the acquisition of dummy scans a consistent dissolved-phase signal reduction was observed in all mice with on-resonance saturation of the CB[6]-bound ^{129}Xe only after CB[6] injection.

state tissue-dissolved ^{129}Xe magnetization is reached. Only after a steady-state condition for the dissolved-phase magnetization has been reached, a consistent drop in dissolved-phase signal intensity is observed upon saturation of CB[6]-bound ^{129}Xe resonance and after CB[6] injection.

Figure 5.3 shows sets of Z-spectra acquired *in vivo* on the same mouse after a first (10 mM) and a second (20 mM) injection of CB[6], both 0.1mL in volume. Without CB[6], no signal loss is observed at -71.8 ppm. In the presence of CB[6], the observed signal loss depends on the frequency with which the caged spins are saturated during the breathing cycle. Specifically, a 40% signal reduction was achieved with 0.3 μT when ^{129}Xe bound to CB[6] was saturated after every breath-hold, whereas a reduced dissolved-phase signal loss was observed when ^{129}Xe bound to CB[6] were saturated every second, third, or fourth breath-hold, regardless of the order with which these Z-spectra were acquired. This trend was observed across multiple mice.

A similar behavior was observed when saturating the gas-phase signal. In this case the signal loss was observed independently of the presence of CB[6], as one would expect from the direct destruction of the ^{129}Xe gas-phase magnetization in the lungs. In this case, the signal loss was about 90% when saturation occurred at the end of each breath-hold, and less than 90% when saturation occurs every second, third, or forth breath-hold. The residual dissolved phase signal observed after saturation of the gas phase signal at the end of every breath-hold originates from the gas that was able to diffuse from the lung airspaces into the blood stream during the breath-hold, before saturation began. Therefore, the residual signal after the gas phase saturation can be taken as a surrogate measure of the lung gas exchange efficiency, similarly to the Xe polarization Transfer Contrast pioneered by Ruppert and colleagues (182) to determine gas exchange in the lungs.

Interestingly, a residual resonance at 0.07 ppm was clearly observed in two of the seven mice after direct saturation of the dissolved-phase ^{129}Xe signal (Figure 5.4). This peak most likely originates from spins that were able to diffuse from the lung airspaces to the lung parenchyma/blood during the small 5 ms delay that elapsed between the end of the RF saturation and the beginning of the RF excitation, i.e. the pool of spins that are in direct exchange with the gas-phase ^{129}Xe in the lungs.

In Vivo HyperCEST Imaging

Figure 5.5 shows the four HP ^{129}Xe images acquired serially with on-resonance and off-resonance saturation using the same bag of HP gas. The images were purposely acquired in series to offset any possible

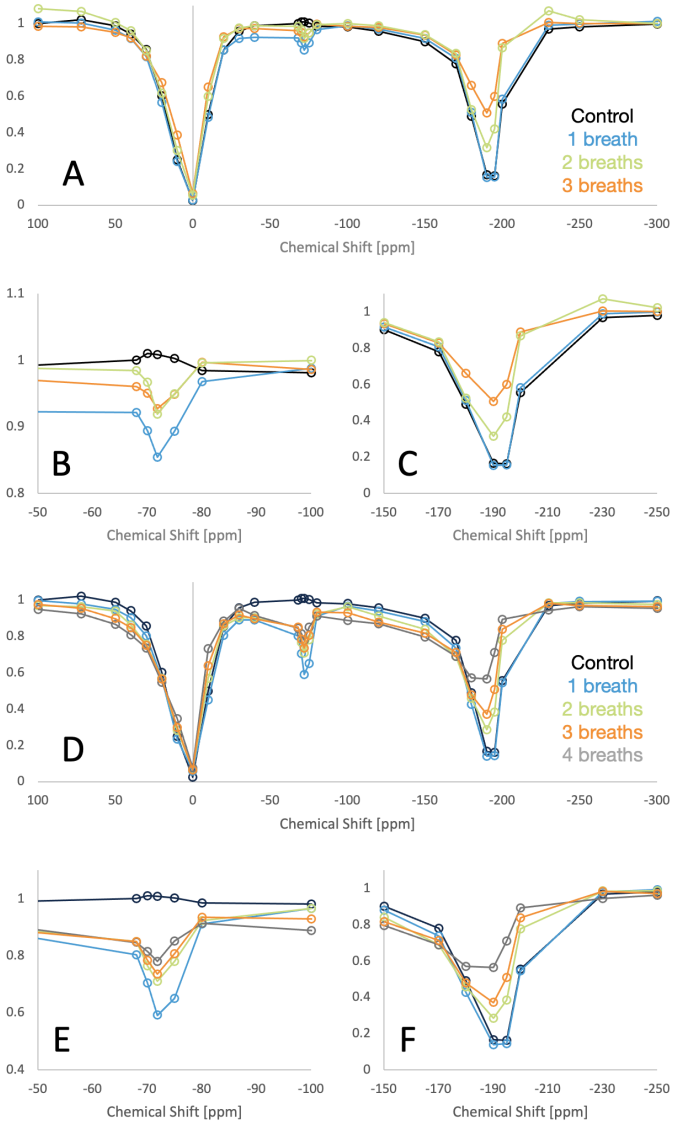

Figure 5.3: *In vivo* Z-spectra acquired before and after CB[6] injection. Z-spectra were collected by monitoring the normalized dissolved-phase signal as the presaturation pulse frequency was varied across the spectral width. Initial data points were discarded due to the observed signal intensity changes observed at the beginning of each experiment. The lines do not represent any sort of fitting, but they rather simply connect data points from the same hyperCEST run. (A-C) Z-spectra resulting from a 0.1 mL bolus injection of a 10 mM CB[6] suspension; (D-F) Z-spectra acquired on the same mouse after a second 0.1 mL bolus injection (occurred about one hour after the first injection), of a 20 mM CB[6] suspension. The animal tolerated well the higher dose of CB[6]; (B) and (E) represent zoom-in of the Z-spectra near the CB[6]-bound ^{129}Xe frequency. A clear dissolved-phase signal reduction is observed with saturation of the CB[6]-bound ^{129}Xe only after CB[6] injection. A larger hyperCEST effect is observed after the second CB[6] injection. HyperCEST effect is greater when saturation is performed during every breath, versus when is performed every second, third, or forth breath. Saturation of the gas phase signal produced also a consistent reduction of the dissolved phase signal, before and after CB[6] injection. Again, a greater reduction is observed when saturation is performed every breath.

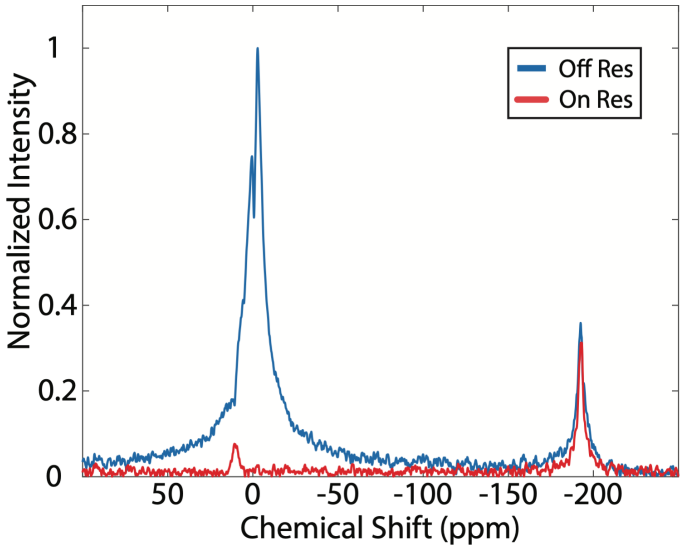

Figure 5.4: ^{129}Xe spectra after direct saturation of the dissolved-phase signal. When the frequency of the presaturation pulse train was set to 0 ppm, i.e. at the tissue-dissolved ^{129}Xe frequency, the dissolved-phase xenon signal was completely destroyed. In some cases, depending on shimming conditions, i.e. on the frequency distribution in the lungs, a small peak appeared at 0.07 ppm, most likely originating from ^{129}Xe spins in the lung parenchyma and blood that were in direct exchange with the gas-phase pool.

signal loss due to the relaxation of HP gas in the fringe field of the magnet. Interestingly, in every experiment, a consistent signal reduction can be observed with saturation of the CB[6]-bound ^{129}Xe resonance.

Figure 5.5 also shows the hyperCEST contrast maps fused to an anatomical coronal proton image. Significant hyperCEST contrast is observed in the heart of the mouse and along major blood vessels, including the vena cava. Figures 5.5A-5.5C were acquired after saturating the CB[6]-bound ^{129}Xe signal after every breath-hold, or after every third or fourth breath-hold. This trend was observed across multiple mice. A reduction in hyperCEST contrast is observed when saturation is not performed after every breath-hold, consistently with what was observed in the Z-spectra. This contrast behavior is consistent with a three-pool chemical exchange model in which one pool represents xenon dissolved in blood (in these mice, ^{129}Xe dissolved in plasma and bound to red blood cells cannot be resolved), one pool represents ^{129}Xe bound to CB[6], and one pool represent ^{129}Xe dissolved into tissues. While exchange rate between the first two pools is quite fast, exchange rate between blood and tissue is much slower. As such, the inverse of the difference in hyperCEST contrast obtained when saturating after every breath-hold or after every second breath-hold could be interpreted as a surrogate measurement of xenon transfer efficiency between blood and tissue.

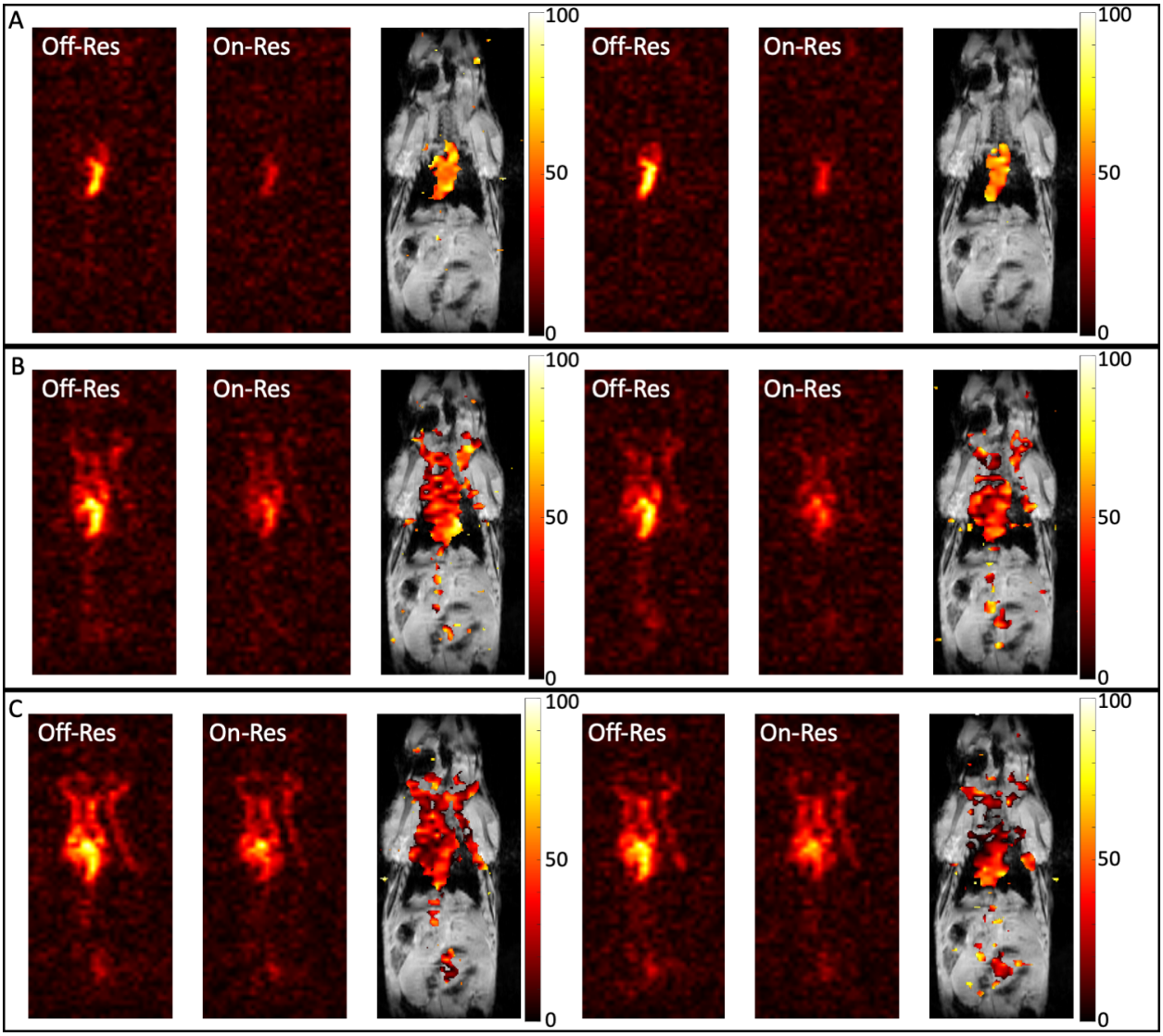

Figure 5.5: *In vivo* hyperCEST maps obtained after CB[6] injection. In each row, left to right, are displayed the two sets of xenon images (offset: -71.8 ppm (On-Res), +71.8 ppm (Off-Res), -71.8 ppm (On-Res), +71.8 ppm (Off-Res)), in the order in which they were acquired, along with the corresponding hyperCEST maps obtained by subtracting the On-Res image from the subsequent Off-Res image, overlapped onto an anatomical 1H image. All images were acquired after a single injection of CB[6] (0.1 mL volume with a 20 mM CB[6] concentration). The four images displayed in each row were acquired in a sequential manner to assess any possible spurious signal fluctuation and by using the same bag of HP gas after the acquisition of a full Z-spectrum and five dummy scans. Similar to what was observed in Z-spectra, the reduction in the dissolved phase signal is maximized when saturation and acquisition is performed during every breath (A), compared to every three breaths (B), or every four breaths (C).

5.4 Discussion

Molecular imaging with MRI has been demonstrated *in vitro* with a wide variety of hyperCEST agents that exchange ^{129}Xe with their environment (110; 112; 138; 183). But, as of yet, the only *in vivo* applica-

tion was shown in rats using CB[6] (123), a commercially available Xe host that can be detected in human plasma at a concentration of 1 mM (135).

Here, we show that *in vivo* translation of hyperCEST presents several challenges when compared to proton CEST. Unlike proton CEST, where bulk and exchangeable protons are endogenously present at a given concentration in tissues, for hyperCEST, both the cage and the bulk ^{129}Xe signal need to be introduced exogenously into the body. Because the hyperCEST contrast requires subtraction of images acquired with an on-resonance and off-resonance saturation, the ability to reach a steady state magnetization before the acquisition of on-resonance and off-resonance images is paramount to obtain a reliable hyperCEST contrast. Specifically, a reliable hyperCEST contrast cannot be obtain just after few seconds from the beginning of xenon inhalation.

Here, by using a mechanical ventilator that can deliver a constant amount of HP ^{129}Xe gas to the mouse at a constant rate, and that can trigger the MR acquisition at specific time points during the breathing cycle, we show that a reliable and repeatable hyperCEST contrast can be obtained only after establishing a steady-state dissolved-phase ^{129}Xe magnetization. As shown in Figures 5.2A and 5.2C, to establish a steady-state dissolved-phase magnetization it takes multiple HP ^{129}Xe breathing cycles and RF cycles, which could prove to be problematic for human translation of this methodology, where ^{129}Xe images are typically acquired during or right after a single breath-hold of HP gas.

We have also shown that the magnitude of the hyperCEST contrast depends both on the relative concentration of CB[6] (110), as well as on the frequency with which the bound spins are saturated during the breathing cycle. Because exchange rate between tissue and blood is relatively slow, saturation of the CB[6]-bound ^{129}Xe spins only partially effects the dissolved-phase pool when performed every other breath or less frequently. While in our studies the dissolved-phase peak was quite broad, preventing us from differentiating between ^{129}Xe dissolved in blood and ^{129}Xe dissolved in tissues, we could not detect specific changes in the dissolved-phase signal intensities. Relative differences in hyperCEST contrast between these pools, however, could potentially reveal the Xe gas exchange rate between tissue and blood. The presence of multiple pools makes the analysis more interesting but also more complicated, as it is typical for more complex exchange systems in CEST (148; 149; 184).

Although CB[6] has shown great potential *in vitro*, it is an inefficient *in vivo* hyperCEST agent because it is prone to bind a wide variety of analytes (145) that can hinder the exchange of ^{129}Xe (185).

Thus, excessive doses are required *in vivo* compared to *in vitro*. Despite the high dose used here, no immediate nor long-term toxic effects were observed in the small number of mice used for these experiments.

It is important to note that a quantitative analysis of the percentage of signal loss as function of CB[6] dose cannot be done for these studies as the in-blood concentration of CB[6] for each experiment was not known. The blood half-life of CB[6] is indeed not known and therefore an estimation of the effective dose at a given time point post injection cannot be made. While our hyperCEST experiments (Figure 5.6) suggest that the concentration of CB[6] does not vary greatly over the course of 10 minutes, an in-blood concentration reduction can be easily observed as a reduction of the hyperCEST contrast after 50 minutes (Figure 5.6). To further complicate the quantification issue, the low solubility of CB[6] in the oversaturated suspension, coupled with the need to perform the injection *in situ* in the magnet using a long tail vein catheter, led to an overestimation and possibly also to a high variability in the effective dose injected. Nonetheless, when two injections were performed sequentially on the same mouse, a clear enhancement in the hyperCEST contrast was observed with the increased CB[6] dose, as one would expect.

5.5 Conclusions

HyperCEST has been demonstrated *in vitro* using a variety of contrast agents but the *in vivo* demonstration was reported only recently in rats using CB[6]. Here, we report the experimental conditions needed to obtain a reliable hyperCEST contrast *in vivo*. Specifically, a reliable hyperCEST contrast can only be obtained after the dissolved-phase xenon magnetization reaches a steady state condition, i.e. after several seconds from the beginning of the xenon inhalation and RF excitation, and only upon careful synchronization of the MR acquisition with the HP ^{129}Xe breathing rate. We also show that the intensity of the hyperCEST contrast *in vivo* is strongly influenced by the frequency with which bound xenon is saturated during the breathing cycle.

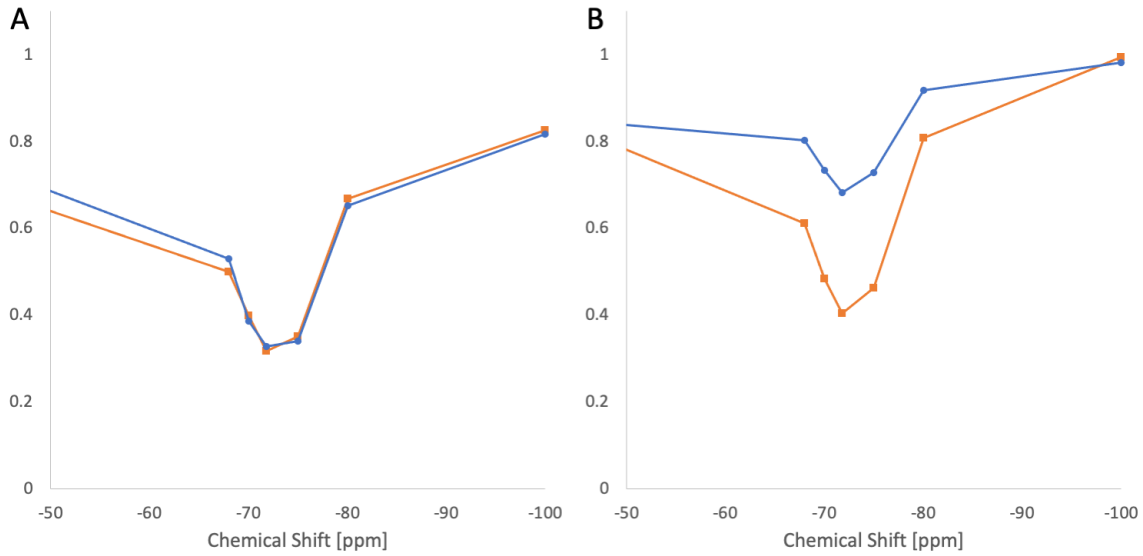

Figure 5.6: CB[6] clearance over time. The amount of hyperCEST contrast is directly related to the in-blood concentration of CB[6]. Because the half-life of CB[6] in blood is not known, it is difficult to accurately quantify the *in vivo* concentration of CB[6] for each of the presented data. Here we show 2 zoomed-in Z-spectra, near the CB[6]-bound xenon frequency, that provide some insights on CB[6] clearance. In (A) are shown Z-spectra acquired few minutes after CB[6] injection with an RF frequency saturation performed every breath. Blue data points were acquired 10 minutes after the acquisition of the orange data point. No change in contrast is noted between the two experiments. In (B) the same orange data points shown in (A) are shown along with similar data points, shown in blue, acquired 50 minutes later. A great reduction in hyperCEST contrast is observed in the blue Z-spectrum acquired 50 minutes later. While these data cannot be used to extract CB[6] blood half-life, they clearly indicate that CB[6] can be assumed to remain constant during the course of 10 minutes, but after several tens of minutes such assumption can no longer be made.

CHAPTER 6: PERFLUOROCARBON NANODROPLETS AS DUAL-PHASE DUAL-MODAL CONTRAST AGENTS

6.1 Introduction

Microbubbles (MB) are gaseous microspheres that are clinically used as a contrast agent for ultrasound (US) and molecular imaging applications (63; 64; 65; 66). They can also be used for targeted delivery of oxygen (60), which makes them a practical theranostic agent. Because of the large susceptibility difference between the heavy-gas interior and the solvent exterior, there has been interest in developing MB as a dual-modality contrast agent for combined US and MRI applications (61; 164; 186). However, direct detection based on susceptibility-based T_2^* image contrast is relatively weak, and MR detection required concentration in excess of what is used for clinical US (164). MR sensitivity to MB can be significantly enhanced with chemical exchange saturation transfer (CEST) with hyperpolarized (HP) ^{129}Xe (hyperCEST) (111). Compared to typical hyperCEST molecular cages with a single binding site, MB are highly efficient hyperCEST agents because each MB interacts with millions of ^{129}Xe atoms at a time even when they are present at low concentration. For *in vitro* experiments, MB have the advantage of being easily separated from the dissolved-phase ^{129}Xe signal, allowing for selective saturation and isolated detection.

In vivo use of MB as hyperCEST agents has been proved to be challenging. HyperCEST has been performed *in vivo* in rats (123) and mice (97) using CB[6] as the molecular cage. While on-resonance saturation of CB[6] produced the desired contrast at -71.8 ppm (with respect to the dissolved-phase ^{129}Xe signal), Z-spectra also indicated a significant magnetization transfer effect after presaturation near the ^{129}Xe gas-phase resonance frequency (-194 ppm) (97). The lungs serve as reservoir of HP ^{129}Xe since, for *in vivo* applications, ^{129}Xe is supplied to the blood via ventilation. As ^{129}Xe remains in the gas-phase within the lungs, on-resonance presaturation of the gas phase induces a magnetization transfer effect from the lungs at the same frequency for which hyperCEST with MB would also be activated. Due to the im-

mense disparity between lung volume and MB volume, it is a challenge to separate and isolate the MB hyperCEST effect.

Perfluorocarbon (PFC) nanodroplets have also been shown to give rise to hyperCEST contrast. Nanodroplets are formed by condensing the gas-phase core of MB into the liquid phase. This is accomplished by subjecting MB to high pressures and low temperatures. Nanodroplets can more easily carry and deliver a payload as, unlike the larger MB, they are not constrained by size as MB (187; 188). With the application of US waves, nanodroplets can expand back to gas MB, which then enables their detection via US. This process is known as acoustic droplet vaporization (ADV) (187). This phase-change contrast agent (PCCA) provides utility in both the liquid-phase and the gas-phase.

Perfluorooctyl bromide (PFOB) nanodroplets have already demonstrated hyperCEST, and are activated by an on-resonance frequency of -82 ppm (116; 109), well separated from both the xenon dissolved-phase and gas-phase resonances. PFOB is classified as a high-boiling point PFC and is a liquid at room temperature, requiring high acoustic pressures for ADV which may be damaging to tissues. Alternatively, nanodroplets filled with low-boiling point PFC, such as decafluorobutane (DFB), transition at lower acoustic pressures, making them more suitable for biomedical applications. Here, DFB nanodroplets, the condensed form of the same MB that previously exhibited the hyperCEST effect (111), were explored as an alternative hyperCEST agent. Because the resonance frequency of xenon dissolved in the DFB core is well separated from the resonance frequency of xenon in the gas phase, nanodroplets could ultimately enable their use as an *in vivo* PCCA for both US and MRI.

6.2 Three-Pool Exchange Model

HyperCEST involves the chemical exchange of HP ^{129}Xe between magnetically distinct spin-pools. The 2-pool exchange theory was presented in Chapter 3. Now here in Chapter 6, ^{129}Xe is subject to chemical exchange between 3 separate pools: solvent (Pool A), MB (Pool B), and nanodroplets (Pool C). Multipool exchange is a common occurrence in ^{1}H CEST where the BM equations have been extended to incorporating up to four pools (148). A multi-pool system is more analogous to a biological system where the nucleus can exchange between various tissues and is not just isolated to blood/carrier compartments (97; 144; 123). HyperCEST is particularly adept for probing complicated systems because the wide chemi-

cal shift range of ^{129}Xe, allowing for the presaturation frequency to activate a specific molecule for multiplexed purposes (109; 118).

The BM equation (Eq. 3.4) models the evolution of magnetization as spins exchange between pool and relax at different rates. As a spin exchanges out of a pool, it carries its magnetization into its destination. This results in a decrease in magnetization of the original pool (i) at a rate of k_{ij} and an increase in magnetization of the new pool (j) at a rate of k_{ji}. Between dilute pools (Pool B and Pool C), the exchange rate is generally considered negligible, and often one assumes that each diluted pool is in direct exchange only with the large solvent pool (Pool A, Figure 6.1). Thus, the dynamical equation for Pool B remains unchanged from its form in Eq. 3.4, and Pool C can be identically modeled with the substitution of its own relaxation rates and exchange rates. Pool A must be adjusted from its form in Eq. 3.4 to include the exchange with Pool C.

$$\begin{aligned}\frac{d\vec{M}^A(t)}{dt} &= \gamma\vec{M}^A(t)\times\left(\vec{B}_0+\vec{B}_1(t)\right)-\hat{R}^A\left(\vec{M}^A(t)-\vec{M}^A_{th}\right)\\ &\quad -k_{AB}\vec{M}^A(t)+k_{BA}\vec{M}^B(t)-k_{AC}\vec{M}^A(t)+k_{CA}\vec{M}^C(t)\\ \frac{d\vec{M}^B(t)}{dt} &= \gamma\vec{M}^B(t)\times\left(\vec{B}_0+\vec{B}_1(t)\right)-\hat{R}^B\left(\vec{M}^B(t)-\vec{M}^B_{th}\right)-k_{BA}\vec{M}^B(t)+k_{AB}\vec{M}^A(t)\\ \frac{d\vec{M}^C(t)}{dt} &= \gamma\vec{M}^C(t)\times\left(\vec{B}_0+\vec{B}_1(t)\right)-\hat{R}^C\left(\vec{M}^C(t)-\vec{M}^C_{th}\right)-k_{CA}\vec{M}^C(t)+k_{AC}\vec{M}^A(t)\end{aligned} \tag{6.1}$$

As shown in Chapter 3, the 2-pool BM equations can be solved numerically with a simple and fast method that involves a single exponential matrix evaluation of the form (Eq. 3.7) (154). For a 3-pool system, matrices $\mathbf{M}$ and $\mathbf{A}$ can be extended to include Pool C, and the solution (Eq. 3.11) still applies. This can be used to accurately simulate a 3-pool exchange. qHyperCEST using the 3-pool BM solution may also be possible, but may prove to be inaccurate due to the doubling of the parameter space.

The FHC solution provided insight on the reliability of qHyperCEST, but it was only applicable for a 2-pool system (112). Data in this Chapter is fit according to qHyperCEST, but the values for the parameters k_{BA}, f_B, k_{CA}, and f_C may not be accurate. Instead, fits will only be used to identify chemical shifts of nanodroplets and MB, and the expected maximum contrast.

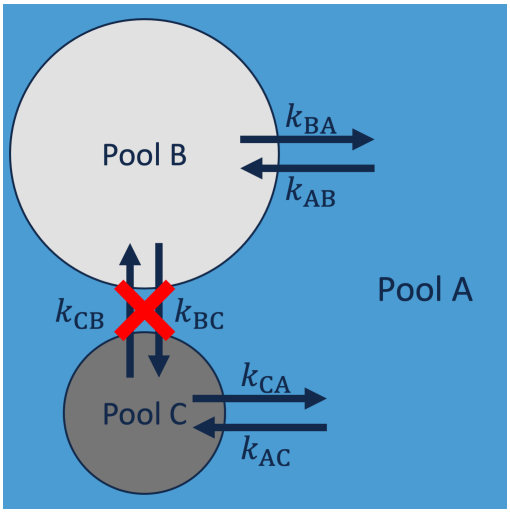

Figure 6.1: Three-pool exchange model. The exchange rate of HP ^{129}Xe is denoted by k with subscripts indicating the original and final pools, respectively. The large, solvent pool (Pool A) is in direct exchange with the two smaller pools (Pool B and Pool C). When Pool B and Pool C are present at low concentrations, it is assumed that there is no direct exchange between Pool B and Pool C.

6.3 Materials and Methods

PFC microbubble and nanodroplet preparation

Nanodroplets were prepared via the condensation method as described in Sheeran et al. (189). Briefly, a solution of DSPC and DSPE-PEG2000 (Avanti Polar Lipids, Alabaster, AL, USA) at a 9:1 molar ratio in phosphate buffered saline, propylene glycol, and glycerol (16:3:1) was prepared. The lipid solution was degassed under vacuum, and the vial headspace was replaced with DFB gas (Fluoromed, Round Rock, TX, USA). MB were generated via mechanical agitation. Nanodroplets were condensed by cooling the bubbles to -13 °C in a chilled ethanol bath, followed by vial pressurization with compressed nitrogen at 20 PSI. MB and nanodroplets were prepared at a concentration of 160 pM. For high-resolution NMR studies, nanodroplets were diluted to 40 pM. For MR imaging studies, nanodroplets were diluted to 50 pM and microbubbles were diluted to 2 pM.

NMR spectroscopy experiments

All spectroscopic studies were performed on a Varian Inova 500 MHz high-resolution NMR spectrometer (Varian NMR Systems, Palo Alto, California, USA) using a ^{1}H-^{19}F/^{15}N-^{31}P PFG switchable broadband probe. The high-resolution spectroscopy methods used here are similar to those described in

Chapter 4. Briefly, the internal temperature of the spectrometer was set to 37 °C in order to replicate *in vivo* conditions. Each droplet sample was placed in a 5 mm (outer diameter) NMR tube and equilibrated to the set temperature before the beginning of each experiment.

HP ^{129}Xe was bubbled directly into the sample through PEEK tubing for 2 s. After a 1 s delay to allow residual HP ^{129}Xe bubbles to rise out of solution, a cw presaturation pulse (B_1=10 μT) was applied for a saturation time of 2 s. A ^{129}Xe spectrum was then acquired using a center frequency of 138.27 MHz (on-resonance with the dissolved-phase ^{129}Xe frequency, here labeled as 0 ppm), a spectral width of 60015 Hz, 8192 data points, 1 average, and a pre-calibrated flip angle of 90°. The frequency of the saturation pulse B_1 was varied across the spectral width, and the intensity of the dissolved-phase peak was monitored. Care was taken to increase the density of measurements around offset frequencies corresponding to the aqueous dissolved-phase ^{129}Xe signal, the PFC dissolved-phase signal, and the gas-phase ^{129}Xe signal.

Following the collection of a full Z-spectrum, the NMR tube that contained the sample was quickly dipped ($<$1 s submerged) into an ultrasonic bath in order to activate the transition from nanodroplets to MB. Another Z-spectrum was then collected to observe the effects of US application on the hyperCEST response of the residual droplets and newly formed MB. This was repeated until the hyperCEST contrast observed was negligible.

Ultrasounic Bath Experiment

To evaluate droplet conversion, droplets were placed into an NMR tube and subjected to US via 0.5 second imersion in an ultrasounic bath. Particle size was measured before and after activation via single particle optical sizing (Accusizer SPOS, Entegris, Billerica, MA, USA).

Analysis

All data processing and fitting were done by using MATLAB R2019b (The Mathworks, Inc., Natick, Massachusetts, US). Initial points upfield from -300 ppm were removed from the analysis due to variable magnetization at the start of each experiment to allow the sample to approach a steady state in dissolved ^{129}Xe concentration (111). The signal intensity of the dissolved-phase ^{129}Xe peak (placed at 0 ppm) was recorded for each B_1 offset frequency. A T_1-correction was applied to these values due to the loss of polarization of the HP ^{129}Xe gas as it sat in the fringe field of the spectrometer. The Z-spectrum was formed

by plotting the normalized T_1-corrected solvent ^{129}Xe signal intensity as a function of the B_1 offset frequency.

The Z-spectrum signals for the nanodroplets and MB were fit separately in order to minimize the volatility of fitting a large array of parameters. This also changed the scenario from a 3-pool system to two 2-pool systems. Thus, the separated Z-spectra could fit according to the FHC solution, as previously published (110; 111; 112; 120). The FHC solution requires much less computational time than the BM solution, yet still extracts similar results (112). The extracted parameters were then applied to the BM solution to display the corresponding fits.

MR imaging experiments

All imaging experiments were performed using a 9.4 T small animal MR scanner (BioSpec 94/30, Bruker Biospin, USA) using a 35 mm dual-tuned ^{1}H/^{129}Xe volume coil (m2m Imaging Corp). Samples of droplets and MB were placed in two separate 10 mm NMR tubes and were positioned horizontally within the bore of the MR scanner, centered on the sensitive region of the dual-tuned ^{1}H/^{129}Xe coil.

HP ^{129}Xe was bubbled directly into each NMR tube separately using the same ventilator system used for the high-resolution studies. Here, the ventilator bubbled for 250 ms. After a 1 s delay to allow residual HP ^{129}Xe bubbles to clear , the ventilator then triggered the MR scanner to apply B_1 followed by image acquisition. To minimize SAR, a train of RF pulses instead of a single cw RF pulse was used for saturation (144; 123). The presaturation pulse was made up of 80 3-lobe sinc pulses, each with a 5 ms duration, a bandwidth of 10 ppm, and a nominal flip angle of 100°. A 1 ms cw pulse, on-resonance with the dissolved-phase xenon spins (110.75 MHz), was used to excite the spins, and images were acquired with a field of view of 50 mm x 50 mm, a matrix size of 64 x 64, an echo time of 2 ms, and a spectral bandwidth of 43859 Hz. Sets of hyperCEST images were acquired after applying the RF pulse saturation train described above, either with an off-resonance or an on-resonance saturation frequency of the targeted pool (-138 ppm for nanodroplets, and -195 ppm for MB). The off-resonance frequencies (+138 ppm for nanodroplets, and +195 ppm for MB) was chosen to be symmetric to the on-resonance frequency about the reference frequency (0 ppm).

^{1}H images were acquired to provide structure context of the phantoms. A Fast Low Angle Shot (FLASH) pulse sequence was used with a field of view of 50 mm x 50 mm, a matrix size of 128 x 128, an echo time of 2.82 ms, a spectral bandwith of 50000 Hz, and a flip angle of 30°.

Analysis

Image processing was also done in MATLAB R2019b (The Mathworks, Inc., Natick, Massachusetts, US). To generate hyperCEST contrast maps, the same intensity threshold was applied to off-resonance and on-resonance images as done previously (132). HyperCEST contrast maps were then generated pixel-by-pixel by subtracting the on-resonance image from the subsequent off-resonance image, before renormalization by the off-resonance pixel value.

6.4 Results

Figure 6.2 shows a high-resolution NMR spectrum of a 160 pM sample of nanodroplets. At this concentration, a ^{129}Xe signal is detected at -138 ppm (referenced to the aqueous ^{129}Xe signal) which corresponds to the resonance frequency of ^{129}Xe dissolved within the core of the nanodroplets. The gas-phase ^{129}Xe within the PEEK tube is detected at -198 ppm. Another signal was observed further upfield at -201 ppm. This signal is consistent with gaseous ^{129}Xe in a spherical compartment, indicating the presence of MB (111). Despite best efforts to formulate and detect a pure solution of nanodroplets, a separate MB peak was always detected. The turbulent bubbling process used to deliver HP ^{129}Xe to the sample unavoidably led to the conversion of some nanodroplets into MB (111; 187). Although the nanodroplet and MB peaks are comparable in amplitude, it is important to note that the phase-change from nanodroplets to MB produces an increase in carrier volume of several orders of magnitude as they go from nano-scale to micro-scale. Since signal intensity is related to spin-density, even a relatively small number of nanodroplets vaporizing into MB can produce significant increase in the signal originating from gas-phase MB core.

As the nanodroplet sample concentration was decreased, its signal was no longer detectable directly with NMR ^{129}Xe spectroscopy, and hyperCEST was used to observe the chemical exchange between nanodroplets and the solvent pool. Figure 6.3 shows a series of Z-spectra collected on the high-resolution spectrometer on a single 40 pM sample of nanodroplets. Initially (Figure 6.3A), direct saturation of the spins dissolved in the nanodroplet core (-135 ppm) produced a 56% reduction of the solvent signal (2 s cw pulse with a B_1 of 10 μT), whereas saturation of the spins residing inside the microbubbles core (-195 ppm) produced a 30% solvent signal reduction.

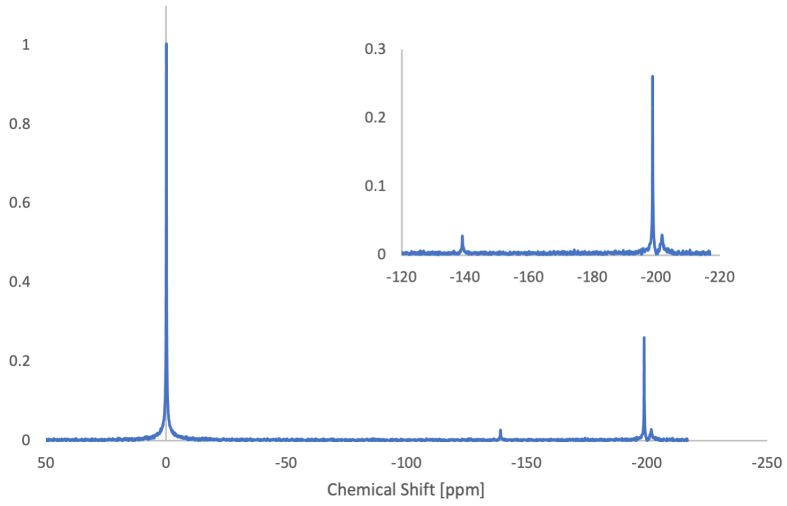

Figure 6.2: Direct detection of MB and nanodroplets. High-resolution NMR spectrum of a full-concentration nanodroplet sample (160 pM) shows very distinct resonances at 0 ppm (solvent dissolved-phase ^{129}Xe), -138 ppm (nanodroplets), -198 ppm (gas-phase signal in PEEK tube), and -201 ppm (MB). The presence of the MB peak demonstrates the difficulty to isolate a pure sample of nanodroplets.

Following the initial Z-spectrum acquisition, the sample was removed from the spectrometer and briefly submerged in an ultrasonic bath to induce ADV. After repositioning the sample back into the spectrometer, another Z-spectrum was acquired (Figure 6.3B). In this case, saturation of the nanodroplet core produced a solvent signal reduction of only 15%, whereas saturation of the MB core produced a slight increase in solvent signal reduction of 33%. Another round of US was applied to the sample followed by Z-spectrum acquisition (Figure 6.3C). Nearly all hyperCEST contrast was eliminated for both nanodroplets and MB. The effects observed in Figure 6.3C indicate that both nanodroplets and MB are completely destroyed by the third application of US. This adds some insight into the behavior observed in Figure 6.3B. The decrease in nanodroplet contrast observed after the first application of US is due to ADV and to an overall decrease in nanodroplet concentration. US also affected the MB concentration, but the it was replenished by the nanodroplets transitioning into MB. The complete destruction of nanodroplets is a multistep process where they contribute to the concentration of the MB pool before dissolution. Thus, using only sufficient exposure to US, nanodroplets can be converted in MB, altering the activation frequency of hyperCEST.

The evolving MB distribution can be seen in Figure 6.3D showing the FHC solution fit of the Z-spectra valleys. The chemical shift of the nanodroplet valley is fairly constant but the MB valley fluctuates. The nanodroplet sample was prepared to be monodisperse, so their size distribution and associated kinetics

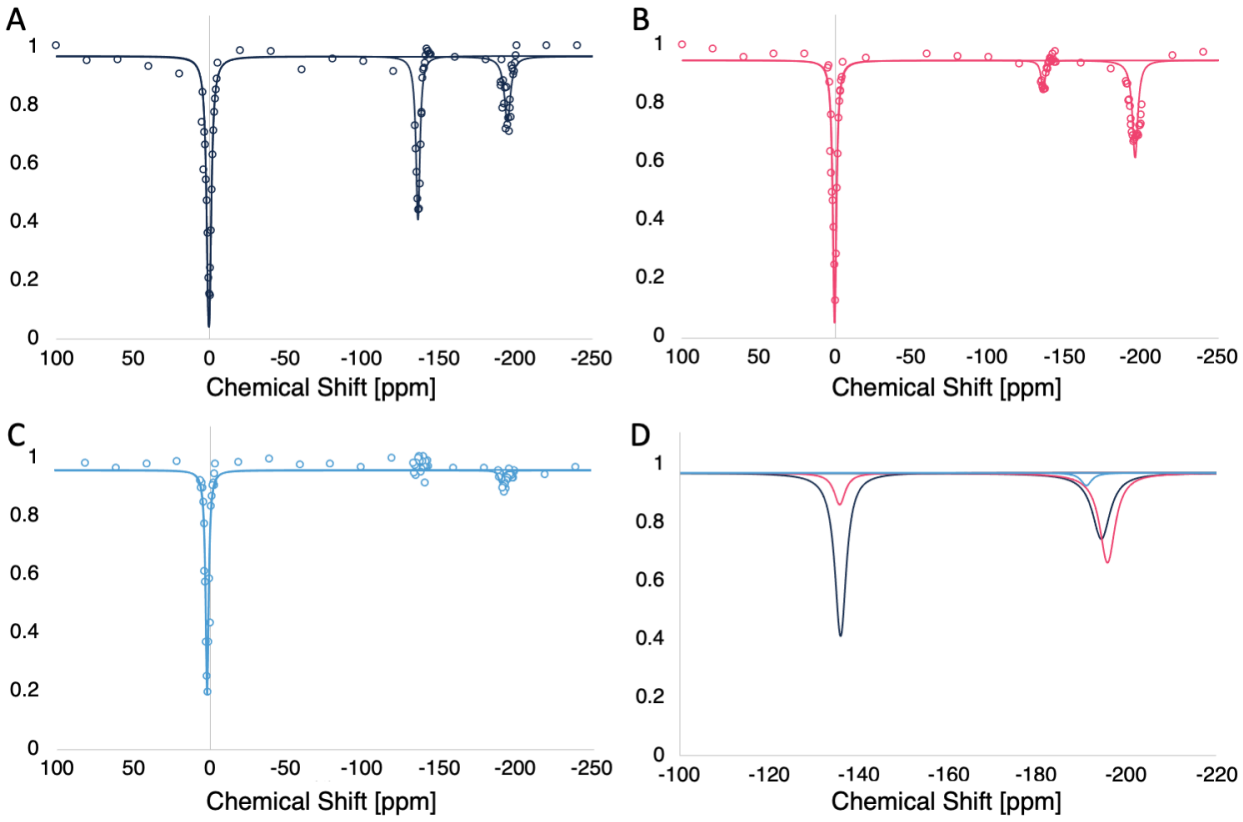

Figure 6.3: High-resolution Z-spectra following acoustic droplet vaporization. Nanodroplet samples were diluted to 40 pM and, nanodroplets were no longer directly detectable. Instead, Z-spectra revealed very strong hyperCEST contrast at the nanodroplet frequency (-135 ppm), as well as the MB frequency (-195 ppm). The initial sample (A) showed the most nanodroplet contrast, and after applying US to the sample, the magnitude decreased (B). Interestingly, the change in MB contrast increased. After another application of US, both resonances were destroyed (C). Z-spectra were fit, and (D) shows the behavior of the contrast agent valleys.

were fairly uniform (Figure 6.4). As such, its corresponding valley is narrow. MB, on the other hand, were formed in an uncontrolled fashion with ADV, resulting in a polydisperse distribution. The wider MB size distribution translated in a wider frequency distribution. The shift observed, on the other hand, may have been the direct effect of a change in the local magnetic susceptibility, and thus a change in the resonance frequency of the dissolved phase that was supposed to be at 0 ppm for all these experiments. This, unlike the resonance of the MB core, is expected to be influenced by the size and concentration of MB.

HyperCEST imaging was done on two separate phantoms placed side by side in the 9.4 T MRI scanner. Figure 6.5 shows a set of dissolved-phase ^{129}Xe images. The nanodroplet solution was placed in the left phantom, and the MB solution was placed in the right phantom. Figure 6.5A and Figure 6.5B show off-resonance images corresponding to symmetric saturation for nanodroplets (+138 ppm) and MB (+195

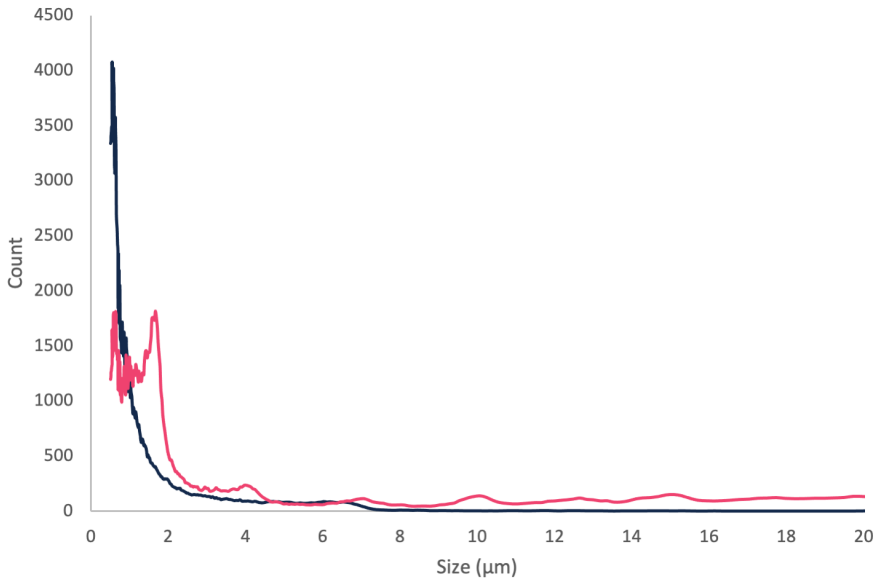

Figure 6.4: Effect of US application on size distribution. A sample of nanodroplets was placed in initially sized and was monodisperse (blue). While in a standard NMR tube, the sample was quickly dipped into an ultrasonic bath. Resizing the sample showed that the size distribution of particles became very irregular, producing much larger MB (fuschia). The optimally sized MB (2 μm) provide the large hyperCEST effect following a single application of US.

ppm), respectively. Following on-resonance saturation, Figure 6.5C shows a drop in signal in the left phantom (-138 ppm), and Figure 6.5D shows a drop in signal in the right phantom (-195 ppm). Here, the phase-dependent multiplex capability of nanodroplets and MB are apparent; their hyperCEST contrast is activated at each phase's specific resonance frequencies.

The set of images took 8 minutes to acquire, and therefore, the relaxation of the ^{129}Xe signal may not be insignificant. In order to observe the T_1 decay, Figure 6.6 shows consecutive dissolved-phase ^{129}Xe images collected from control phantoms containing only PBS. Although small, these images show that the signal does decrease in between images. Therefore, change in contrast displayed in Figure 6.5 underestimates the true contrast.

It was previously shown that upon initiating ventilation of HP ^{129}Xe, the dissolved-phase concentration does not immediately saturate for both *in vitro* (111) and *in vivo* (97) experiments. The same effect was also observed here. Figure 6.7 shows a significant increase in signal between consecutive images taken immediately after the start of HP ^{129}Xe bubbling. These were control samples. Given the order of saturation frequencies (on, off), a false-positive in both phantoms because signal was lower for the on-resonance image than it was for the off-resonance image. Therefore, this is yet another example of the importance of

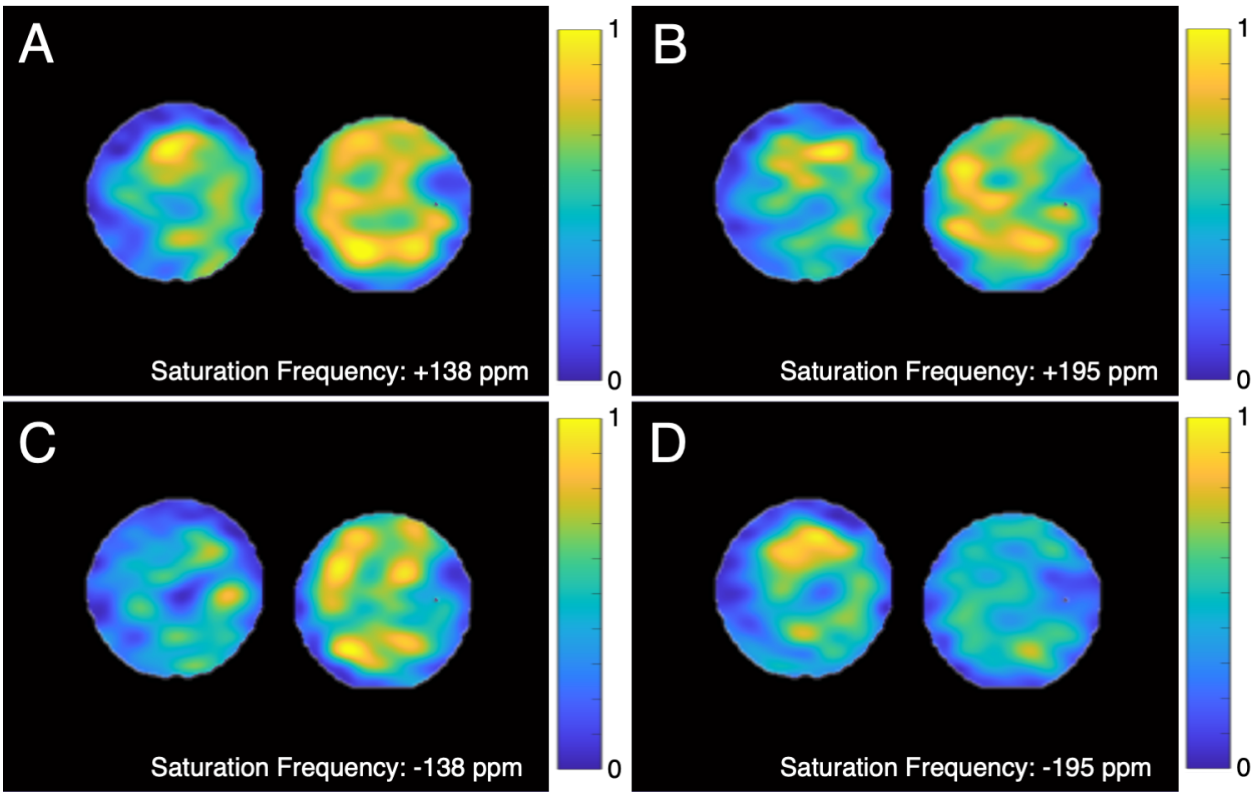

Figure 6.5: HyperCEST imaging of nanodroplet and MB samples. Two 10 mm NMR tubes were filled either a 50 pM nanodroplet sample (left phantom) or a 2 pM MB sample (right phantom). The phantoms were position horizontally in the bore of the magnetic, and HP ^{129}Xe was bubbled directly into them. Compared to the off-resonance image (A), the nanodroplet sample signal decreased following on-resonance presaturation (C). Similarly in the MB sample, on-resonance presaturation (D) decreased the contrast compared to the on-resonance image (B). Images are normalized with respect to the maximum value of their off-resonance counterpart.

establishing a consistent and repeatable initial magnetization in order to accurately identify and quantify the hyperCEST contrast.

6.5 Discussion

Xenon and oxygen are highly soluble in PFC. PFC nandroplets have therefore been used to transport oxygen to tissues and as an hemoglobin substitute (187; 190). In a sense, they are considered to be superior to hemoglobin as their carrying capacity is not limited by binding sites but depends on the partial pressure of the gas. In fact, in 1966, anesthetized mice were shown to survive for 4 hours while being submerged in liquid PFC equilibrated to atmospheric pressure (191). As nano-scale carriers, nanoemulsions can transport gas deep within the vasculature, reaching narrow areas that impede MB access. As xenon is

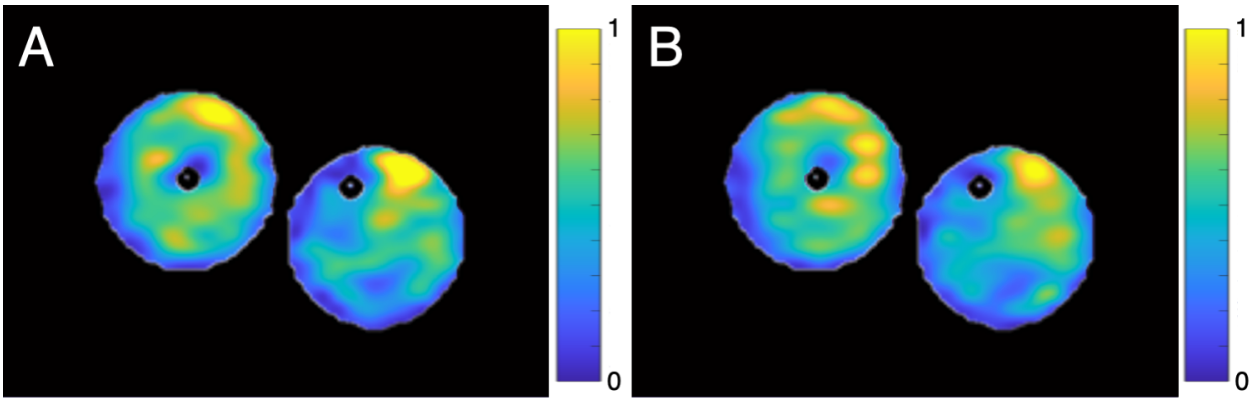

Figure 6.6: Signal loss due to T_1 relaxation in between consecutive images on two control samples. Images A and B were acquired one after the other, and are normalized with respect to the maximum intensity of image A. Due to the prolonged repetition time, the signal decay of the HP ^{129}Xe bubbled into the samples is not negligible. Considering that on-resonance images were acquired before off-resonance images, and considering the non-negligible T_1 relaxation between the two acquisitions, the change in contrast as shown in Figure 6.5 is an underestimation of the true hyperCEST contrast.

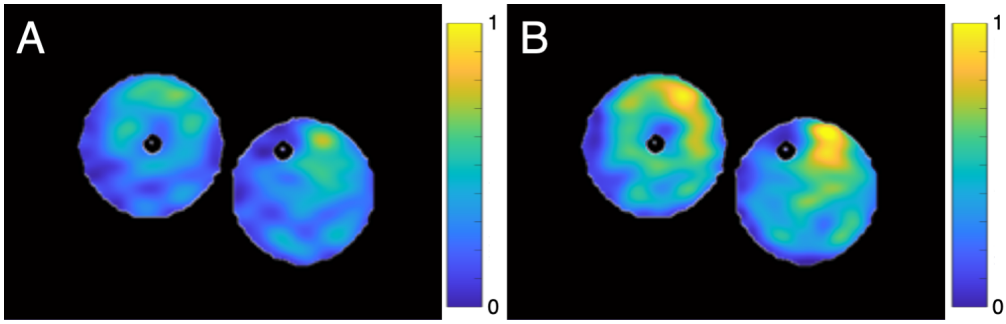

Figure 6.7: HP ^{129}Xe saturation in solution. When HP ^{129}Xe ventilation begins, it takes time for ^{129}Xe to accumulate to saturation. As a result, consecutive images (A followed by B) collected immediately after the introduction of HP ^{129}Xe will show an increase of signal. This may indicate a false-positive hyperCEST contrast even for control samples, as shown above. Thus, it is vital to establish a steady-state magnetization before attempting hyperCEST. Images are normalized to the maximum intensity of B.

also highly soluble in PFC (192), nanodroplets have also been used as a mean for intravenous delivery of HP ^{129}Xe for *in vivo* MR applications (115).

We have shown that *in vivo* detection of MB by hyperCEST is challenged by the presence of the large gas reservoir in the lungs, that is directly saturated during an hyperCEST experiments, whether or not MB are present in circulation. Overlapping signals in a Z-spectrum is not usually a lost cause, and is a common feature in ^{1}H CEST. Chemical shifts in ^{1}H CEST are usually only a few ppm, and a formal magnetization transfer ratio asymmetry analysis can be used to separate contrast-agent resonances from the direct saturation of the solvent pool (117). This is not as straightforward for the gas-phase ^{129}Xe signal

in the lungs because of the large frequency distribution of the gas in this compartment. A better approach would be to take advantage of the extreme sensitivity that ^{129}Xe has to its environment and detect signal that is separated not only from the dissolved-phase signal, but also the gas-phase signal.

Figure 6.2 showed a nanodroplet resonance at -138 ppm, which is 60 ppm shifted downfield from the MB signal. Based on *in vivo* Z-spectra, this chemical shift should be resolvable *in vivo* (97). It is interesting to point out that the Z-spectra shown in Figure 6.3 indicate that the nanodroplet and MB resonance frequencies were located at -135 ppm and -195 ppm, respectively. The chemical shifts between the carriers remained at 60 ppm, but their frequencies with respect to the solvent were shifted. This might be due to the difference in concentration perturbing the microscopic magnetic field within the solvent. This is further supported by the analysis seen in in Figure 6.3D.

While fitting the Z-spectra, the BM solution was initially used due to the fact that this is a 3-pool system. It was fairly difficult to get the optimization algorithm to converge on a solution with such a large parameter space. When it did converge, it had difficulty establishing an accurate linewidth of the valleys, most likely indicating a miscalculation of the exchange rates. It was previously shown that the accuracy of qHyperCEST depends on whether B_1 is in the weak saturation regime or the strong saturation regime. Further studies should test the tolerance of qHyperCEST with handling multiple spin pools. Foregoing the BM solution, instead, the nanodroplet valley and the MB valley were fit separately using the FHC solution. This approach was able to fit each valley very well as shown in Figure 6.3. There is still doubt on the resulting kinetic parameters, but the chemical shifts seem to be accurate.

Figure 6.5 shows the multiplexed imaging capabilities of nanodroplets and MB. Multiplexed hyperCEST imaging was previously demonstrated with a sample of various of gas vesicles by Shapiro et al. (118) and also a solution of Cry-A and PFOB nanodroplets by Klippel et al. (109). While their samples contained a collection of different carriers, the nanodroplet and MB used here are made of the same PFC in different physical states. Similar to US employing either nanodroplets or MB based on whether application calls for optimal therapeutic or imaging capabilities, respectively, nanodroplets or MB can be activated with hyperCEST based on the scenario. *In vivo*, the nanodroplet form allows for the signal to be separated from the gas-phase signal in the lungs. *In vitro*, or if the gas-phase in the lungs can be avoided with the use of a surface coil, MB would be the superior hyperCEST agent due to their larger carrying capacity (111). This disparity in efficiency is clear form Figure 6.3A where MB produced substantial contrast even in a solution expected to contain a much higher concentration of nanodroplets.

6.6 Conclusions

Nanodroplets filled with low-boiling point PFC are a PCCA that can easily be converted into MB using US. Their detection by hyperCEST, at the clinically relevant doses used for US, could enable their use as dual-modality PCCA. Here, we show that these nanodroplets display a strong hyperCEST effect *in vitro*, and multiplex imaging can selectively activate nanodroplet or MB contrast.

CHAPTER 7: OUTLOOK AND FUTURE DIRECTIONS

Over the past 15 years, the collection of synthetic biosensors that reversibly bind xenon and produce hyperCEST contrast has continued to grow (183). As shown in this thesis, MB and nanodroplets can be added to this roster. In Chapter 4, MB were established as exceptionally efficiency hyperCEST agents that could produce contrast at 10s of fM, the lowest detection limit of a hyperCEST contrast agent to date. This is below the in-blood concentration used for clinical US imaging, allowing for dual-modal MR/US detection.

While some synthetic hyperCEST agents have been deemed biocompatible, currently, none of them are approved by the Food and Drug Administration for use in humans. As such, the demonstrated feasibility of using FDA-approved MB as a hyperCEST agent could greatly facilitate human translation of hyperCEST (170).

Chapter 5 presented the first *in vivo* hyperCEST experiments performed in mice using commercially-available CB[6]. We discussed the experimental requirements needed to obtain a reliable hyperCEST contrast *in vivo*. Specifically, these experiments highlighted the interplay between gas delivery, xenon accumulation in tissues, and MR acquisition in establishing a steady state magnetization.

Chapter 6 demonstrated the feasibility of low boiling point PFC nanodroplets as a dual-phase dual-modality contrast agent via hyperCEST. Since nanodroplets can be formulated by commercially-available MB, their translation to clinical use may not be too far behind (187; 193).

7.1 *In Vivo* Translation of MB-Mediated HyperCEST

Here, MB and nanodroplets were demonstrated to be very effective hyperCEST agents *in vitro*. As hyperCEST depends on chemical exchange rates, the *in vitro* behavior in PBS may not necessarily translate to the *in vivo* behavior in blood. Our experiments, along with results previously reported by others, suggest that this may indeed be the case. In the following paragraphs, the experimental difficulties with *in vivo* detection of MB and nanodroplets using hyperCEST are highlighted.

Chapter 5 outlines the work done to establish an optimal *in vivo* hyperCEST protocol using CB[6]. In our *in vivo* experiments, significant contrast was observed near the heart and the surrounding vasculature. The acquired Z-spectra also show an "apparent" hyperCEST effect obtained after on-resonance saturation of the gas-phase ^{129}Xe spins in the lungs. For these experiments, the volume coil was centered on the mouse's heart to ensure saturation of essentially the entire blood pool and the CB[6] in circulation.

For *in vivo* experiments with MB, saturation of the MB gas core inevitably led to direct saturation of the gas-phase spins in the lungs. In this case, the inability to resolve the gas-phase resonance of xenon in the MB core from the gas-phase resonance of xenon in the lungs prevented a clear identification of a possible hyperCEST effect originating from MB alone. The issue, although slightly reduced, was present also when the sensitive region of the transmit/detection coil was placed away from the lungs (Figure 7.1).

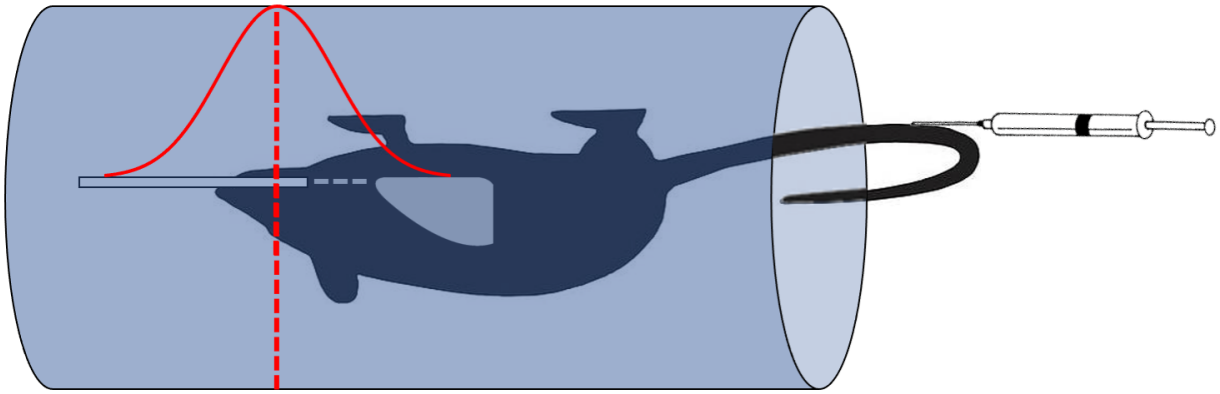

Figure 7.1: Positioning of mouse in volume coil for *in vivo* hyperCEST. Initial *in vivo* hyperCEST experiments with MB utilized a volume coil centered (red dotted line) on the brain of the mouse, partially affecting the ^{129}Xe gas-phase frequency in the ventilation tubing and the lungs. As a result, an apparent magnetization transfer effect is detected when saturating the gas-phase frequency.

Figure 7.2 shows the Z-spectra before and after a 100 μL bolus injection of a 2.5e10 MB/mL dose of MB, resulting in 1 pM in-blood concentration that is well within the detection limits (Table 4.1). A significant reduction of the dissolved-phase signal is observed for a saturation frequency near -200 ppm, even in absence of MB. This reduction is simply due to a saturation of the gas-phase in the lungs, which directly leads to a destruction of the spin polarization in the lung airspaces and to a consequent reduction of the observed dissolved phase signal. A volume coil is generally preferred when the signal is to be acquired from a large portion of the sample. Often referred to as a birdcage coils, these volume coils are commonly used for clinical MRI because they produce very uniform B_1. The center of coil is the most sensitive region,

and amplitude decreases away from the center of the coil along the z-axis (194). So even though the center of the volume was moved to the brain, this head-lung distance in the mouse was not big enough to move the lungs completely out of the sensitivity region of the coil.

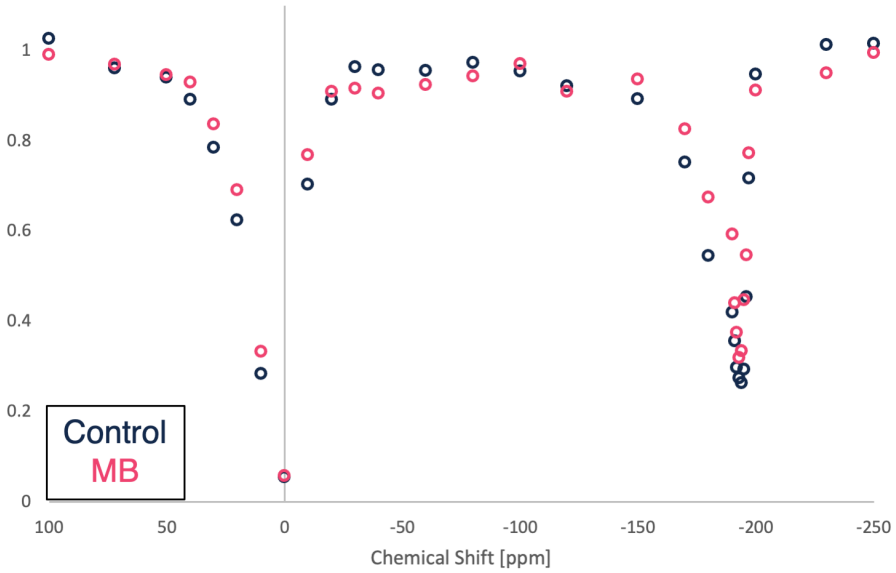

Figure 7.2: *In vivo* hyperCEST with and without MB in a mouse using a volume coil. A significant reduction of the dissolved-phase signal is noted after saturating gas-phase spins at -200 ppm, even in the absence of MB (Control). The large field inhomogeneity experienced by the gas-phase spins in the lungs does not allow for selective saturation of the gas core of the MB.

To clearly separate the hyperCEST effect due to gas MB, the volume coil was replaced with a surface coil. A surface coil is essentially a loop of wire whose sensitivity rapidly degrades with sample's distance from the coil. A surface coil is generally used to collect signal from a smaller region of the sample. To further minimize the spurious contribution of the gas-phase in the lungs, for our experiments, we used a surface coil centered on the rat brain (Figure 7.3).

Figure 7.4 shows Z-spectra before and after 700 μL bolus injection of a 2.5e10 MB/mL dose of MB, again resulting in 1 pM in-blood concentration. A reduction of the dissolved-phase signal is still present when saturating the gas-phase resonance even in absence of gas MB. For these experiments, the rat was orally intubated and ventilated with HP ^{129}Xe. The supine positioning of the rat placed the intratracheal tube away from the surface coil, but not far enough for the spins to be completely unaffected by the saturation pulse. When MB were used, we observed only a very small increase in hyperCEST contrast. Based on the *in vitro* results, the in-blood MB concentration used here should have produced a significantly greater

Figure 7.3: Positioning of surface coil for *in vivo* hyperCEST. In order to avoid a contribution from the large gas-phase reservoir in the lungs, a surface coil was centered on the brain of a rat. A surface coil collects localized signal, and its B_1 decreases with depth (red). In this case a small spurious contribution originated from the intratracheal tube used to deliver the HP gas to the mouse.

signal loss, which we did not observe. Further experiments may be conducted by centering the surface coil on the kidney, a highly perfused organ that is located far away from the lungs as well as the gas delivery tubing.

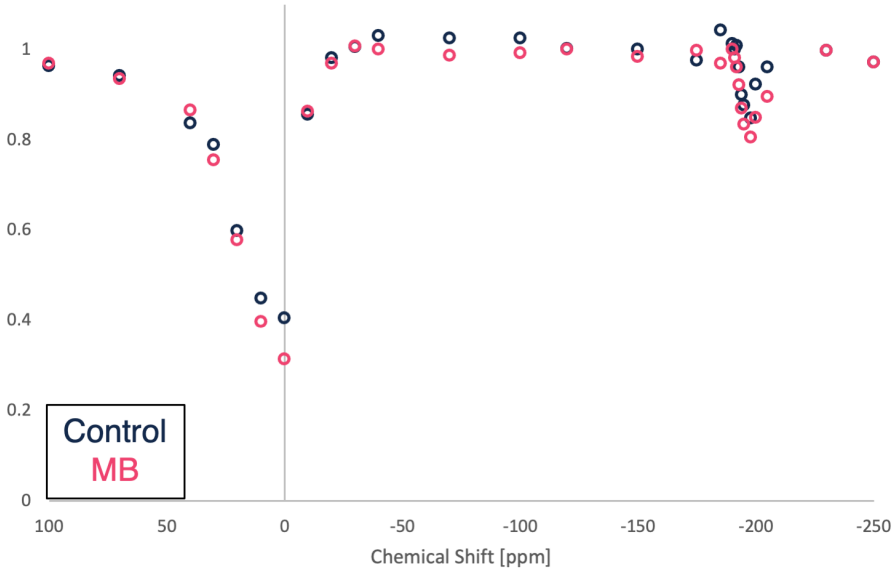

Figure 7.4: *In vivo* hyperCEST detection of gas MB in a rat using a surface coil centered on the head of the rat. The spurious gas-phase response decreased when using a small surface coil placed away from the lungs, but still remained present. This is puzzling because MB should produce significant hyperCEST contrast at this concentration. The data shown here was collected with the center frequency slightly off-resonance from the dissolved-phase signal, explaining why there is not complete saturation at 0 ppm.

In Chapter 6, nanodroplets were used in an attempt to separate the carrier frequency from the gas-phase frequency. Figure 6.3A showed that nanodroplets produced a large hyperCEST effect at -135 ppm, which was also demonstrated with hyperCEST imaging (Figure 6.5C). The chemical shift of xenon in the nanodroplets core was expected to be well separated from the gas-phase peak that prevented the detection of hyperCEST contrast from gas MB *in vivo* (Figure 7.1). Figure 7.5 shows Z-spectra before and after a 200 μL bolus injection of 10^{11} nanodroplets/mL and 10^{12} nanodroplets/mL. Unfortunately, the gas-phase valley was still too broad to clearly identify a hyperCEST effect near the -135 ppm frequency (blue line). The experiment with the 10x higher concentration (grey, resulting in an in-blood concentration of 100 pM) showed an asymmetry of the gas-phase valley that suggests a possible hyperCEST effect from the nanodroplets. A formal magnetization transfer ratio asymmetry could potentially be used to separate the signal, but there is also an unreliable variability in the valley shape which is troublesome. Future experiments would benefit from the surface coil setup since -135 ppm is very clearly separated from the gas-phase valley shown in Figure 7.4. One should note that this *in vivo* experiment was performed by using the same *in vitro* concentration used for the experiment shown in Figure 6.3A. Yet, if nanodroplets were present, the hyperCEST effect obtained *in vivo* is still nowhere near the one obtained *in vitro*. This could be attributed a different exchange dynamic in blood.

The fact that neither the MB nor the nanodroplets performed as optimally as they did *in vitro* also suggest that there may be hinderance involved with chemical exchange in blood. Previous work suggest that this may be the case. When PFOB nanodroplets were first explore by Wolber et al. as carriers of HP ^{129}Xe, they noticed that the NMR linewidth of the nanodroplet signal varied with nanodroplet size (115). They acknowledged the possibility of magnetic susceptibility affecting the linewidth, similar to the phenomenon discussed in Chapter 6. Instead, they hypothesized that the observed line broadening was the result of chemical exchange of xenon in and out the nanodroplet core. They also injected pre-loaded PFOB into a rat, which led to the detection of a single very large and very narrow peak corresponding to ^{129}Xe in the nanodroplets core. A year later, a similar spectrum was published by Venkatesh et al. (195). In both cases only a single peak was detected, indicating that ^{129}Xe inside the nanodroplet core did not exchange with blood or tissues, as that would have resulted in the presence of additional peaks in the spectra. Another experiment involved replacing 50% of a rat's blood volume with a nanodroplet solution and ventilating the animal with HP ^{129}Xe. In this scenario, the peaks corresponding to RBC and plasma were detected in the spectra, but there was no trace of a resonance from xenon inside the nanodroplets. Taken together these

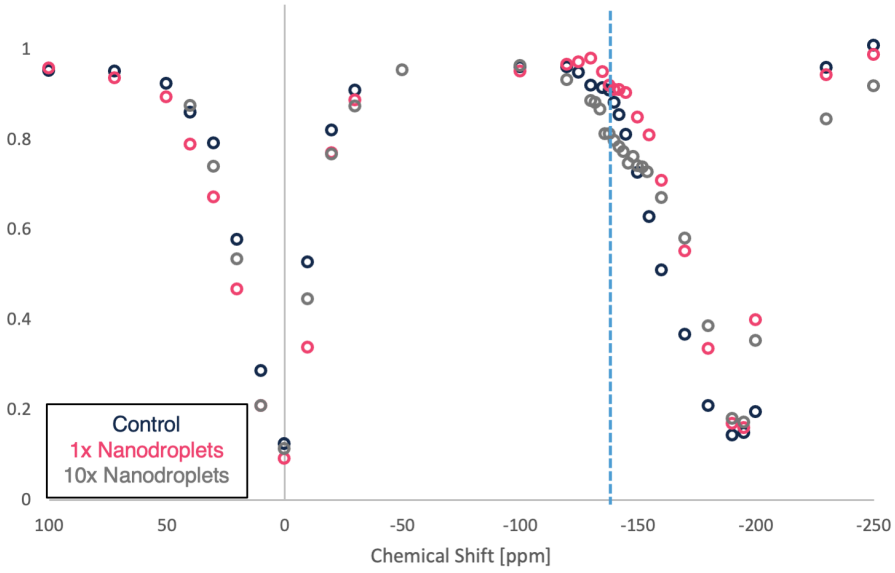

Figure 7.5: *In vivo* Z-spectra from DFB nanodroplets in a mouse using a volume coil. The chemical shift of nanodroplets (-135 ppm, blue dotted line) should be separated from the gas-phase signal in the lungs. Because of the much larger field inhomogeneity experienced by the gas-phase resonance in the lungs, the gas-phase valley appears too broad and asymmetrical to quantify the nanodroplet effect. The use of the surface coil setup in this case may provide better separation between the nanodroplets and the gas phase resonances.

results can only be explained by a complete or greatly reduced xenon exchange between the nanodroplets and blood. Of course, further experiments will be needed to confirm this hypothesis.

As demonstrated in Chapter 5, there is no problem with *in vivo* hyperCEST using CB[6], which could be due to how xenon is bound to these different carriers. The majority of work done in the field of hyperCEST have been limited to *in vitro*, aqueous environments. More work must be done to better understand the properties of hyperCEST in blood. Using blood as solvent for *in vitro* experiments is experimentally difficult because the delivery method of bubbling HP ^{129}Xe creates large amounts of foam which is difficult to control and contain (144; 196).

Evidently, if ^{129}Xe is pre-loaded into a PFC, it is likely to remain within the carrier molecule while in blood. This may not be ideal for hyperCEST, but it serves its purpose as a transporter for targeted release. If PFC nanodroplets are capable of carrying large amounts of HP ^{129}Xe, preserving their magnetization (195), targeted delivery of HP ^{129}Xe still remains of interest. Injecting and delivering ^{129}Xe in this manner could find niche applications *in vivo*.

7.2 MB as MR Theranostic Agent

The theranostic quality of MB and nanodroplets is defined by their ability to provide diagnostic US image contrast and deliver therapeutic gases. In the realm of MRI, MB and nanodroplets could also serve these purposes, extending their theranostic ability across imaging modalities. MB and nanodroplets have been used for US-mediated therapy treatments where the delivery of oxygen can reverse tumor hypoxia to better facilitate diagnosis and treatment (60; 69). The same utility has been suggested with the delivery of HP ^{129}Xe (115). With the delivery of HP ^{129}Xe to regions such as BAT, the spin density would increase locally thus increasing the signal contrast. It was also shown that having HP ^{129}Xe transported in a carrier can help prolong T_1 to maintain magnetization (195). After targeted delivery, MR imaging and spectroscopy could then be used to detect the tissues and compartments in which xenon dissolves.

7.3 MB as MR pressure Probe

Another interesting path to pursue would be to characterize the pressure-dependence of the hyperCEST contrast provided by MB. As shown in Figure 4.6, MB perturb the local external magnetic field due to the difference in susceptibility between the gas core and the solvent. The size of the susceptibility field depends on the MB size, which is governed by the Laplace pressure. Since the field inhomogeneity influences T_2^*-contrast, MB could in principle be used as a pressure-sensitive MR-probe (197; 198). This can be particularly useful for noninvasively detecting abnormalities of intravascular pressure such as pulmonary hypertension. While simulations have shown that in order to produce enough contrast for this application, MB must be doped with SPIONs (199), hyperCEST may allow for detection of MB size without the need of exogenous paramagnetic particles. Kunth et al. introduced the concept of an "elastic" hyperCEST contrast agent when they observed that hyperCEST efficiency of GV increased with pressure (110). At a fixed concentration, GV would accommodate more xenon atoms and increase the gas turnover rate pet host. This suggests that elastic hyperCEST is also a pressure-sensitive detection method. They saw that the filling of GV with xenon followed the Ideal Gas Law, indicating that GV are fairly rigid and maintain their volumes and, consequently, their exchange rates (200). As MB-diameter responds to the applied pressure, the exchange rate is also affected (Figure 4.1). The hyperCEST response of MB as a function of pressure would be an interesting idea to pursue as exchange rate efficiency diminishes as MB size deviates from 2 μm (Figure 4.8F).

7.4 Effect of Gas Environment on Microbubble Size

The size and gas contents of a MB are extremely sensitive to the surrounding environment. Changes in the partial pressures cause gases to rush in or out of the MB as it adjusts to establish equilibrium. In order to model the gas contents of a MB, dissolution was simulated by considering only pure diffusion of different gas species in and out of the MB. This model of gas diffusion for multiple species recursively outputs the MB radius (R) as well as number of moles (n) of each gas species (i) over time (173; 174; 175).

$$n_i^{\tau+1} = -4\pi h R D_i K_{H,i} \left[\frac{2\sigma}{R} - P_{\infty,i}\alpha_i + P_H - \frac{3BT}{4\pi R^3} \sum_{j=1}^{N} n_j \right] + n_i^{\tau}, j \neq i$$

$$0 = \frac{8\pi\sigma}{3BT}(R^{\tau+1})^2 + \frac{4\pi P_H}{3BT}(R^{\tau+1})^3 - \sum_{i=1}^{N} n_i^{\tau+1} \tag{7.1}$$

$$h = \frac{R^2}{4D_{min}}$$

D is the diffusion coefficient, K_H is the Henry's constant, B is the ideal gas constant, and T is the temperature. The dynamic timestep h is based on the slowest dissolving gas.

Simulations were used to model the diffusion of three gases: PFOB, N_2, and ^{129}Xe. All relevant parameters are listed in Table 7.1. The MB surface tension (σ) was set to 0 mN m^{-1} (175), the temperature was set to 310 K, the hydrostatic pressure (P_H) was set to the sum over all P_∞ (the partial pressures far away from the MB). α_i represents the degree of dissolved-gas saturation where 1 is considered fully saturated. When determining the subsequent MB radius, the Newton-Raphson method was used for 100 iterations.

	$D \times 10^{10}$ [m^2 s^{-1}]	$K_H \times 10^8$ [mol m^3 Pa^{-1}]	P_∞ [atm]
PFOB	6.9	1.4797	0
N_2	20	640	0.25
^{129}Xe	19.5	4400	0.75

Table 7.1: The diffusion coefficient (D), Henry's Constant (K_H)), and partial pressure at saturation ($P_{\infty,i}$) for each gas in the MB dissolution simulation are shown. The MB were initially filled with PFOB. Fresh HP ^{129}Xe was delivered in a mixture with N_2 (75%:25%). When calculating their respective P_∞, it was assumed that the sample was completely degassed of O_2, and it was in equilibrium with atmospheric pressure. Simulations were run at $\alpha_{N_2,^{129}Xe}$=1 and $\alpha_{N_2,^{129}Xe}$=0.98.

Figure 7.6 shows the MB dissolution simulations for (A) a fully saturated ($\alpha_{N_2,^{129}Xe}$=1) solution and (B) an undersaturated ($\alpha_{N_2,^{129}Xe}$=0.98) solution. At full saturation, the MB diameter and gas contents all approach a steady state over time. But, even with a modest 2% decrease in the dissolved gases, there is a steady decline in the MB size and gas contents as ^{129}Xe exchanges into solution.

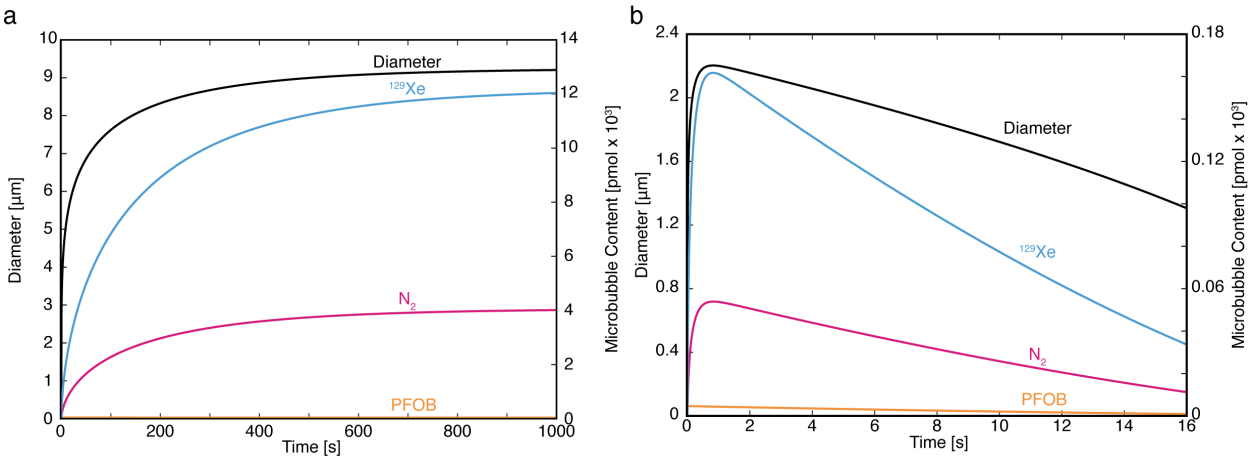

Figure 7.6: *In vitro* MB dissolution simulations. MB growth and gas contents were simulated based on experiment parameters listed in Table 1. The initial diameter was 0.4 microns. Growth for MB with zero surface tension is driven by the degree of saturation of the dissolved gases. At $\alpha_{N_2,^{129}Xe}$=1 (a), the MB diameter grows by a factor of 20. At $\alpha_{N_2,^{129}Xe}$=0.98 (b), the MB diameter grows by a factor of 5.5. MB growth is very sensitive to α_i, and this parameter needs to be monitored in future experiments.

REFERENCES

[1] Scatliff, J. & Morris, P. From röntgen to magnetic resonance imaging. *N. C. Med. J* **75**, 111–113.

[2] Bercovich, E. & Javitt, M. Medical imaging: From roentgen to the digital revolution, and beyond. *Rambam Maimonides Med. J* **9**, 0034.

[3] Bradley, W. History of medical imaging. *Proc. Am. Philos. Soc* **152**, 349–361.

[4] Badash, L. Marie curie: In the laboratory and on the battlefield. *Phys. Today* **56**, 37.

[5] The nobel prize in physics 1901 - nobelprize.org. URL `https://www.nobelprize.org/prizes/physics/1901/summary/`.

[6] Gillanders, I. The roentgen rays in bullet extraction. *Br. Med. J* **1**, 1252–1253.

[7] Webb, A. *Introduction to Biomedical Imaging* (Wiley-IEEE Press).

[8] The nobel prize in physiology or medicine 1979. URL `https://www.nobelprize.org/prizes/medicine/1979/summary/`.

[9] Bouma, G. Ultra-early evaluation of regional cerebral blood flow in severely head-injured patients using xenon-enhanced computerized tomography. *J. Neurosurg* **77**, 360–368.

[10] Branca, R. Accurate quantification of brown adipose tissue mass by xenon-enhanced computed tomography. *Proc. Natl. Acad. Sci. U. S. A* **115**, 174–179.

[11] Antonacci, M. Direct detection of brown adipose tissue thermogenesis in ucp1/ mice by hyperpolarized 129xe mr thermometry. *Sci. Rep* **9**.

[12] Mukherjee, J., Baranwal, A., Schade, N. & K. Classification of therapeutic and experimental drugs for brown adipose tissue activation: Potential treatment strategies for diabetes and obesity. *Curr. Diabetes Rev* **12**, 414–428.

[13] Sampath, S., Sampath, S., Bredella, M., Cypess, A. & Torriani, M. Imaging of brown adipose tissue: State of the art. *Radiology* **280**, 4–19.

[14] Cypess, A., Haft, C., Laughlin, M. & Hu, H. Brown fat in humans: Consensus points and experimental guidelines. *Cell Metab* **20**, 408–415.

[15] Cannon, B. & Nedergaard, J. Brown adipose tissue: function and physiological significance. *Physiol. Rev* .

[16] Cypess, A. Identification and importance of brown adipose tissue in adult humans. *N. Engl. J. Med* **360**, 1509–1517.

[17] Thornton, S. & Rex, A. *Modern Physics for Scientists and Engineers* (Cengage Learning).

[18] McHugh, C., Raynor, W., Werner, T., Alavi, A. & Rajapakse, C. Feasibility of quantifying bone metabolism in the femoral neck in human subjects using multi-modality imaging. In *Proceedings of the International Society of Magnetic Resonance in Medicine*.

[19] Austin, A., Austin, A., Raynor, W., Reilly, C. & Zadeh, M. Evolving role of mr imaging and pet in assessing osteoporosis. *PET Clin* **14**, 31–41.

[20] Weber, W. Assessing tumor response to therapy. *Journal of Nuclear Medicine* **50**.

[21] Beyer, T. A combined pet/ct scanner for clinical oncology. *J. Nucl. Med* **41**.

[22] Townsend, D. Combined positron emission tomography-computed tomography: the historical perspective. semin. ultrasound, ct. *MRI* **29**, 232–235.

[23] Stammes, M. Medical imaging of pulmonary disease in sars-cov-2-exposed non-human primates. *Trends Mol. Med* **28**, 123–142.

[24] Finch, C. Characteristic and quantifiable covid-19-like abnormalities in ct- and pet/ct-imaged lungs of sars-cov-2-infected crab-eating macaques (macaca fascicularis. *bioRxiv* .

[25] Hartman, A. Sars-cov-2 infection of african green monkeys results in mild respiratory disease discernible by pet/ct imaging and shedding of infectious virus from both respiratory and gastrointestinal tracts. *PLOS Pathog* **16, e1008903**.

[26] Böszörményi, K. The post-acute phase of sars-cov-2 infection in two macaque species is associated with signs of ongoing virus replication and pathology in pulmonary and extrapulmonary tissues. *Viruses* **13**, 1673 13,.

[27] Arunachalam, P. Adjuvanting a subunit covid-19 vaccine to induce protective immunity. *Nat* **5947862 594**, 253–258.

[28] Inokuma, K. Uncoupling protein 1 is necessary for norepinephrine-induced glucose utilization in brown adipose tissue. *Diabetes* **54**, 1385–1391.

[29] Jeanguillaume, C. Visualization of activated bat in mice, with fdg-pet and its relation to ucp1. *Adv. Mol. Imaging* .

[30] Hankir, M. Dissociation between brown adipose tissue 18 f-fdg uptake and thermogenesis in uncoupling protein 1 deficient mice. *J. Nucl. Med* **116**.

[31] Olsen, J. 3-adrenergically induced glucose uptake in brown adipose tissue is independent of ucp1 presence or activity: Mediation through the mtor pathway. *Mol. Metab* .

[32] McHugh, C. Differences in [18f]fdg uptake in bat of ucp1 / and ucp1 +/+ during adrenergic stimulation of non-shivering thermogenesis. *EJNMMI Res* **10**, 136.

[33] Leitner, B. Mapping of human brown adipose tissue in lean and obese young men. *Proc. Natl. Acad. Sci* **114**, 8649–8654.

[34] Blondin, D. Selective impairment of glucose but not fatty acid or oxidative metabolism in brown adipose tissue of subjects with type 2 diabetes. *Diabetes* **64**, 2388–2397.

[35] McCallister, A., Zhang, L., Burant, A., Katz, L. & Branca, R. A pilot study on the correlation between fat fraction values and glucose uptake values in supraclavicular fat by simultaneous pet/mri. *Magn. Reson. Med* **78**.

[36] Hankir, M. & Klingenspor, M. Brown adipocyte glucose metabolism: a heated subject. *EMBO Rep* **19**, 46404.

[37] Carpentier, A. Brown adipose tissue energy metabolism in humans. *Frontiers in Endocrinology* **9**.

[38] Golozoubova, V., Cannon, B. & Nedergaard, J. Ucp1 is essential for adaptive adrenergic nonshivering thermogenesis. URL `http://www.ajpendo.org`.

[39] Shimizu, Y. Effects of noradrenaline on the cell-surface glucose transporters in cultured brown adipocytes: Novel mechanism for selective activation of glut1 glucose transporters. *Biochem. J* **330**, 397–403.

[40] Raylman, R. *Reduction of positron range effects by the application of a magnetic field: For use with positron emission tomography. ProQuest Dissertations and Theses* (University of Michigan).

[41] Raylman, R., Hammer, B. & Christensen, N. Combined mri-pet scanner: a monte carlo evaluation of the improvements in pet resolution due to the effects of a static homogeneous magnetic field. *IEEE Trans. Nucl. Sci* **43**, 2406–2412.

[42] Brown, R., Cheng, Y., Haacke, E., Thompson, M. & Venkatesan, R. Magnetic resonance imaging: Physical principles and sequence design: Second edition. *Magn. Reson. Imaging Phys. Princ. Seq. Des. Second Ed* **9780471720**, 1–944.

[43] Schröder, L., Lowery, T., Hilty, C., Wemmer, D. & Pines, A. Molecular imaging using a targeted magnetic resonance hyperpolarized biosensor. *Science* **80-.). 314**, 446–449.

[44] The nobel prize in physics 1944 - nobelprize.org. URL `https://www.nobelprize.org/prizes/physics/1944/summary/.`

[45] The nobel prize in physiology or medicine 2003 - nobelprize.org. URL `https://www.nobelprize.org/prizes/medicine/2003/summary/.`

[46] Branca, R. Detection of brown adipose tissue and thermogenic activity in mice by hyperpolarized xenon mri. *Proc. Natl. Acad. Sci* **111**, 18001–18006.

[47] Branca, R., Zhang, L., Burant1, A., Katz, L. & McCallister, A. Detection of human brown adipose tissue by mri with hyperpolarized xe-129 gas and validation by fdg-pet/mri. In *International Society of Magnetic Resonance in Medicine 1054*.

[48] Zhang, L. Accurate mr thermometry by hyperpolarized 129 xe. *Magn. Reson. Med* **78**, 1070–1079.

[49] Antonacci, M., Zhang, L., Degan, S., Erdmann, D. & Branca, R. Calibration of methylene-referenced lipid-dissolved xenon frequency for absolute mr temperature measurements. *Magn. Reson. Med* **81**, 765–772.

[50] Bernstein, M., King, K. & Zhou, X. *Handbook of MRI Pulse Sequences* (Elsevier Science Technology).

[51] Ogawa, T. S. Lee. Magnetic resonance imaging of blood vessels at high fields: In vivo and in vitro measurements and image simulation. *Magn. Reson. Med* **16**, 9–18.

[52] Oxygenation-sensitive contrast in magnetic resonance image of rodent brain at high magnetic fields. *Magn. Reson. Med* **14**, 68–78.

[53] Ogawa, S., Lee, T., Kay, A. & Tank, D. Brain magnetic resonance imaging with contrast dependent on blood oxygenation. *Proc. Natl. Acad. Sci* **87**, 9868–9872.

[54] Khanna, A. & Branca, R. Detecting brown adipose tissue activity with bold mri in mice. *Magn. Reson. Med* **68**, 1285–1290.

[55] Lee, J. Artificially engineered magnetic nanoparticles for ultra-sensitive molecular imaging. *Nat. Med* **13**, 95–99.

[56] Pankhurst, Q., Connolly, J., Jones, S. & Dobson, J. Applications of magnetic nanoparticles in biomedicine. *J. Phys. D. Appl. Phys* **36, R167**.

[57] Valdiglesias, V. Effects of iron oxide nanoparticles: Cytotoxicity, genotoxicity, developmental toxicity, and neurotoxicity. *Environ. Mol. Mutagen* **56**, 125–148.

[58] Valdiglesias, V. Are iron oxide nanoparticles safe? current knowledge and future perspectives. *J. Trace Elem. Med. Biol* **38**, 53–63.

[59] Senyei, A., Widder, K. & Czerlinski, G. Magnetic guidance of drug-carrying microspheres. *J. Appl. Phys* **49**, 3578.

[60] Fix, S., Borden, M. & Dayton, P. Therapeutic gas delivery via microbubbles and liposomes. *J. Control. Release* **209**, 139–149.

[61] Yang, F. Superparamagnetic iron oxide nanoparticle-embedded encapsulated microbubbles as dual contrast agents of magnetic resonance and ultrasound imaging. *Biomaterials* **30**, 3882–3890.

[62] Dayton, P. & Rychak, J. Molecular ultrasound imaging using microbubble contrast agents. *Frontiers in Bioscience* .

[63] Gessner, R. & Dayton, P. Advances in molecular imaging with ultrasound. *Mol. Imaging* **9**, 117–127.

[64] Abou-Elkacem, L., Bachawal, S. & Willmann, J. Ultrasound molecular imaging: Moving toward clinical translation. *Eur. J. Radiol* **84**, 1685–1693.

[65] Quaia, E. Classification and safety of microbubble-based contrast agents. In *Contrast Media in Ultrasonography*, 3–14.

[66] Flynn, A. Contrast-enhanced ultrasound: A novel noninvasive, nonionizing method for the detection of brown adipose tissue in humans. *J. Am. Soc. Echocardiogr* **28**, 1247–1254.

[67] Cosgrove, D. Ultrasound contrast agents: An overview. *Eur. J. Radiol* **60**, 324–330.

[68] Ohlerth, S. & O'Brien, R. Contrast ultrasound: General principles and veterinary clinical applications. *Vet. J* **174**, 501–512.

[69] Kwan, J., Kaya, M., Borden, M. & Dayton, P. Theranostic oxygen delivery using ultrasound and microbubbles. *Theranostics* **2**, 1174–1184.

[70] Tong, J. Mesenchymal stem cell transplantation enhancement in myocardial infarction rat model under ultrasound combined with nitric oxide microbubbles. *PLoS One* **8, e80186**.

[71] Ma, D. Neuroprotective and neurotoxic properties of the 'inert' gas, xenon. *Br. J. Anaesth* **89**, 739–746.

[72] Kelkar, S. & Reineke, T. Theranostics: Combining imaging and therapy. *Bioconjug. Chem* **22**, 1879–1903.

[73] Svenson, S. Theranostics: Are we there yet? mol. *Pharm* **10**, 848–856.

[74] Solvay institutes. URL http://www.solvayinstitutes.be/html/solvayconference.html.

[75] de Physique, C. *Rapports et discussions du cinquième Conseil de physique tenu à Bruxelles du 24 au 29 octobre 1927 sous les auspices de l'Institut international de physique Solvay* (Gauthier-Villars et cie, Paris).

[76] Pais, A. George uhlenbeck and the discovery of electron spin. *Phys. Today* **42**, 34.

[77] Goudsmit on the discovery of electron spin. URL https://www.lorentz.leidenuniv.nl/history/spin/goudsmit.html.

[78] Pauli, W. & In, H. Über den zusammenhang des abschlusses der elektronengruppen im atom mit der komplexstruktur der spektren. *Zeitschrift für Phys* **311 31**, 765–783.

[79] Uhlenbeck, G. & Goudsmit, S. Spinning electrons and the structure of spectra. *Nat* **1172938 117**, 264–265.

[80] The nobel prize in physics 1952 - nobelprize.org. URL https://www.nobelprize.org/prizes/physics/1952/summary/.

[81] The nobel prize in chemistry 2002 - nobelprize.org. URL https://www.nobelprize.org/prizes/chemistry/2002/summary/.

[82] The nobel prize in chemistry 1991 - nobelprize.org. URL https://www.nobelprize.org/prizes/chemistry/1991/summary/.

[83] Levitt, M. *Spin Dynamics : Basics of Nuclear Magnetic Resonance* (John Wiley Sons, Ltd).

[84] Rabi, I., Zacharias, J., Millman, S. & Kusch, P. A new method of measuring nuclear magnetic moment. *Phys. Rev* **53**, 318.

[85] Bain, A. Operator formalisms: An overview. *Concepts Magn. Reson. Part A* **28A**, 369–383.

[86] Sakurai 1933-1982, S. F., J. J. (Jun J. Tuan 1932. *Modern quantum mechanics* (Addison-Wesley Pub. Co, Reading, Mass).

[87] Nikolaou, P., Goodson, B. & Chekmenev, E. Nmr hyperpolarization techniques for biomedicine. *Chem. – A Eur. J* **21**, 3156–3166.

[88] Ardenkjær-Larsen, J. Increase in signal-to-noise ratio of gt; 10,000 times in liquid-state nmr. *Proc. Natl. Acad. Sci* **100**, 10158–10163.

[89] Eisenschmid, T. Para hydrogen induced polarization in hydrogenation reactions. *J. Am. Chem. Soc* **109**, 8089–8091.

[90] Walker, T. & Happer, W. Spin-exchange optical pumping of noble-gas nuclei. *Rev. Mod. Phys* **69**, 629–642.

[91] Freeman, M., Emami, K. & Driehuys, B. Characterizing and modeling the efficiency limits in large-scale production of hyperpolarized xe 129. *Phys. Rev. A - At. Mol. Opt. Phys* **90**, 023406.

[92] Nikolaou, P. Near-unity nuclear polarization with an open-source 129xe hyperpolarizer for nmr and mri. *Proc. Natl. Acad. Sci* **110**, 14150–14155.

[93] Happer, W. Optical pumping. *Rev. Mod. Phys* **44**, 169.

[94] Driehuys, B. High-volume production of laser-polarized 129xe. *Appl. Phys. Lett* **69**, 1668.

[95] He, M. Dose and pulse sequence considerations for hyperpolarized 129xe ventilation mri. *Magn. Reson. Imaging* **33**, 877–885.

[96] Schrank, G., Ma, Z., Schoeck, A. & Saam, B. Characterization of a low-pressure high-capacity x 129 e flow-through polarizer. *Phys. Rev. A - At. Mol. Opt. Phys* **80**, 063424.

[97] McHugh, C., Kelley, M., Bryden, N. & Branca, R. In vivo hypercest imaging: Experimental considerations for a reliable contrast. *Magn. Reson. Med* .

[98] Kelley, M. & Branca, R. Theoretical models of spin-exchange optical pumping: Revisited and reconciled. *J. Appl. Phys* **129**, 154901.

[99] Kelley, M., Burant, A. & Branca, R. Resolving the discrepancy between theoretical and experimental polarization of hyperpolarized 129xe using numerical simulations and in situ optical spectroscopy. *J. Appl. Phys* **128**, 144901.

[100] Bloch, F. Nuclear induction. *Phys. Rev* **70**, 460.

[101] McConnell, H. Reaction rates by nuclear magnetic resonance. *J. Chem. Phys* **28**, 430.

[102] Pietraiß, T. & Gaede, H. Optically polarized129xe in nmr spectroscopy. *Adv. Mater* **7**, 826–838.

[103] Schröder, L. Xenon for nmr biosensing–inert but alert. *Phys. Med* **29**, 3–16.

[104] Ernst, R. & Anderson, W. Application of fourier transform spectroscopy to magnetic resonance. *Rev. Sci. Instrum* **37**, 93.

[105] Richard, R. Ernst - biographical - nobelprize.org. URL `https://www.nobelprize.org/prizes/chemistry/1991/ernst/biographical/`.

[106] Antonacci, M., Zhang, L., Burant, A., McCallister, D. & Branca, R. Simple and robust referencing system enables identification of dissolved-phase xenon spectral frequencies. *Magn. Reson. Med* **80**, 431–441.

[107] Bain, A. Chemical exchange in nmr. *Progress in Nuclear Magnetic Resonance Spectroscopy* **43**, 63–103.

[108] Jayapaul, J., Schröder, L. & Pimentel-Coelho, P. Nanoparticle-based contrast agents for 129xe hypercest nmr and mri applications. *Contrast Media and Molecular Imaging* **2019**.

[109] Klippel, S., Freund, C. & Schröder, L. Multichannel mri labeling of mammalian cells by switchable nanocarriers for hyperpolarized xenon. *Nano Lett* **14**, 5721–5726.

[110] Kunth, M., Lu, G., Witte, C., Shapiro, M. & Schröder, L. Protein nanostructures produce self-adjusting hyperpolarized magnetic resonance imaging contrast through physical gas partitioning. *ACS Nano* **12**, 10939–10948.

[111] McHugh, C., Durham, P., Kelley, M., Dayton, P. & Branca, R. Magnetic resonance detection of gas microbubbles via hypercest: A path toward dual modality contrast agent. *ChemPhysChem* **22**, 1219–1228.

[112] Kunth, M., Witte, C. & Schröder, L. Quantitative chemical exchange saturation transfer with hyperpolarized nuclei (qhyper-cest): Sensing xenon-host exchange dynamics and binding affinities by nmr. *J. Chem. Phys* **141**, 194202.

[113] Lippens, G., Caron, L. & Smet, C. A microscopic view of chemical exchange: Monte carlo simulation of molecular association. *Concepts Magn. Reson. Part A Bridg. Educ. Res* **21**, 1–9.

[114] Woods, M., Woessner, D. & Sherry, A. Paramagnetic lanthanide complexes as paracest agents for medical imaging. *Chem. Soc. Rev* **35**, 500–511.

[115] Wolber, J., Rowland, I., Leach, M. & Bifone, A. Perfluorocarbon emulsions as intravenous delivery media for hyperpolarized xenon. *Magn. Reson. Med* **41**, 442–449.

[116] Stevens, T., Ramirez, R. & Pines, A. Nanoemulsion contrast agents with sub-picomolar sensitivity for xenon nmr. *J. Am. Chem. Soc* **135**, 9576–9579.

[117] Zijl, P. & Yadav, N. Chemical exchange saturation transfer (cest): what is in a name and what isn't? magn. *Reson. Med* **65**, 927–948.

[118] Shapiro, M. Genetically encoded reporters for hyperpolarized xenon magnetic resonance imaging. *Nat. Chem* **6**, 629–634.

[119] Sherry, A. & Woods, M. Chemical exchange saturation transfer contrast agents for magnetic resonance imaging. *Annu. Rev. Biomed. Eng* **10**, 391–411.

[120] Zaiss, M., Schnurr, M. & Bachert, P. Analytical solution for the depolarization of hyperpolarized nuclei by chemical exchange saturation transfer between free and encapsulated xenon (hypercest. *J. Chem. Phys* **136**, 144106.

[121] Lee, J.-S. & Khitrin, A. Nmr quantum toys. *Concepts Magn. Reson. Part A* **30A**, 194–217.

[122] Kunth, M., Witte, C. & Schröder, L. Continuous-wave saturation considerations for efficient xenon depolarization. *NMR Biomed* **28**, 601–606.

[123] Hane, F. In vivo detection of cucurbit[6]uril, a hyperpolarized xenon contrast agent for a xenon magnetic resonance imaging biosensor. *Sci. Rep* **7**, 1–7.

[124] Zhou, J., Lal, B., Wilson, D., Laterra, J. & Van Zijl, P. P. T. Contrast for imaging of brain tumors. *Magn. Reson. Med* **50**, 1120–1126.

[125] Zhou, J. Differentiation between glioma and radiation necrosis using molecular magnetic resonance imaging of endogenous proteins and peptides. *Nat. Med* **17**, 130–134.

[126] Zhao, X. Three-dimensional turbo-spin-echo amide proton transfer mr imaging at 3-tesla and its application to high-grade human brain tumors. *Mol. Imaging Biol* **15**, 114–122.

[127] Park, J., Kim, H., Park, K., Choi, C. & Kim, S. Histogram analysis of amide proton transfer imaging to identify contrast-enhancing low-grade brain tumor that mimics high-grade tumor: Increased accuracy of mr perfusion1. *Radiology* **277**, 151–161.

[128] Dula, A. Amide proton transfer imaging of the breast at 3 t: Establishing reproducibility and possible feasibility assessing chemotherapy response. *Magn. Reson. Med* **70**, 216–224.

[129] Donahue, M. Assessment of lymphatic impairment and interstitial protein accumulation in patients with breast cancer treatment-related lymphedema using cest mri. *Magn. Reson. Med* **75**, 345–355.

[130] Jia, G. Amide proton transfer mr imaging of prostate cancer: A preliminary study. *J. Magn. Reson. Imaging* **33**, 647–654.

[131] Cai, K. Characterizing prostate tumor mouse xenografts with cest and mt-mri and redox scanning. *Advances in Experimental Medicine and Biology* **765 39–45**.

[132] Klippel, S. Cell tracking with caged xenon: Using cryptophanes as mri reporters upon cellular internalization. *Angew. Chemie Int. Ed* **53**, 493–496.

[133] Brotin, T. & Dutasta, J. Cryptophanes and their complexes - present and future. *Chem. Rev* **109**, 88–130.

[134] Fernando, P. Decacationic pillar[5]arene: A new scaffold for the development of 129xe mri imaging agents. *ACS Omega* **5**, 27783–27788.

[135] Wang, Y. & Dmochowski, I. Cucurbit[6]uril is an ultrasensitive 129 xe nmr contrast agent. *Chem. Commun* **51**, 8982–8985.

[136] Korchak, S., Riemer, T., Kilian, W. & Mitschang, L. Quantitative biosensor detection by chemically exchanging hyperpolarized 129xe. *Phys. Chem. Chem. Phys* **20**, 1800–1808.

[137] Stevens, T. Hypercest detection of a 129xe-based contrast agent composed of cryptophane-a molecular cages on a bacteriophage scaffold. *Magn. Reson. Med* **69**, 1245–1252.

[138] Spence, M. Functionalized xenon as a biosensor. *Proc. Natl. Acad. Sci. U. S. A* **98**, 10654–10657.

[139] Chen, H. Developmental and organ-specific toxicity of cucurbit[7]uril: In vivo study on zebrafish models. *RSC Adv* **5**, 30067–30074.

[140] Liu, H. A sample preparation technique using biocompatible composites for biomedical applications. *Molecules* **24**, 1321.

[141] Kim, J. Carbohydrate wheels: Cucurbituril-based carbohydrate clusters. *Angew. Chemie Int. Ed* **46**, 7393–7395.

[142] Walker, S., Kaur, R., McInnes, F. & Wheate, N. Synthesis, processing and solid state excipient interactions of cucurbit[6]uril and its formulation into tablets for oral drug delivery. *Mol. Pharm* **7**, 2166–2172.

[143] Kunth, M., Witte, C., Hennig, A. & Schröder, L. Identification, classification, and signal amplification capabilities of high-turnover gas binding hosts in ultra-sensitive nmr. *Chem. Sci* **6**, 6069–6075.

[144] Hane, F. Hypercest detection of cucurbit[6]uril in whole blood using an ultrashort saturation pre-pulse train. *Contrast Media Mol. Imaging* **11**, 285–290.

[145] Assaf, K. & Nau, W. Cucurbiturils: From synthesis to high-affinity binding and catalysis. *Chemical Society Reviews* **44**, 394–418.

[146] Farhadi, A. Recombinantly expressed gas vesicles as nanoscale contrast agents for ultrasound and hyperpolarized mri. *AIChE J* **64**, 2927–2933.

[147] Woessner, D., Zhang, S., Merritt, M. & Sherry, A. Numerical solution of the bloch equations provides insights into the optimum design of paracest agents for mri. *Magn. Reson. Med* **53**, 790–799.

[148] Li, A. Four-pool modeling of proton exchange processes in biological systems in the presence of mri-paramagnetic chemical exchange saturation transfer (paracest) agents. *Magn. Reson. Med* **60**, 1197–1206.

[149] Sun, P. Simplified and scalable numerical solution for describing multi-pool chemical exchange saturation transfer (cest. *MRI contrast. J. Magn. Reson* **205**, 235–241.

[150] Williams, M. & Williams, M. The general solution to the bloch equation with constant rf and relaxation terms: Application to saturation and slice selection. *Med. Phys* **20**, 5–13.

[151] Roell, S., Dreher, W. & Leibfritz, D. A general solution of the standard magnetization transfer model. *J. Magn. Reson* **132**, 96–101.

[152] Madhu, P. & Kumar, A. Direct cartesian-space solutions of generalized bloch equations in the rotating frame. *J. Magn. Reson. Ser. A* **114**, 201–211.

[153] Roberts, J. The bloch equations. how to have fun calculating what happens in nmr experiments with a personal computer. *Concepts Magn. Reson* **3**, 27–45.

[154] Murase, K. & Tanki, N. Numerical solutions to the time-dependent bloch equations revisited.

[155] Klibanov, A., Shevchenko, T., Raju, B., Seip, R. & Chin, C. Ultrasound-triggered release of materials entrapped in microbubble-liposome constructs: A tool for targeted drug delivery. *J. Control. Release* **148**, 13–17.

[156] Kheirolomoom, A. Acoustically-active microbubbles conjugated to liposomes: Characterization of a proposed drug delivery vehicle. *J. Control. Release* **118**, 275–284.

[157] Unger, E. Therapeutic applications of lipid-coated microbubbles. *Adv. Drug Deliv. Rev* **56**, 1291–1314.

[158] Liu, Y., Miyoshi, H. & Nakamura, M. Encapsulated ultrasound microbubbles: Therapeutic application in drug/gene delivery. *J. Control. Release* **114**, 89–99.

[159] Dijkmans, P. Microbubbles and ultrasound: From diagnosis to therapy. *Eur. J. Echocardiogr* **5**, 245–256.

[160] Ferrara, K., Pollard, R. & Borden, M. Ultrasound microbubble contrast agents: Fundamentals and application to gene and drug delivery. *Annu. Rev. Biomed. Eng* **9**, 415–447.

[161] Lum, A. Ultrasound radiation force enables targeted deposition of model drug carriers loaded on microbubbles. *J. Control. Release* **111**, 128–134.

[162] Reusser, T. Phospholipid oxygen microbubbles for image-guided therapy. *Nanotheranostics* **4**, 83–90.

[163] Kheir, J. Oxygen gas-filled microparticles provide intravenous oxygen delivery. *Sci. Transl. Med* **4**, 140–188.

[164] Cheung, J., Chow, A., Guo, H. & Wu, E. Microbubbles as a novel contrast agent for brain mri. *Neuroimage* **46**, 658–664.

[165] Grobner, T. A specific trigger for the development of nephrogenic fibrosing dermopathy and nephrogenic systemic fibrosis? nephrol. *Dial. Transplant* **21**, 1104–1108.

[166] *Journal of the American Chemical Society* **131**.

[167] Sander, R. Compilation of henry's law constants (version 4.0) for water as solvent. *Atmos. Chem. Phys* **15**, 4399–4981.

[168] Chann, B., Nelson, I., Anderson, L., Driehuys, B. & Walker, T. 129xe - xe molecular spin relaxation. *Phys. Rev. Lett* **88, 4**.

[169] Fix, S. Accelerated clearance of ultrasound contrast agents containing polyethylene glycol is associated with the generation of anti-polyethylene glycol antibodies. *Ultrasound Med. Biol* **44**, 1266–1280.

[170] Full prescribing information for definity®. URL `https://www.definityimaging.com/prescribing-information.html`.

[171] Nouls, J., Fanarjian, M., Hedlund, L. & Driehuys, B. A constant-volume ventilator and gas recapture system for hyperpolarized gas mri of mouse and rat lungs. *Concepts Magn. Reson. Part B Magn. Reson. Eng* **39B**, 78–88.

[172] Torres, A. & Price, W. Common problems and artifacts encountered in solution-state nmr experiments. *Concepts Magn. Reson. Part A Bridg. Educ. Res* **45A, e21387(1-16**.

[173] Kwan, J. & Borden, M. Microbubble dissolution in a multigas environment. *Langmuir* **26**, 6542–6548.

[174] Mullin, L. Effect of anesthesia carrier gas on in vivo circulation times of ultrasound microbubble contrast agents in rats. *Contrast Media Mol. Imaging* **6**, 126–131.

[175] Duncan, P. & Needham, D. Test of the epstein-plesset model for gas microparticle dissolution in aqueous media: Effect of surface tension and gas undersaturation in solution. *Langmuir* **20**, 2567–2578.

[176] Durrant, C., Hertzberg, M. & Kuchel, P. Magnetic susceptibility: Further insights into macroscopic and microscopic fields and the sphere of lorentz. *Concepts Magn. Reson* **18A**, 72–95.

[177] Sarkar, K., Katiyar, A. & Jain, P. Growth and dissolution of an encapsulated contrast microbubble: Effects of encapsulation permeability. *Ultrasound Med. Biol* **35**, 1385–1396.

[178] Wischhusen, J. & Padilla, F. Ultrasound molecular imaging with targeted microbubbles for cancer diagnostics: From bench to bedside. *IRBM* **40**, 3–9.

[179] Phs policy on humane care and use of laboratory animals — olaw. URL `https://olaw.nih.gov/policies-laws/phs-policy.htm`.

[180] Animal welfare act — animal welfare information center — nal — usda. URL `https://www.nal.usda.gov/awic/animal-welfare-act`.

[181] Council, N. Guide for the care and use of laboratory animals. In *Guide for the Care and Use of Laboratory Animals (National Academies Press*.

[182] Probing lung physiology with xenon polarization transfer contrast (xtc. *Magn. Reson. Med* **44**, 349–357.

[183] Wang, Y. & Dmochowski, I. An expanded palette of xenon-129 nmr biosensors. *Acc. Chem. Res* **49**, 2179–2187.

[184] Trott, O. & Palmer, A. Theoretical study of r1 rotating-frame and r2 free-precession relaxation in the presence of n-site chemical exchange. *J. Magn. Reson* **170**, 104–112.

[185] Sloniec, J. Biomembrane interactions of functionalized cryptophane-a: Combined fluorescence and 129xe nmr studies of a bimodal contrast agent. *Chem. - A Eur. J* **19**, 3110–3118.

[186] Lu, G. Acoustically modulated magnetic resonance imaging of gas-filled protein nanostructures. *Nat. Mater* **17**, 456–463.

[187] Durham, P. & Dayton, P. Applications of sub-micron low-boiling point phase change contrast agents for ultrasound imaging and therapy. *Curr. Opin. Colloid Interface Sci* **56**, 101498.

[188] Jägers, J., Wrobeln, A. & Ferenz, K. Perfluorocarbon-based oxygen carriers: from physics to physiology. *Pflügers Arch. - Eur. J. Physiol* **4732 473**, 139–150.

[189] Sheeran, P. Contrast-enhanced ultrasound imaging and in vivo circulatory kinetics with low-boiling-point nanoscale phase-change perfluorocarbon agents. *Ultrasound Med. Biol* **41**, 814–831.

[190] CABRALES, P., VÁZQUEZ, B., NEGRETE, A. & INTAGLIETTA, M. Perfluorocarbons as gas transporters for o2, no, co and volatile anesthetics. *Transfus. Altern. Transfus. Med* **9**, 294–303.

[191] Clark, L. & Gollan, F. Survival of mammals breathing organic liquids equilibrated with oxygen at atmospheric pressure. *Science* **80-.). 152**, 1755–1756.

[192] Pollack, G., Kennan, R. & Holm, G. Solubility of inert gases in pfc blood substitute. *Blood Plasma, and Mixtures* 1101–1104.

[193] Choudhury, S., Xie, F., Dayton, P. & Porter, T. Acoustic behavior of a reactivated, commercially available ultrasound contrast agent. *J. Am. Soc. Echocardiogr* **30**, 189–197.

[194] Alecci, M. Radio frequency magnetic field mapping of a 3 tesla birdcage coil: Experimental and theoretical dependence on sample properties. *Magn. Reson. Med* **46**, 379–385.

[195] Venkatesh, A., Zhao, L., Balamore, D., Jolesz, F. & Albert, M. Evaluation of career agents for hyperpolarized xenon mri. *NMR Biomed* .

[196] Tseng, C. Nmr of laser-polarized 129xe in blood foam. *J. Magn. Reson* **126**, 79–86.

[197] Alexander, A., McCreery, T., Barrette, T., Gmitro, A. & Unger, E. Microbubbles as novel pressure-sensitive mr contrast agents. *Magn. Reson. Med* **35**, 801–806.

[198] Dharmakumar, R., Plewes, D. & Wright, G. On the parameters affecting the sensitivity of mr measures of pressure with microbubbles. *Magn. Reson. Med* **47**, 264–273.

[199] Dharmakumar, R., Plewes, D. & Wright, G. A novel microbubble construct for intracardiac or intravascular mr manometry: a theoretical study. *Phys. Med. Biol* **50**, 4745.

[200] Hayes, P. & Walsby, A. The inverse correlation between width and strength of gas vesicles in cyanobacteria. URL `http://dx.doi.org/10.1080/00071618600650221`.